Investigations of GaN-based Micro-pillars by a Multi-scale Scanning Tunneling Microscope

Von der Fakultät für Mathematik und Physik
der Gottfried Wilhelm Leibniz Universität Hannover

zur Erlangung des Grades
Doktor der Naturwissenschaften
Dr. rer. nat.

genehmigte Dissertation
von

Dipl.-Phys. Fatih Kalkan
geboren am 17. Juni 1975 in Istanbul

2012

Referentin: Prof. Dr. Karina Morgenstern
Koreferent: Prof. Dr. Peter Lemmens

Tag der Promotion: 09. Mai 2012

3

Abstract

This Ph.D. thesis focuses on the construction of a room temperature, multi-scale Scanning tunneling microscope in a ultra-high vacuum system and the investigations of Gallium Nitride (GaN)-based micro-pillars by use of the multi-scale STM.

In the first part, the design and construction of the experimental setup is presented. A beetle-type stage and an XYZ-scanning stage are combined to form a two-stage scanning tunneling microscope (STM) that operates at room temperature in an ultra-high vacuum and is capable of scanning areas of up to 450 μm x 450 μm down to resolutions on the nanometer scale. This multi-scale STM has been designed and constructed in order to investigate pre-structured metallic or semiconducting micro- and nano-structures in real space, from atomic-sized structures to the large-scale environment. The principle of the instrument is demonstrated on two different systems. GaN-based micro-pillars demonstrate scan areas of up to hundreds of micrometers while an Au(111) surface demonstrates nanometer resolutions.

In the second part, GaN-based III-V compound semiconductor micro-pillars are investigated by using the multi-scale STM. In addition to morphological investigations, this study also contains, for the first time, investigations on the electronic structure of those micro-pillars on the hundreds of micrometer scale. According to morphology investigations, the GaN-based sample contains various types of micro-pillars, and each kind of micro-pillar has individual etching characteristics and individual distributions of spacing. Furthermore, the formation of various types of micro-pillars is pointing to different etching rates, and the investigations have revealed that the a-planes with lower atom density are etched faster.

The local scanning tunneling spectroscopy (STS) is used to find out the doping type, the oxidation and metallization levels, the terminating layer, and the band gap energy width of the individual micro-pillars. According to the STS measurements, the band gap energy of the micro-pillars' surface consists not only of GaN as expected, but rather contains metallic (Ga-rich), semiconducting (GaN, InGaN), impurity, and oxide regions. Sputtering of the surface to remove the residual oxide resulted in the polarization of the surface; the N atoms, because of their higher sputtering yields, were removed while the Ga was left behind, leaving the surface metallic.

Keywords: STM, GaN-based micro-pillars, spectroscopy

Kurzfassung

Die vorliegende Dissertation beschäftigt sich mit der Konstruktion, dem Aufbau und der Inbetriebnahme eines multiskaligen Raumtemperatur-Rastertunnelmikroskops (RTM) als Teil eines Ultrahochvakuum (UHV)-Systems. Die Möglichkeiten der Anlage werden anhand detaillierter Untersuchungen an Galliumnitrid-(GaN)-basierten Mikrosäulen vorgestellt.

Im ersten Teil wird der Aufbau des RTM-Systems beschrieben. Das zweistufige RTM besteht aus der Kombination eines RTM-Scanners vom Typ "beetle" mit einer XYZ-Scanplattform. Es arbeitet bei Raumtemperatur unter Ultrahochvakuum-Bedingungen und erlaubt es, Flächen von bis zu 450 μm x 450 μm mit einer Auflösung von besser als 1 nm zu untersuchen. Das System ist damit geeignet, die Morphologie und die elektrischen Eigenschaften von metallischen und halbleitenden Mikro- und Nanostrukturen sowohl auf makroskopischer, mikroskopischer, nanoskopischer als auch auf sub-nanoskopischer (atomarer) Skala zu studieren. Die Möglichkeiten der Anlage werden an zwei unterschiedlichen Systemen demonstriert. Die Untersuchung an GaN-basierten Mikrosäulen zeigt die Möglichkeit Hunderte von Mikrometern grosser Scanflächen, während Messungen einer Au(111)-Oberfläche die Möglichkeit von Auflösungen besser als 1nm aufzeigt.

Im zweiten Teil werden Untersuchungen mit diesem RTM-System an GaN-basierten III-V-Verbindungshalbleiter- Mikrosäulen vorgestellt. Zusätzlich zur Morphologie werden hier zum ersten Mal auch Untersuchungen zur elektronischen Struktur dieser Mikrosäulen gezeigt. Die GaN-basierte Probe enthält verschiedene Typen von Mikrosäulen mit einer individuellen Ätz-Charakteristik und Verteilung der Abstände. Insbesondere verdeutlicht die Bildung verschiedener Typen von Mikrosäulen unterschiedliche Ätzraten. Die Untersuchungen zeigen, dass die Ebenen mit niedrigerer Atom-Dichte (a-Ebenen) schneller geätzt werden. Rastertunnelspektroskopie (RTS) wird genutzt, um die Dotierung, den Oxidations- und Metallisierungsgrad, die Art der abschliessenden Schicht und die Breite und Lage der Bandlücken der Mikrosäulen zu untersuchen. Demnach sind die Oberflächen der Mikrosäulen nicht homogen wie erwartet, sondern bestehen aus inhomogen verteilten Bereichen mit metallischem (Ga-reich) und halbleitendem (GaN, InGaN) Charakter bzw. Verunreinigungen und oxidierten Bereichen. Das Sputtern der Säulen-Oberflächen zur Entfernung von Oxidschichten führt zur Polarisation der Oberfläche. Aufgrund ihrer grösseren Sputter-Ausbeute werden die N-Atome aus Oberflächen-nahen Bereichen ent-

fernt. Die damit einhergehende Anreicherung von Ga-Atomen führt zur Metallisierung der Oberflächen.

Schlagworte: RTM, GaN-basierte Mikrosäulen, Spektroskopie

Contents

Chapter 1

Introduction

The scanning tunneling microscope (STM) [1, 2, 3, 4, 5], following its invention in 1981, has opened up novel realms for surface and adsorbate studies. Characteristic features of the tunneling current provide not only real space imaging on the atomic-scale, but also local information of electronic structures. Furthermore, the adsorption and diffusion of atoms and molecules on surfaces [6], semiconductors [7], surface chemistry [8], and molecular switches [9] were investigated. The construction of STMs started in the early 1980s [10]. A primal aspect of STM construction consists of bringing the tip from macroscopic distances close enough to the sample (coarse approach) such that a tunneling current flows. From the early days piezoelectric material was used for this purpose. As a first design a tripod scanner was used for this coarse approach. However, the difficulties in thermal drift prompted the development of the beetle-type STM [11, 12]. In this new design, the sample or the tip is moved also in a horizontal direction on the millimeter scale with a slip-stick method of three tube piezos. The larger temperature stability is achieved by the highly symmetric design. This design allows to approach any point on the investigated sample. One drawback of this flexibility, however, is a reduced mechanical stability [13] due to a ramp that is connected to the piezo tubes only by gravity. In a different approach, the Aarhus design [14] uses an inchworm motor for the coarse approach. On the other hand, with its compact design, the Aarhus STM achieved a high stability, resulting in the very fast scanning rate of up to one image per 1s. The drawback here is that no horizontal motion on the millimeter scale is possible.

Nowadays, most STMs utilize a piezo tube with five electrodes that are used for x, y and z motion. While these piezos allow atomically resolved images, the mechanical instability of larger piezos of this type restricted the ability of STM to scan, allowing only up to $\approx 10\ \mu$m.

However, for prestructured samples it is desirable to image their topography on the millimeter and the micrometer scale and then magnify a chosen region to make further topographic and electronic investigations on the nanometer scale. This can be achieved by a combination of a scanning electron microscope (SEM) and a STM [15]. Typically, thereby the scan regions of the SEM are from 1 mm x 1 mm down to 10 nm x 10 nm after having chosen a specific region of the prestructured sample by an optical microscope. However, in the combined instrument, the SEM does only yield structural information in two dimensions and no information of e.g. roughness can be achieved. In addition, it is not possible to obtain information about the electronic features of the surfaces or adsorbates by SEM. Furthermore, the mechanical instability restricts the spatial resolution of the instrument to 10-20 nm. Finally, electron sensitive adsorbates and the surfaces might be altered by the high energy electron beam used. Apart from these technical restrictions, the high costs for such an instrument make it desirable to develop a different solution for the investigation of prestructured surfaces in real-space.

In the first part of this Ph.D. thesis, I present the design and construction of a multi-scale STM coupling two different scan units. A XYZ-scanning stage may scan regions up to 450 μm x 450 μm with a height variation up to 50 μm. A beetle-type STM is used for submicrometer and high resolution images. This allows us to image regions as chosen by an optical microscope and obtain topographic and electronic information in the entire region. The multi-scale STM with its ability of scanning from millimeter scale images down to nanometer scale resolution facilitates to overcome the limitations imposed by SEM.

Such a multi-scale STM requires a combination of several cooperating electronic units to control the system. In addition to the electronic units, a double interface software, each controlling a scan unit, is utilized for the operation of the multi-scale STM. Two feedback loops control each scan unit. Furthermore, it is designed rigidly with compact components to avoid shaking and a combination of damping systems is used to filter the vibrational noise from 1 to 1500 Hz in different directions. These technical issues in the construction of the multi-scale STM were the most challenging to surmount, as they restrict the spatial resolution of the instrument.

I use a microstructured GaN-based sample to demonstrate the capability of the multi-scale STM. In the field of nano-technologies the III-V compound semiconductor heterostructures are of increasing interest because of their broad optical emission bands in all regions of the visible spectrum [16]. These heterostructures are used in all-semiconductor optoelectronic devices, such as blue light emitting diodes (LED) [17, 18, 19, 20, 21, 22] and laser diodes (LD) [23, 24].

Since recently, the brightness and the durability of LEDs are sufficient for using them in displays and light sources.

LDs are used in optical communication and storage systems. The storage capacity of optical disks is improved by the invention of materials with shorter wavelengths. The optical disks began their evolution with compact disks (CDs), relying on infrared aluminium gallium arsenide (AlGaAs) laser diodes, and later improved to DVDs by utilizing red laser diodes based on aluminium indium gallium phosphate (AlInGaP). Today, gallium nitride (GaN) blue-light laser diodes are used to make Blu-ray disks.

Beyond these planar heterostructures, the controlled growth and etching of GaN-based micro-pillars is expected to increase the efficiency of optoelectronic devices further and gain increasing attention in the fabrication of a new generation of LEDs and LDs [25]. With the advantages of micro-pillars over thin film devices, new possibilities emerge in growing defect-reduced structures for light emitting as well as the enlargement of the effective area. However, the fabrication of those micro-pillars is not yet well understood. Thus, further control and verification information is required to improve their fabrication. These structures provide thus an ideal system to demonstrate the capabilities of the multi-scale STM. In the second part of this Ph.D. thesis, I present a combined study on 3D GaN-based micro-pillars. The morphology investigations show that different kinds of micro-pillars have different spatial distributions because of their etching character. The low etching rates form pillars with inhomogeneous spatial distribution. On the other hand, the high etching rates form pillars with homogeneous spatial distribution but cause a drawback of further etching of the pillars to their centers instead of stopping at the border defined by the mask. Furthermore, the electronic structure has been observed for the first time locally by means of multi-scale STM. This study reveals that the band gap width of the individual micro-pillars is inhomogeneously distributed.

This Ph.D. thesis is structured as follows. In chapter 2, the theories and working principles of STM, SEM, and XRD are explained. Also in this chapter, the scanning tunneling spectroscopy (STS) is described, as this technique is used to measure the band gap energy widths of the micro-pillars.

In chapter 3, I present the design and construction of a rigid room temperature multi-scale STM (see section 3.3) in a ultra-high vacuum (UHV) chamber (see section 3.1) and various sample handling (see section 3.2) instruments necessary for the sample transfer and the preparation. The multi-scale STM is established from two different scan units (see section 3.3). The technical properties, operating principles of the beetle-type STM (see section 3.3.2) and the XYZ-scanning stage-based STM (see section 3.3.3), and the damping system (see section 3.3.5) are described in detail.

The control electronics and the software of the multi-scale STM (see section 3.4) are also presented in chapter 3. The two scan units are controlled by various electronics and a software with two interfaces controlling each scan unit. Two feedback loops are used to regulate these two scan units.

In chapter 4, the operating principle of the multi-scale STM is demonstrated on two different systems. Gallium nitride (GaN) based micro-pillars are studied to prove large scan ranges from 450 μm x 450 μm images down to 7 μm x 7 μm images. The current resolution limit is demonstrated at the reconstruction lines of an Au(111) surface.

Chapter 5 contains a combined study of the geometrical and electronic structure study on GaN-based micro-pillars. According to the geometrical investigations, the GaN-based sample contains various types of micro-pillars. Micro-pillars vary from one another not only because of their different shapes but also due to their different spacing distributions caused by various etching characteristics. The local scanning tunneling spectroscopy (STS) was used to observe the electronic structure of the micro-pillars' surface. The STS allows for the determination of the doping type, the oxidation and metallization levels, the terminating layer, and the band-gap energy width of the individual micro-pillars is determined. According to its findings, the surfaces of the micro-pillars are not conserved homogeneously–consisting only of GaN, as expected–but rather are inhomogeneously distributed, containing metallic (Ga-rich), semiconducting (GaN, InGaN), impurity, and oxide regions. Some possible reasons for this will be explained later in this work.

Chapter 2

Methods

In this chapter, the methods used in this thesis are presented. In section 2.1, the STM's operating principle and theory are explained, while section 2.1.3 describes the theory of scanning tunneling spectroscopy (STS). In section 2.2, the SEM's operating principle is explained, and finally, section 2.3 describes the operating principle of X-ray diffraction (XRD).

2.1 Scanning Tunneling Microscopy

The STM, following its invention in 1981 by G. Binning and H. Rohrer [5, 10, 2], has opened a new realm in the field of surface science investigations. It allows the study of metallic and semiconducting surfaces on the atomic scale. In this section, the physical and theoretical operating principles of the STM as well as the scanning tunneling spectroscopy (STS)–which is used to investigate the electronic structures of the surfaces–will be briefly explained.

2.1.1 Principle of STM

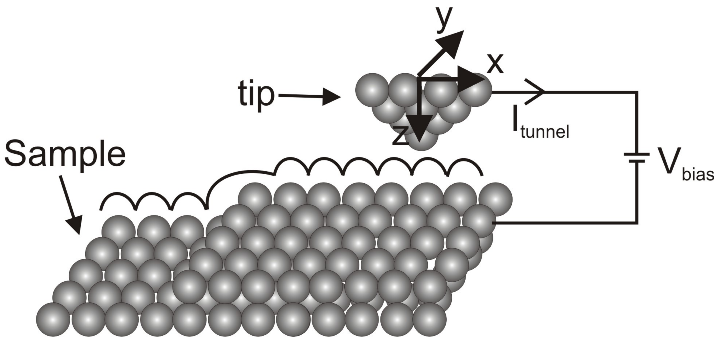

Figure 2.1: Scheme of the constant current mode operation of the STM. A feedback loop regulates the distance between the tip and the sample so that the tunneling current, I_{tunnel}, is kept constant at an applied bias voltage. The tip scans the surface in the x- and y- directions, creating a topographical image.

The STM uses the quantum mechanical tunneling of electrons between two electrodes as its working principle. A very sharply-formed metallic tip (ideally with only one atom on the head of the tip) is positioned only few Angstroms (Å) from a conductive surface (metal or semi-conductor) that is to be investigated. Meanwhile, a voltage of only a few volts is applied between the tip and the sample. Classically, the energy of the electrons is not large enough to overcome the potential barrier between the tip and the sample, thus forbidding a current flow between them. Quantum mechanically, the wave functions of the tip and the sample decay into the gap and overlap each other. This gives the electrons a finite probability of tunneling. The tunneling current is in magnitudes of pico- to nano-Amperes. The direction of the tunneling of the electrons is related to the polarity of the voltage chosen between the electrodes. The tunneling current I_T shows an exponential behaviour related to the distance d between the electrodes.

$$I_T(z) \propto exp(-2\kappa d) \tag{2.1}$$

with a wave vector

$$\kappa = \frac{\sqrt{2m\,|E|}}{\hbar} \tag{2.2}$$

This exponential dependence allows the STM to achieve a resolution of 1 pm in the vertical direction. Aided by the piezo electric ceramics, the tip scans the surface line-by-line, as shown in Fig. 2.1. In the constant-current mode–the working mode used in this work–the tunneling current is kept constant and the height (z) of the tip is regulated by a feedback loop. A topographical image of the surface is obtained through the tip height (z) at each lateral point P(x,y) scanned on the surface. However, due to electronic effects the STM creates not only a topographical map but also a map of constant local density of states (LDOS). The overlapping of the geometrical and electronic effects leads to talk about a relative height at STM.

2.1.2 Theory of STM

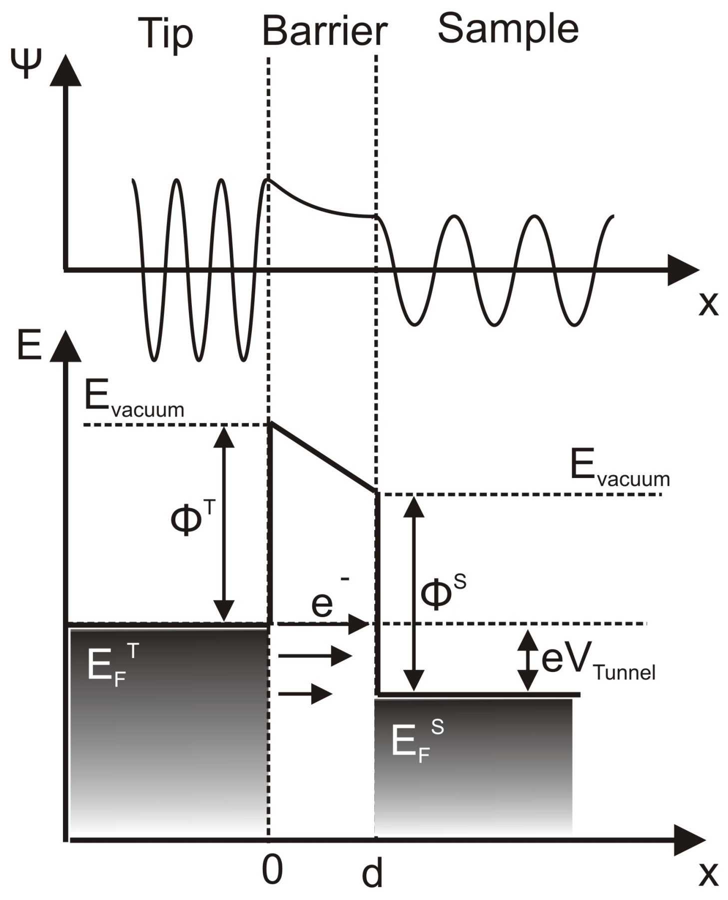

Figure 2.2: Tunneling through a one-dimensional triangular potential barrier and corresponding wave functions. The electrons tunnel from the tip to the sample. E_F^T and E_F^s are Fermi energies, Φ^T and Φ^S are the work functions of the tip and the sample, respectively. The vacuum levels are shown by E_{vacuum}, while E_{tunnel} is determined by the bias voltage.

The theory of the tunneling process has been studied in great extent. In this section, the fundamental theories will be briefly reviewed. In a simplified picture, the tunneling effect can be described one-dimensionally and time-independently. The stationary Schrödinger equation defines the inelastic tunneling of an electron through a potential barrier, as shown in eq. 2.3:

$$\left[\frac{1}{2m}\left(\frac{\hbar}{i}\frac{\partial}{\partial x}\right)^2 + V(x)\right]\psi(x) = E\psi(x). \tag{2.3}$$

E is the energy, ψ is the wave function of the tunneling electron and V(x) is the potential barrier. The electron is assumed to be a free particle inside the metal but the electron's energy in the tunneling region is smaller than the potential. The Schrödinger equation for the wave functions in the metal and in the barrier can be solved. Based on the wave functions ψ(x), the probability P of finding the particle can be calculated.

A wave is reflected and transmitted by a barrier. The transmission coefficient T can be calculated by differentiating the wave functions and using the boundary conditions for the potential barrier.

$$T = \frac{1}{1 + \frac{\left(k^2+\kappa^2\right) sinh^2(\kappa d)}{4k^2\kappa^2}} \tag{2.4}$$

with

$$\kappa = \frac{\sqrt{2m\left(V_0 - E\right)}}{\hbar} \tag{2.5}$$

E is the energy and m is the mass of the electron. V_0 is the height and d is the width of the barrier. k and κ are the wave vectors outside and inside the barrier, respectively. The exponential dependence of the transmission coefficient T is derived by an approximation for a large barrier of κ d $\gg$ 1 [26] as

$$T \approx \frac{16k^2\kappa^2}{k^2+\kappa^2} \cdot \exp\left(-2\kappa d\right). \tag{2.6}$$

The exponential relationship between the tunneling distance d and the transmission coefficient explains the exponential dependence of the tunneling current to the tip-sample distance in the STM. Due to this exponential dependence, the STM is able to achieve high spatial resolutions.
In 1961, Bardeen has treated the problem more detailed in three-dimensions in

time-dependent perturbation theory [27]. He used the assumption that the two electrodes do not strongly interact and are separated by a barrier so that the tunneling probability is small. The transmission probability of the two unperturbed states ψ_μ and ψ_ν at the two opposite sides of the potential barrier is defined as the Bardeen integral $M_{\mu\nu}$:

$$M_{\mu\nu} = -\frac{\hbar^2}{2m}\int_A d\vec{A}\left(\psi_\mu^* \vec{\nabla}\psi_\nu - \psi_\nu \vec{\nabla}\psi_\mu^*\right) \tag{2.7}$$

The ψ_μ and the ψ_ν are the wave functions of the tip and the sample, respectively. The tip state ψ_μ and the sample state ψ_ν overlap each other in an area A at the tunneling barrier. Following Bardeen's theory, Tersoff and Hamann calculated the tunneling current I_T for the STM [28][29] by utilizing the matrix element $M_{\mu\nu}$. They started by assuming a spherical tip with a curvature of R and a plane substrate as shown in Fig. 2.3. Assuming that the bias voltage is smaller than the work function of the tip and that the sample is at zero Kelvin, this reduced the I_T to :

$$I_T = \frac{2\pi e^2}{\hbar} V \sum_{\mu\nu} \left|M_{\mu\nu}\right|^2 \delta\left(E_\mu - E_F\right)\delta\left(E_\nu - E_F\right). \tag{2.8}$$

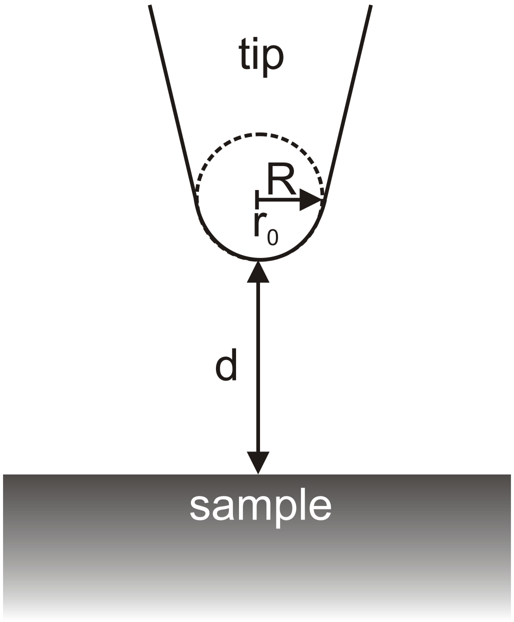

Figure 2.3: Schematic drawing of tunneling geometry in Tersoff-Hamann Theory. The tip is assumed to be spherical with a curvature radius of R and centered at r_0. The nearest distance between the tip and the sample is d.

Where E_F is the Fermi energy and E_μ and E_ν are the corresponding energies of the wave functions ψ_μ and ψ_ν in eq. 2.7. However, in order to calculate the tunneling matrix element $M_{\mu\nu}$, Tersoff and Hamann assumed that the wave function ψ_ν of the electron in the sample propagates freely parallel to the surface and decays exponentially perpendicular to it. The work functions, which affect the decay rate are also assumed to be equal for the tip and for the sample. With these assumptions, the Bardeen integral 2.7 can be calculated as:

$$M_{\mu\nu} = \frac{2\pi\hbar^2}{m\sqrt{\Omega_t}} R \exp^{\kappa R} \psi_\nu (r_0) \tag{2.9}$$

where Ω_t is the volume of the tip. With this new tunneling matrix element the I_T in eq. 2.8 is given by:

$$I_T = \frac{32\pi^3 e^2 \Phi^2 R^2 \exp^{2kR}}{\hbar\kappa^4} V \cdot D_t (E_F) \cdot \underbrace{\sum_\nu \left|\psi_\nu (\vec{r_0})\right|^2 \delta (E_\nu - E_F)}_{\equiv D_s(\vec{r_0}, E_F)} \tag{2.10}$$

The density of states of the tip per unit volume at the Fermi energy is defined by D_t. The sum in eq. 2.10 is described as the local density of states (LDOS) of the sample at the Fermi energy E_F at the point $\vec{r_0}$. The current measured by the STM reflects as the LDOS of the sample at E_F in the center of the curvature of the tip.

2.1.3 Scanning Tunneling Spectroscopy

The STM is not only capable of giving information about the topography of surfaces but also of giving local information about their electronic structure [30]. The Local Density of States (LDOS) at any given energy are investigated by Scanning Tunneling Spectroscopy (STS).
The STS can be discussed in abstract terms by integrating the terms of the tunneling current as shown in eq. 2.11 up to the applied voltage V

$$I(\vec{r_0}, V) \propto \int_{E_F}^{E_F+eV} D_t\left(E - eV\right) T\left(\vec{r_0}, E, eV\right) D_s\left(\vec{r_0}, E\right) dE \tag{2.11}$$

The D_t and D_s are the density of states of the tip and of the sample, respectively. T is the transmission probability of the tunneling current. The dI/dV in a one-dimensional model is then [31, 32]

$$\begin{aligned}\frac{dI}{dV} &\propto D_t\left(E_F\right) D_s\left(E_F + eV_0\right) T\left(\vec{r_0}, E + eV_0, eV_0\right) \\ &+ \int_{E_F}^{E_F+eV} dE' D_s\left(E'\right) \left.\frac{dD_t}{dE}\right|_{E=E'-eV_0} T\left(\vec{r_0}, E', eV\right) \\ &\quad + \int_{E_F}^{E_F+eV} dE' D_s\left(E'\right) D_t\left(E' - eV\right) \left.\frac{dT}{dV}\right|_{V=V_0} .\end{aligned} \tag{2.12}$$

Assuming that the density of states of the tip is constant, the 2.12 simplifies to :

$$\frac{dI}{dV} \propto D_t\left(E_F\right) \left[D_s\left(E_F + eV_0\right) T\left(\vec{r_0}, E + eV_0, eV_0\right) + \int_{E_F}^{E_F+eV} dE' D_s\left(E'\right) \left.\frac{dT}{dV}\right|_{V=V_0} \right] \tag{2.13}$$

The first term results from the dependence of the interval of the tunneling probability on the variations in the bias voltage. In the integral term the two functions are assumed to be pinned to their respective Fermi energies. Ramping the voltage results in shifting the Fermi energies of the tip and the sample relative to one another. The dI/dV is proportional to the density of states of the sample at an energy $E = eV$ at a given potential.

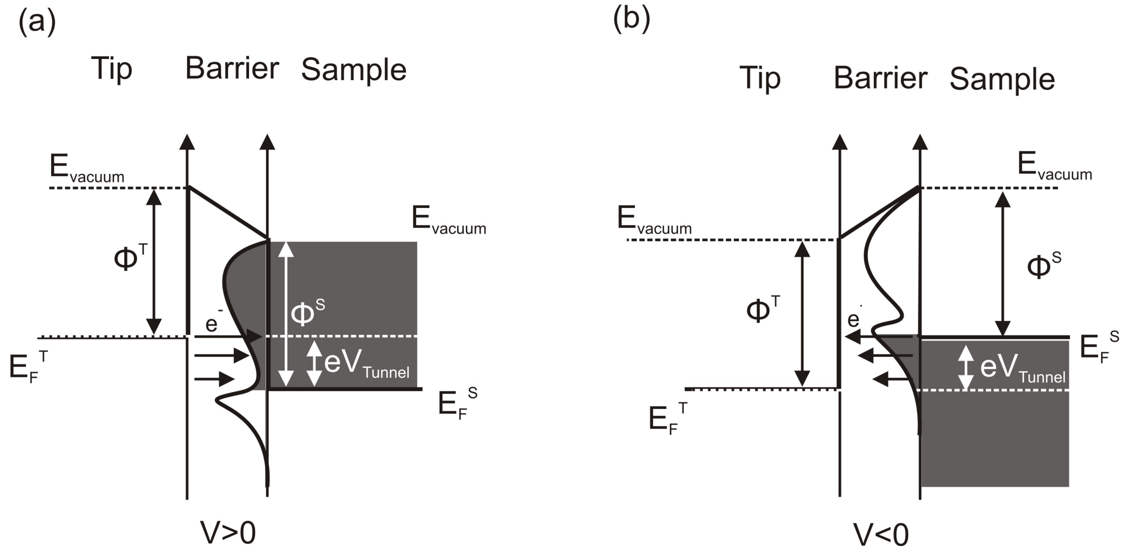

Figure 2.4: Schematic picture of STS. By STS, the changes of the tunneling current, which are due to the LDOS of the sample D_s can be measured. The LDOS of the tip is assumed to be constant. By the variations in the bias voltage, different regions of the LDOS are measured. Φ_t and Φ_s are the work functions of the tip and the sample, respectively. (a) Unoccupied states of the sample are measured at positive sample voltages (b) Occupied states of the sample are measured at negative sample voltages.

By using the STS, it is possible to acquire information about the band gap of semiconductors, the surface states, and more.
Within this work, it was only possible to record I(V)-curves by placing the tip on a chosen point on the surface and ramping the voltage with the feedback loop switched off. That way, the chosen point's spectral density of states can be recorded. The band gaps are measured by numerically taking the first derivative of the I(V)-curves. Recording some hundreds of I(V)-curves allows for the creation of a spatially-resolved band-gap map after a proper drift correction and a band-gap histogram for subsequent evaluations of material distributions on the investigated surface

2.2 Scanning Electron Microscopy

The desire to investigate nano-structures beyond the physical limitation of light microscopes prompted the development of the scanning electron microscopes (SEM) [33]. The SEM utilizes a beam of highly energetic electrons to investigate topographical properties of surfaces on the nanometer scale. The examined surfaces are not necessarily conductive, they can also be insulating. The resolution is limited by the diameter of the electron beam focus: the smaller the diameter of the focus, the higher the resolution. Typically, the diameter of the focus is around 2 nm.

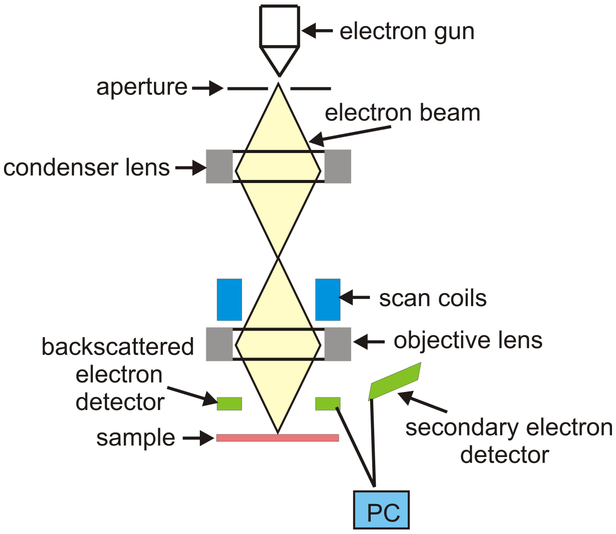

Figure 2.5: Schematic picture of SEM.

As shown in Fig. 2.5, in the SEM a stream of monochromatic electrons generated by a field emission gun (FEG) is directed towards a sample. The electron beam is accelerated by a field of 20 to 30 kV. Various magnetic lenses are used to focus and scan the electron beam onto the sample.

Following the interaction of the primary electron beam with the surface, the electrons lose energy due to random scattering and absorption processes. This interaction volume extends in teardrop-shape into the specimen. The size of the interaction volume depends on the electron's energy, the atomic number and the density of the specimen. The interaction between the high-energy electron beam and the atoms of the sample produces reflection of high-energy electrons as a result of elastic scattering, emission of secondary electrons as a result of inelastic scattering, and also electromagnetic radiation emission. Each of these signals

can be detected by specialized detectors. Normally, the secondary electrons, the backscattered electrons and the x-rays are detected and used to produce the SEM's images.
To avoid interactions of electrons with air molecules, measurements are done in a high vacuum ($\leq 10^{-5}$ mbar).

2.3 X-ray Diffraction

X-ray diffraction (XRD) is an analytical technique that reveals the crystal structure of materials and determines the orientation of a crystal. It is based on the elastic scattering of X-rays from the crystal in many specific directions. From the angles and intensities of the diffracted beams, it is possible to determine the positions of the atoms.
In X-ray diffraction, X-rays interact with the electrons of the solid states atoms. In 1913, an English physicist, Bragg, explained that the X-ray beams are reflected at certain angles of incidence at the cleavage faces of crystals. The Bragg equation is:

$$n\lambda = 2dsin\theta \tag{2.14}$$

where d is the atomic layer displacement of the crystal, λ is the wavelength of the incident X-ray, θ is the diffraction angle, and n is an integer.
In an XRD measurement, a goniometer is used to rotate the crystal as it's bombarded by X-rays. This forms a regularly-spaced diffraction pattern.

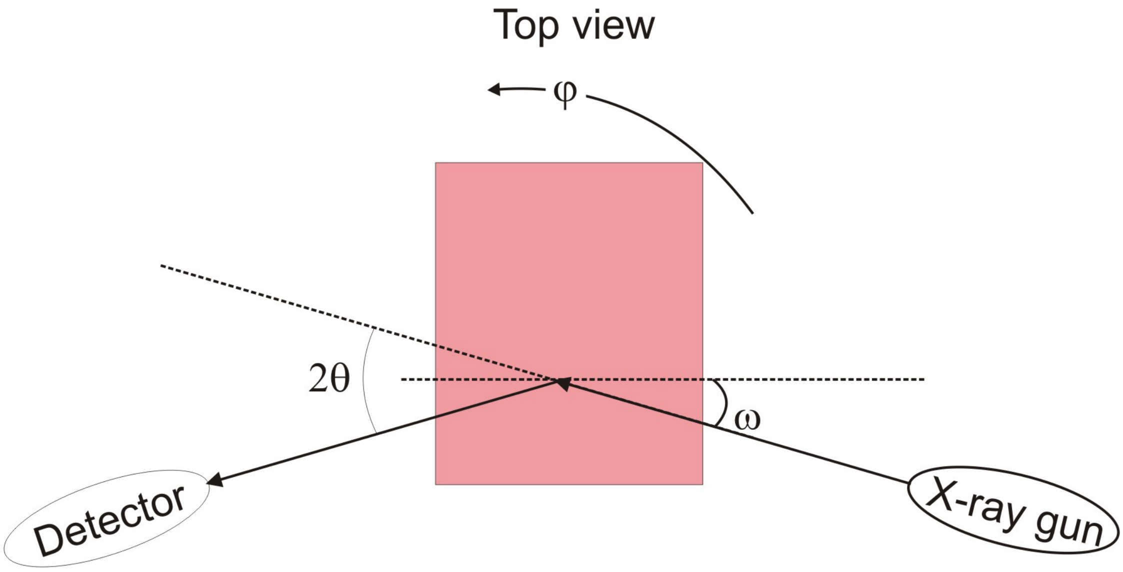

Figure 2.6: Top and side view of the XRD setup, $\chi = 1^o$.

Fig. 2.6 schematically shows the setup of a X-ray diffraction experiment. A sample is placed on a table between the X-ray gun and the detector. The table rotates 360^o in the azimuthal φ-angle. The incidence angle χ is 1^o. θ is the diffraction angle. The X-ray intensity is recorded in a diffraction pattern as a function of 2θ-angle. The anode of the X-ray source can be chosen from different materials, e.g. Cu, W etc.

Chapter 3

Construction of a Multi-scale Scanning Tunneling Microscope

In this chapter, the design and construction of the experimental setup will be explained in detail.

As clean surfaces are a prerequisite to surface science investigations, the UHV system is an unavoidable element in the experimental setup. The UHV system (see section 3.1) is composed of various chambers, each with its own task.

It is also necessary to the experimental setup that the precious single crystal samples are handled by different tools for their transfer, preparation, and storage. These sample handling tools are presented in section 3.2.

The need to investigate atomically-sized structures with respect to their large-scale environment on surfaces pre-structured on the micro or nanometer scales has been fulfilled by the multi-scale STM (see section 3.3). The multi-scale STM, with its two scan units, enables scan areas from 450 μm x 450 μm down to subnanometer resolutions. In addition to metallic and semiconducting planar crystals, predefined 3D micro- and nano-structures can be studied by the large scanning capacity of the multi-scale STM. Furthermore, mechanical stability is achieved by a combination of four damping systems (see section 3.3.5). The damping systems filter the oscillations in different ranges and in different directions.

As the multi-scale STM consists of two scan units, these units are operated by various network attached controllers (see section 3.4). The control software is composed of two user interfaces for each scan unit. Two feedback loops simultaneously regulate the two scan units of the multi-scale STM.

3.1 The Ultra High Vacuum Chamber

Surface studies are generally performed under UHV conditions, providing a clean environment. The UHV system consists of four chambers, each with a different task: the preparation chamber, the STM chamber, the load lock, and the molecule deposition chamber. The chamber is designed so that it can be operated by a single person.

The four different units of the stainless steel UHV chamber are shown in Fig. 3.1. The preparation chamber is used for preparation processes like sputtering and annealing, while the STM chamber houses the multi-scale STM. The load-lock provides a transfer of samples and tips from ambient atmosphere into vacuum without breaking the vacuum of the whole system. Finally, the molecule deposition chamber serves to clean molecules prior to their deposition onto the surfaces. The load-lock and the molecule deposition chamber can be separated from the preparation chamber by gate valves. The samples are transferred between the load-lock and the preparation chamber by a transfer rod, and between the preparation chamber and the STM chamber by a coolable manipulator.

The main UHV chamber is pumped via an ion pump–Vaclon Plus 300 (from *Varian*)–attached to the bottom of the STM chamber (see Fig. 3.1). Its base pressure is $3 \cdot 10^{-10}$ mbar. The vacuum chamber rests on a stainless steel frame. This frame is stabilized by filling it with sand to avoid the transfer of low-frequency oscillations originating from the ground and from the building.

In this section, the functionality and the components of each unit of the UHV chamber is explained in detail.

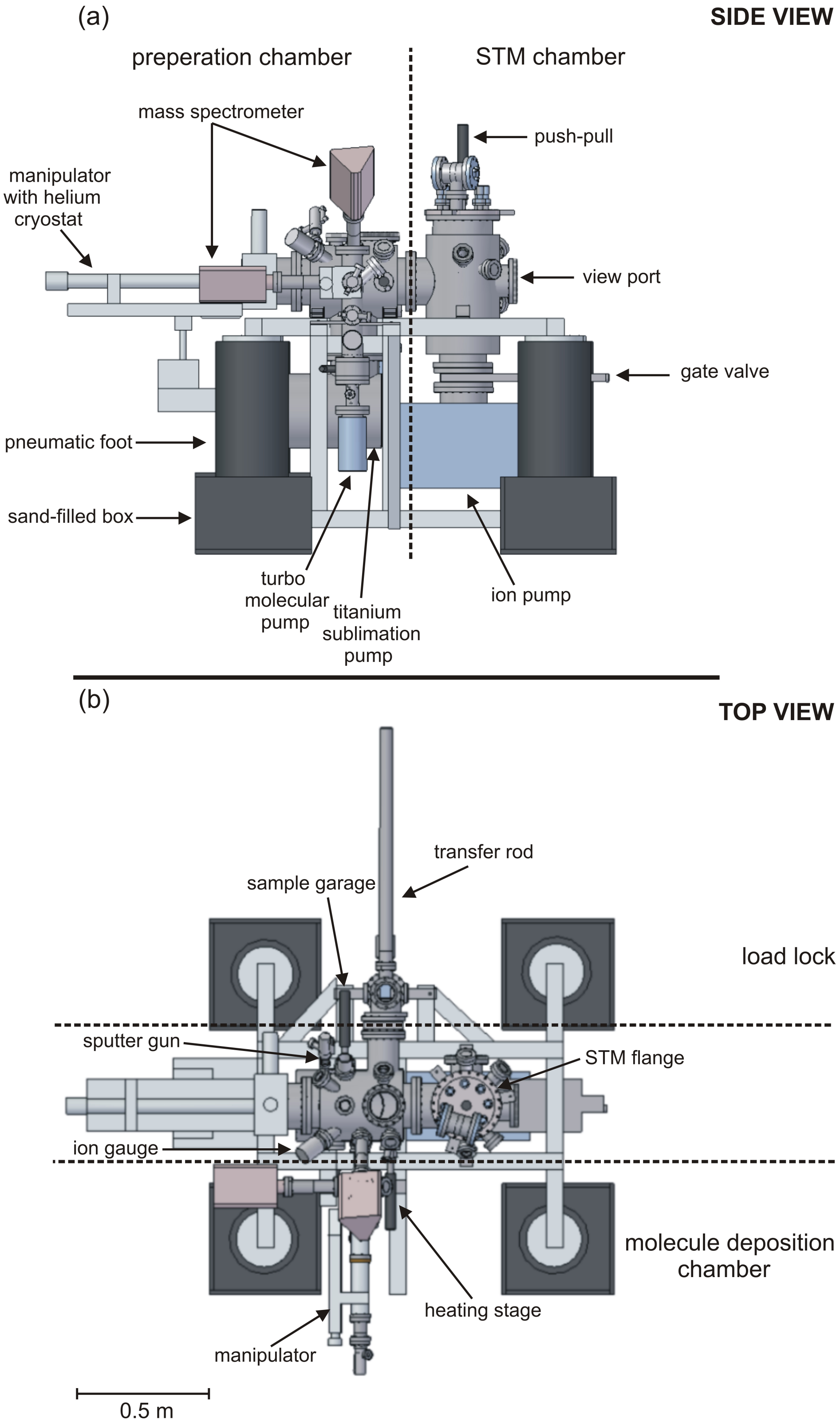

Figure 3.1: Sketch of (a) side and (b) top view of UHV chamber.

3.1.1 Preparation Chamber

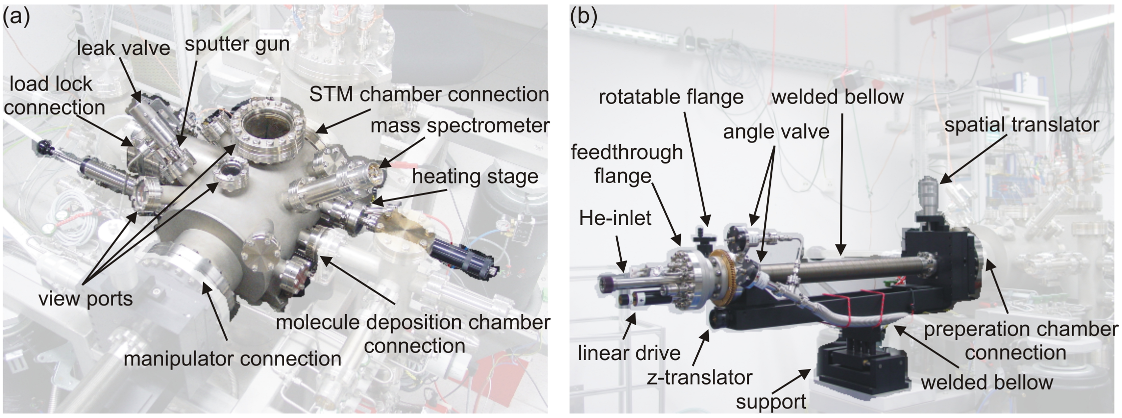

Figure 3.2: Image of (a) preparation chamber and (b) coolable manipulator.

As shown in Fig. 3.2a, the preparation chamber is located at the center of the entire UHV system. The sample is mounted on a commercial xyz-manipulator (from *Vab*), which facilitates the transfer of the samples in front of or into several units of the chamber. The manipulator, which is attached to the preparation chamber, has a differential pump section that makes 360^o rotations possible, as illustrated in Fig. 3.2b. A cryostat is used for cooling the manipulator with liquid nitrogen or helium. The manipulator flange contains a 10-pin feedthrough for electrical connections to the sample, a high voltage feedthrough for high voltage applications to the sample, and a push-pull for grabbing and releasing the sample. Differently-sized view ports provide a good visual access during the transfer of the sample between the units.

The ion sputter gun IQE35 (from *SPECS*) and a custom built heating stage (see section 3.2.2) are utilized for the cleaning process of the samples in this chamber. A mass spectrometer QMA 200 (from *Pfeiffer*) provides rest gas and sputter gas analyses. An ion gauge (from *Varian*) determines the pressure in the vacuum system.

A Titanium Sublimation Pump (TSP) chamber is attached to the bottom of the preparation chamber (see Fig. 3.1). It is operated at 40 A. A cold shield around the TSP is cooled by liquid nitrogen.

Up to four samples and one spare tip can be stored in a custom-built sample garage for easy exchange between different systems without having to transfer them out of the UHV chamber.

3.1.2 STM Chamber

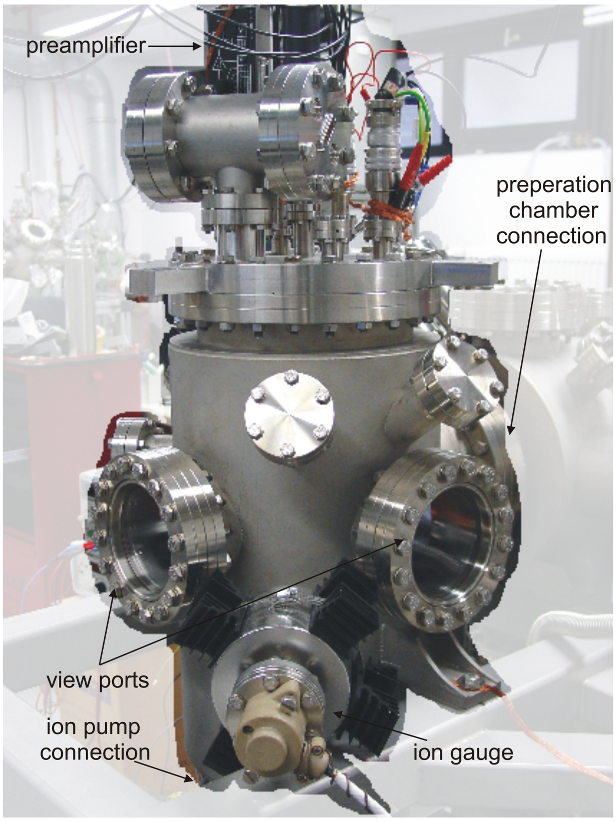

Figure 3.3: Image of the STM chamber and the STM flange.

The STM chamber (Fig. 3.3) houses the multi-scale STM on a CF 200 flange. It is directly connected by a CF 150 flange to the preparation chamber for direct transfer of samples. Good visual access during the transfer of the sample and during the tip into and out of the multi-scale STM is achieved via two CF 150 view ports and one 35 CF viewport at an angle of 45^o degrees from the back side (not visible in (Fig. 3.3)).

3.1.3 Load Lock

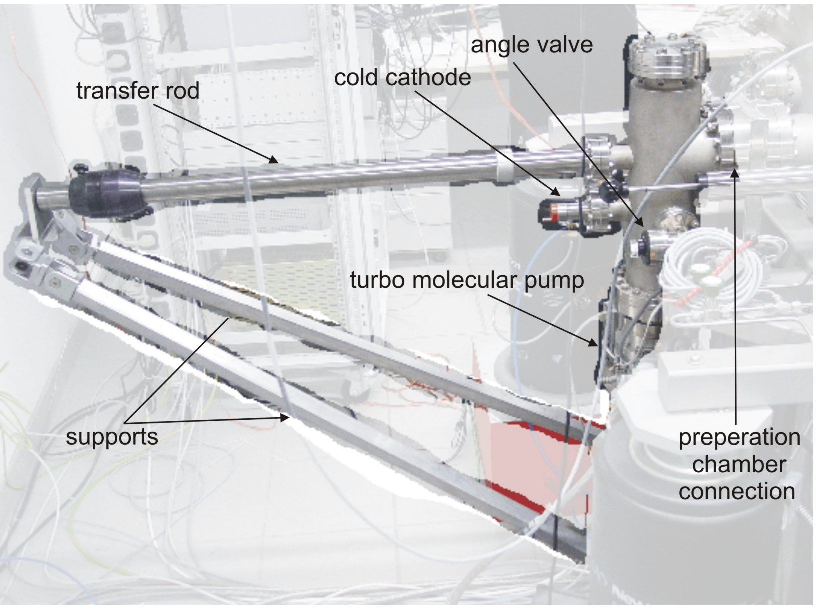

Figure 3.4: Image of the load-lock and the transfer rod.

The load-lock (see Fig. 3.1) allows us to transfer the sample and the tip from ambient conditions into the UHV chamber and back without breaking the vacuum of the whole system. A transfer rod (from *VG Scienta*) is used for these transfers. The load lock is separated from the preparation chamber by a gate-through valve (from *VAT*) for separate venting.

The pumping unit is composed of a membrane pump and a combination of a small and a large turbo pump with pumping capacities of 10 l/s and 70 l/s, respectively. The final pressure of the load-lock is around $9 \cdot 10^{-9}$ mbar before baking and is below $5 \cdot 10^{-9}$ mbar after baking. A cold cathode pressure gauge (from *Pfeiffer*) determines the pressure.

3.1.4 Molecule Deposition Chamber

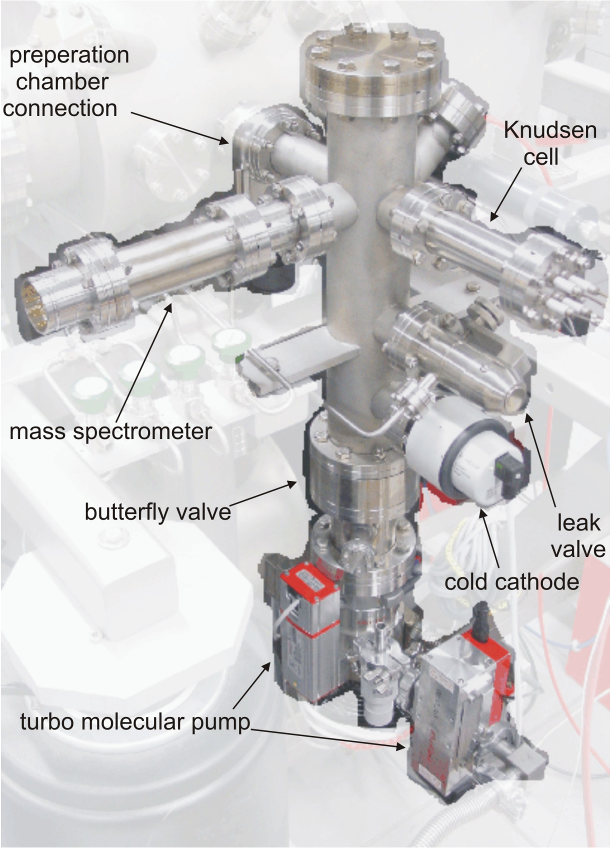

Figure 3.5: Image of the molecule deposition chamber.

In order to avoid the contamination of the main chamber, molecules are cleaned in a molecule deposition chamber and deposited from it. A gate-through valve (from *VAT*) separates the molecule deposition chamber from the preparation chamber for this purpose. The purity of the molecules is checked by a mass spectrometer QMA 200 (from *Pfeiffer*).

Molecules with high melting temperatures are loaded into a custom-built Knudsen cell. This cell is heated by direct current flow. Its temperature is controlled by a NiCr-Ni thermocouple spot-welded to the cell. The Knudsen cell can be replaced by a glass tube on a z-manipulator for the sublimation of molecules with low melting temperatures and/or high vapour pressures, as shown in Fig. 3.1.

The pumping unit consists of the same combination as the one found in the load-lock (see section 3.1.3). After baking, a final pressure of $1 \cdot 10^{-10}$ mbar is reached. The pressure is determined by a cold cathode pressure gauge (from *Pfeiffer*).

3.2 Sample Handling Instruments

In this section, the tools that are designed and constructed for the sample's transfer, preparation, and storage are presented.

The samples are mounted on a sample holder based on a commercial design from *Specs*. A drawback of the original sample holders is that they had no way of allowing the reading of a samples' temperature directly, which made a precise and reproducible sample preparation difficult for samples with low melting points.

To resolve this issue, I modified the *Specs* sample holder with a temperature control unit (see section 3.2.1) and constructed a heating stage unit (see section 3.2.2) compatible with it in order to read the annealing temperatures of the samples precisely.

The transfer of samples between the chambers is achieved by two custom-built extenders, one for the transfer rod and the other one for the manipulator head. A custom-built garage provides the storage of the samples and a spare tip.

3.2.1 Sample Holder

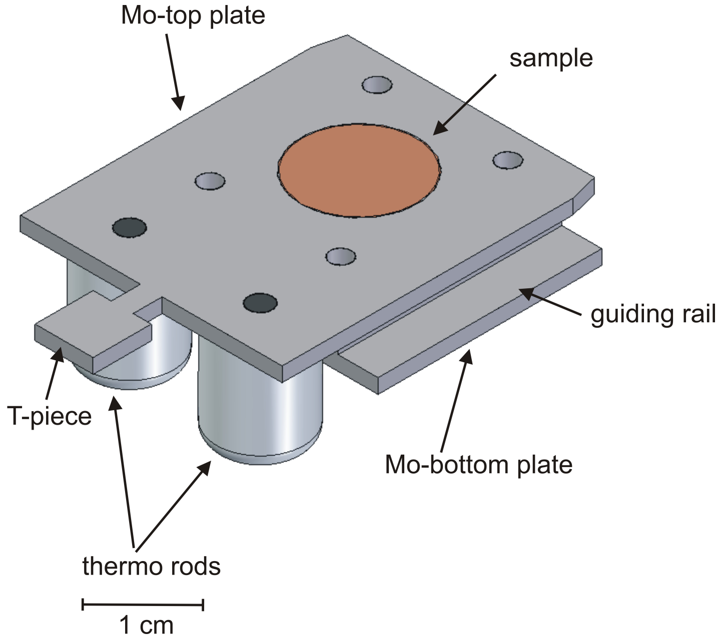

Figure 3.6: Sketch of the sample holder modified by thermorods.

The design of the sample holder allows us to control the temperature via NiCr-Ni thermo rods. As shown in Fig. 3.6, the sample holder is constructed from two Mo-plates that clamp a hat-shaped sample. The bottom plate has a hole in its center for electron bombardment to the back side of the sample and two guiding rails at its sides. These guiding rails are utilized for the storage of the sample holder in the sample garage, the heating stage, and the STM. The top plate has a hole for the sample and a T-piece for grabbing the sample holder by the manipulator. Other than the original design by *Specs*, I extended this upper plate by 6 mm. Two thermo-rods with diameters of 5 mm are screwed to this extension. Two thin NiCr-Ni thermo wires are spot-welded to these rods and onto the sample holder so that the sample is pressed against their end.

3.2.2 Heating Stage

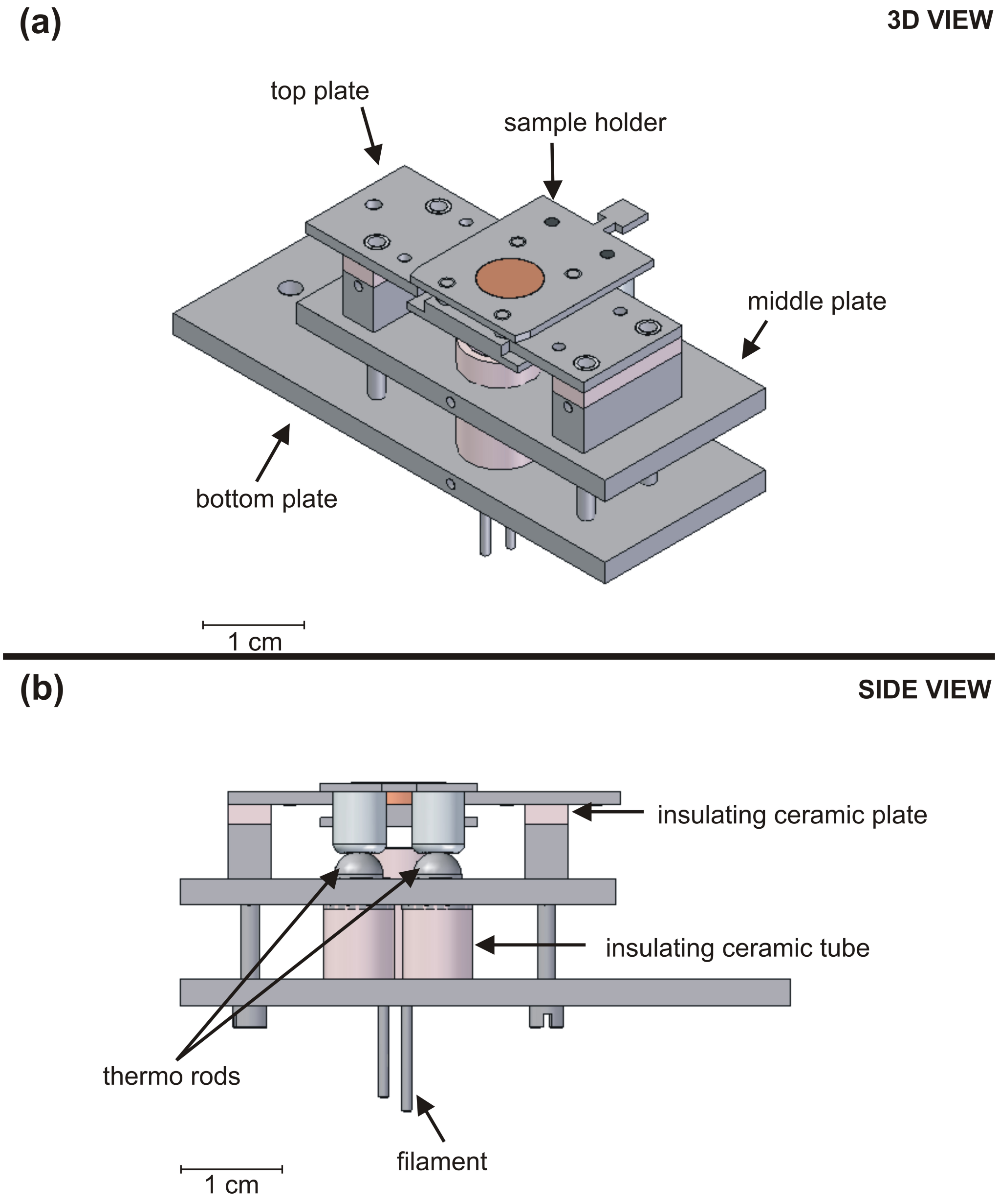

Figure 3.7: Sketch of the heating stage with sample (a) 3D view (b) side view.

The heating stage (see Fig. 3.7) uses electron bombardment to anneal the samples up to 1573 K. As shown in Fig. 3.7, the heating stage is made out of three differently sized titanium plates, which are screwed together but also electrically insulated from one other via ceramic tubes and plates. The low vapor pressure

of titanium, even at elevated temperatures, reduces possible contaminations of the samples during annealing. NiCr-Ni thermo-rods are used for contacting the thermorods of the sample holder. The thermorods of the heating stage are supported by two springs on the bottom. These springs provide the necessary flexibility to slide the thermorods at the sample holder above them. This allows a good galvanic contact between the thermorods of the heating stage and the sample holder. Two NiCr-Ni thermo cables are screwed to the bottom of the thermorods of the heating stage. These are connected to a feedthrough.
A positively polarized high voltage is applied to the top plate and is insulated from the rest via ceramic plates. By this way, the high voltage is applied to the sample. Thereby, a tungsten filament is utilized as an electron source and connected to the ground. The thermionic electrons emitted from the filament are accelerated towards the sample due to the high-voltage applied to the sample.
In a control measurement with a second thermocouple directly connected to a dummy sample holder, I determined that the deviation of the measured temperature to the true temperature is below 1% for annealing at 773 K and below 3% for annealing at 1273 K.

3.2.3 Manipulator Extention

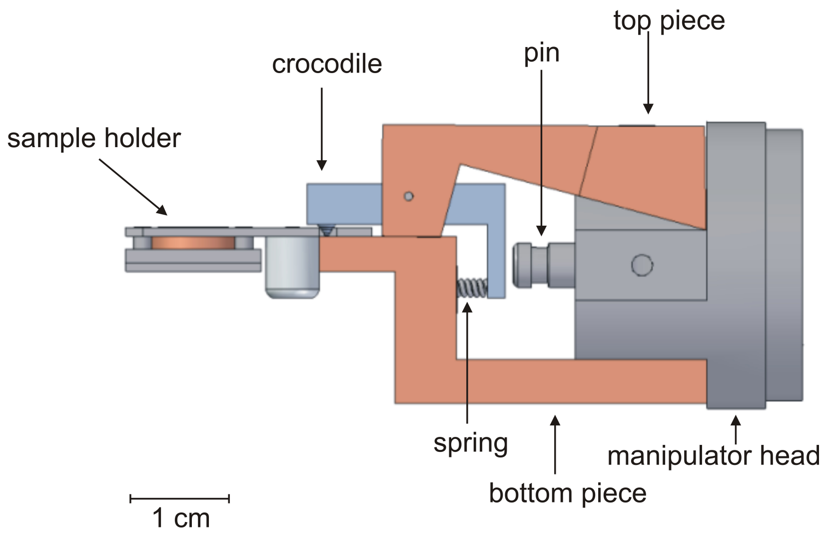

Figure 3.8: Sketch of the manipulator extention.

A custom built manipulator extention is used to grab the sample holder or the tip holder during their transfer between chambers.

The manipulator extender (see Fig. 3.8) is composed of Cu top and Cu bottom pieces. These are screwed to the manipulator head and are insulated electrically by ceramic tubes and a Kapton foil. A crocodile clamp is used to grab the sample holder and the tip fork at their T-pieces.

The opening and closing of the crocodile clamp allows for the grabbing of the sample holder or the tip fork and is supported by a spring mechanism. A linear drive moves a pin mounted to the manipulator (see Fig. 3.8) backwards and forwards. If this pin pushes the crocodile clamp at its end, the front part of the clamp rises up. The retraction of the pin releases the crocodile clamp and the spring mechanism pushes the clamp to its original position. The clamp thus grabs or releases the sample holder.

The sample holder has an electric contact via a feedthrough of the manipulator. This contact is used to read the emission current during the sputtering process.

3.2.4 Transfer Rod Extention

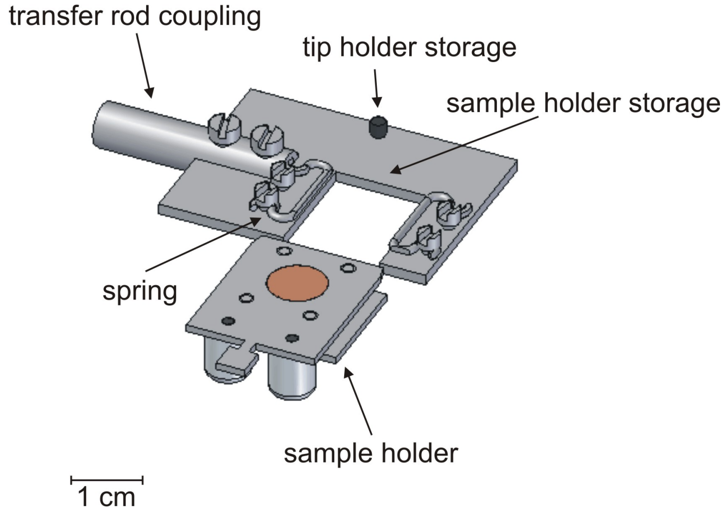

Figure 3.9: Sketch of the transfer rod extention.

The stainless steel transfer rod extention (see Fig. 3.9) is used to store the sample holder and the tip holder in the load lock.

The sample holder is stored into the extention via its guiding rails. Two springs mounted to the extention allow the sample holder to be fixed tightly in place. The tip holder is held by a magnet glued non-conductively to the extention.

3.2.5 Sample Garage

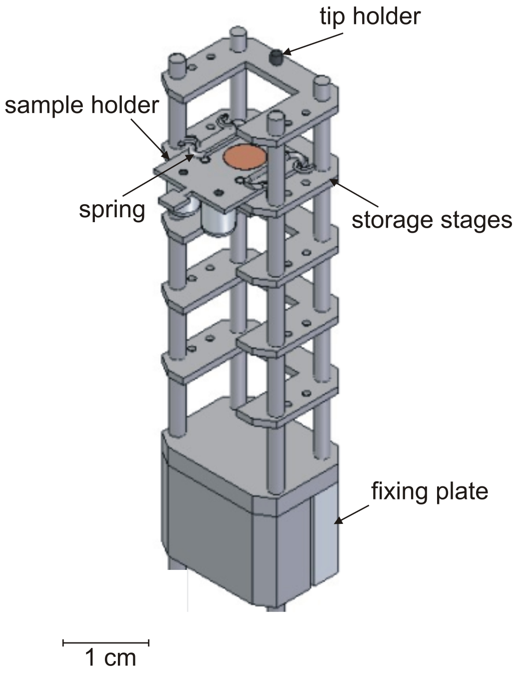

Figure 3.10: Sketch of the sample garage.

A custom-built sample garage (see Fig. 3.10) is made of four stainless steel stages to store four sample holders and a platform with a magnet glued insulating onto it for storing a spare tip. The sample holders are stored in the stages via their guiding rails and fixed tightly in place by the two springs mounted at each stage. The sample garage is able to move backwards and forwards in the z-direction by the use of a push-pull mechanism mounted to the fixing plate.
With its compact design it is possible to mount the sample garage through a CF 35 flange.

3.2.6 Tip Holder

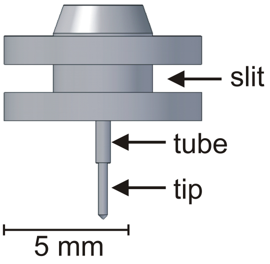

Figure 3.11: Sketch of the tip holder.

The tip holder (see Fig. 3.11) is used to fix the tungsten tips. The tip holder is fixed in place by magnets; it is for this reason that it is made out of Ni.
The tip holder consists of a tube in the center surrounded by a slit. The tungsten tips are fixed to the tube in the center of the tip holder. The slit is used to grab the tip holder during its transfer.

3.2.7 Tip Holder Fork

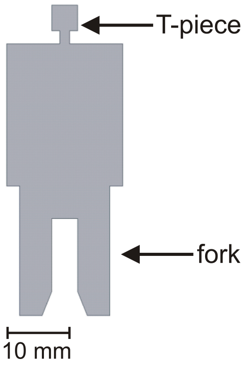

Figure 3.12: Sketch of the tip holder fork.

The tip holder fork (see Fig. 3.12) is a modified version of the top plate of the sample holder. It consists of a fork in the front, which is used to grab the tip holder from its slit.
The T-piece enables the manipulator extention to grab the tip holder like the sample holder.

3.3 Multi-scale Scanning Tunneling Microscope

In this section, the multi-scale STM's technical elements, design, operation principle, and damping system are described.
The idea of constructing a multi-scale STM resulted from the desire to investigate atomically-sized structures with respect to their large-scale environments on surfaces pre-structured on the micro- or nanometer scales, e.g. micro-pillars for LEDs or LDs or molecules adsorbed on semiconducting pillars to change their band gap. The construction was realised by the combination of two different stages: A commercial piezo stage for a scan range from 450 μm x 450 μm to 7 μm x 7 μm (see section 3.3.3) and a custom-built beetle type STM (see section 3.3.2) for scan areas from 5 μm x 5 μm down to nanometer resolutions. The possibility of scanning on all scales is made possible by the use of two different but continuously cooperating systems (see section 3.3.4). Since STMs are extremely sensitive to noise, mechanical noise sources are filtered by a combination of three damping systems (see section 3.3.5), with each system filtering different frequency ranges.

3.3.1 Technical Elements

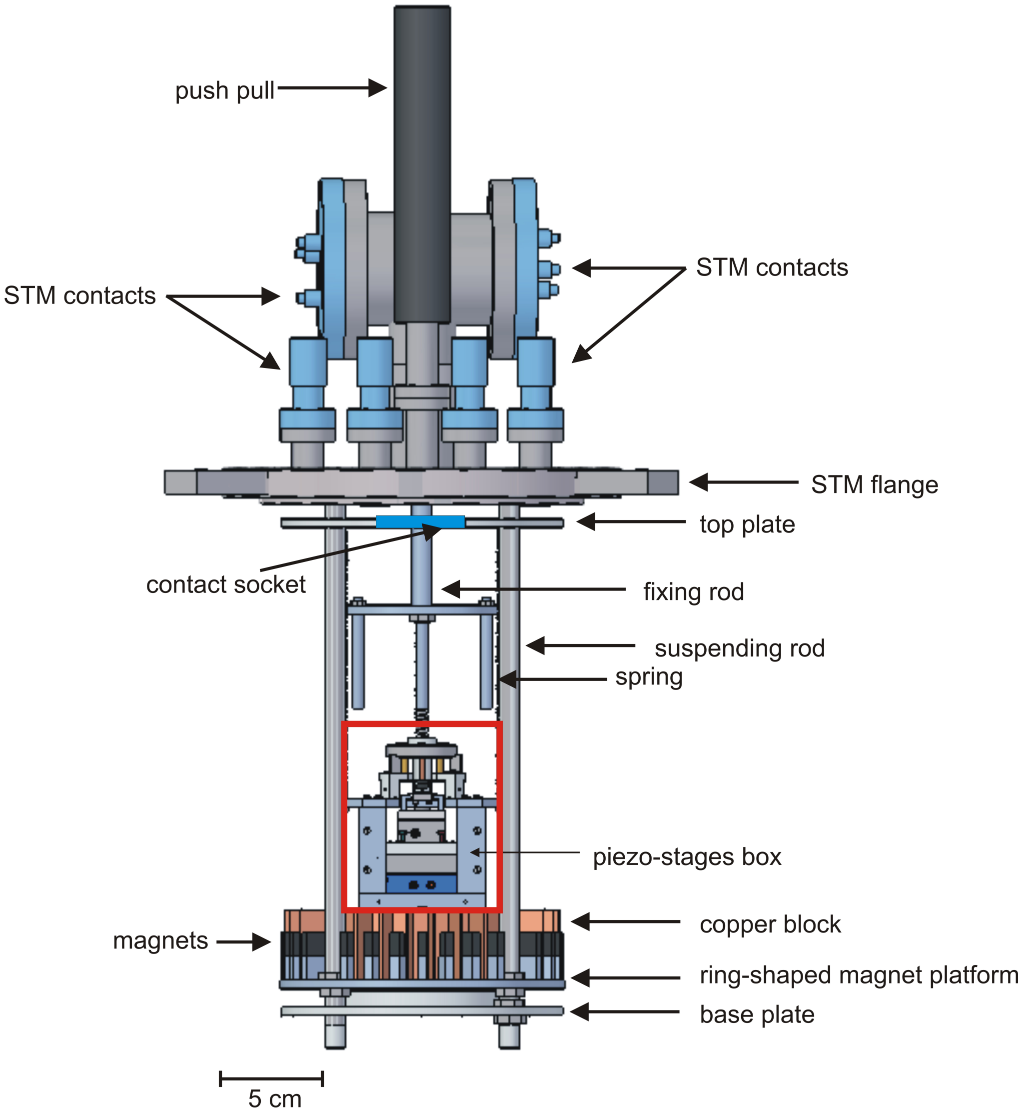

Figure 3.13: Front view of the multi-scale STM.

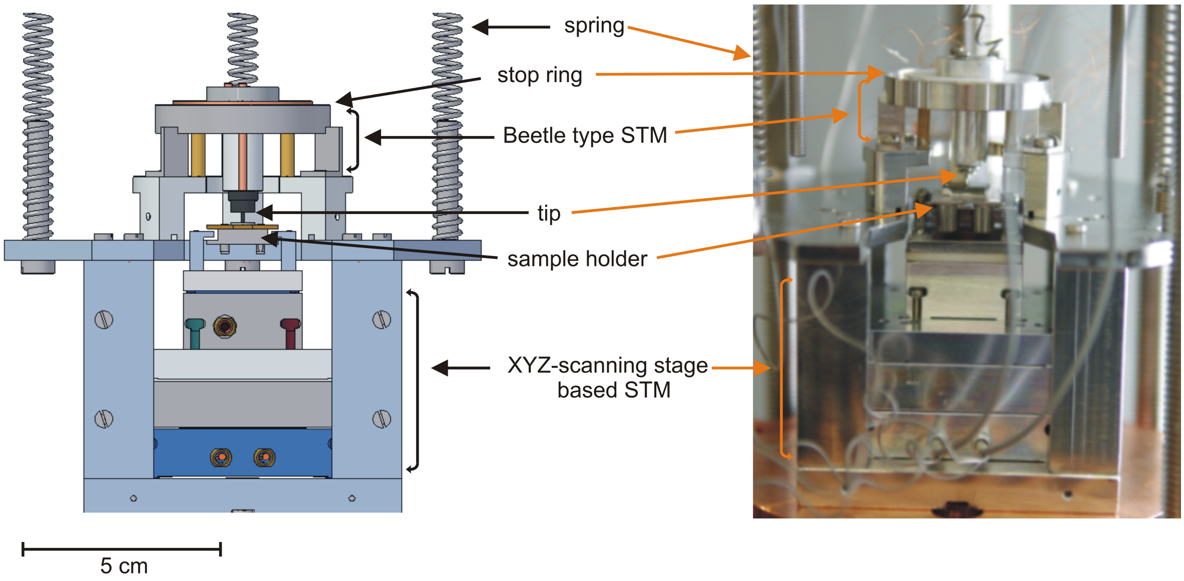

Figure 3.14: Front view of the two stages of the multi-scale STM: the XYZ-scanning stage-based STM and the beetle-type STM.

The multi-scale STM is mounted on a CF 200 flange, as shown in Fig. 3.13. Four stainless steel suspending rods are used as the main supporting elements, and are screwed to the vacuum side of the STM flange. The stainless steel top plate, the base plate, and the magnet platform ring are fixed to the suspending rods, whereas the combination of the piezo-stages box and the copper block levitates freely on the top plate via three suspending springs. The beetle-type STM is constructed on top of the stainless steel piezo-stages box and the XYZ-scanning stage-based STM is mounted inside of it, as illustrated in Fig. 3.14.

Since the STM levitates freely on springs during operation, it is necessary to fix it in place during sample or tip transfer. The tripod-shaped fixing rod connected to a push-pull at the center of the STM flange is used for this purpose. The push-pull mechanism (see Fig. 3.13) moves the fixing rod up and down. With the downward movement of the push-pull, the STM is pushed downwards onto the base plate. It is fixed by locking the push-pull mechanism. By unlocking it, the STM is released and levitates freely.

The electrical feedthroughs at the STM flange serve as contacts for both STM stages. The contact socket mounted at the top plate is used as an interface for electrical contacts, which is explained in detail in section 3.3.2. The pre-amplifier is attached directly to the tunneling current feedthrough as shown in Fig. 3.3.

3.3.2 Beetle Type STM

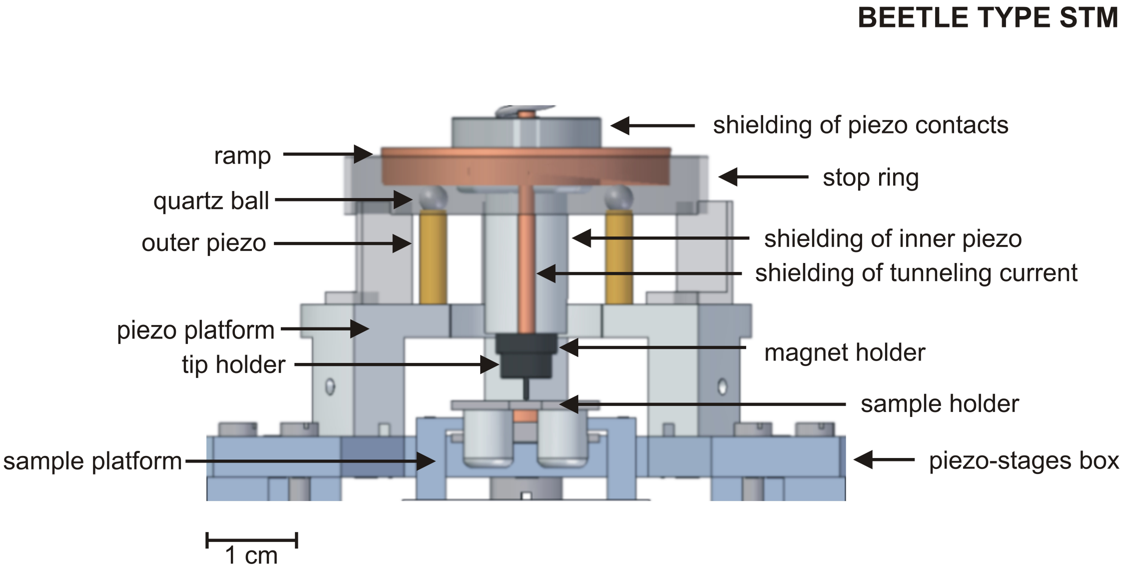

Figure 3.15: Front view of the beetle-type STM.

The beetle-type STM (see Fig. 3.15) is based on an established design by G. Meyer [34]. It consists of three outer piezos, one inner piezo, and a ramp. The ramp, with a slope of 2^o, is used in connection with the three outer piezos as a coarse approach mechanism. It is also used to allow the tip's motion in the two horizontal directions. Its operation method is explained in more detail in section 3.3.4. In contrast to the original design by Besocke [11], the inner piezo is connected to the ramp, while the sample is mounted on a sample platform, which is screwed to the Z-stage of the XYZ-scanning stage-based STM. As illustrated in Fig. 3.15, the sample is mounted on top of the piezo-stages.

The ramp rests on top of the outer piezos by gravity. It is insulated via sapphire balls, which are glued on top of the outer piezos. The three outer piezos are glued to the top of the piezo platform, whereas the inner piezo is glued to an aluminium disc that is screwed to the ramp (see Fig. 3.16). This aluminium disc serves as an electrical shield and as a guide for the contact wires of the inner piezo. An aluminium tube surrounding the inner piezo is used to shield the inner piezo and the tunneling current wire electro-magnetically. A stop ring (see Fig. 3.15) surrounds the ramp to avoid its falling down during the horizontal motion. The glue used here is an insulating glue.

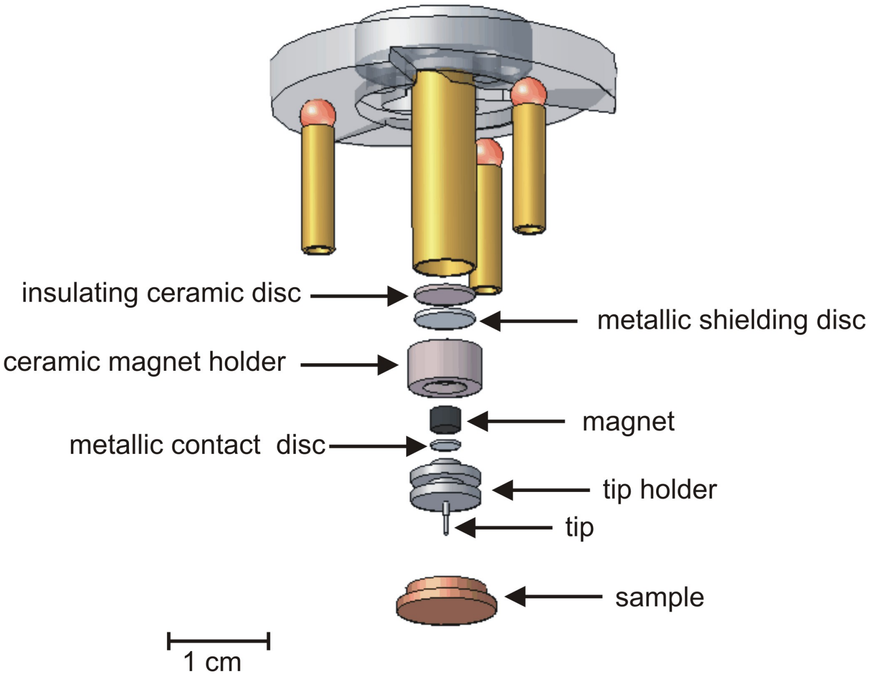

Figure 3.16: Details of the inner piezo that holds the tip.

Fig. 3.16 shows the parts that are mounted on the inner piezo in order to attach the tip. As the tunneling current is measured via a cable connected to the tip holder, specific care for electrical shielding and against cross talk is necessary. The inner piezo is electrically insulated by a ceramic disc fixed to its end. Cross talk between the inner electrode and the tunneling current are suppressed by a shielding disc glued to this ceramic disc. A ceramic magnet holder with a hole in the center is fixed to the shielding disc by insulating glue. A magnet is fitted into its hole, and a metallic disc is glued to the magnet. To this disc, the tunneling current wire is soldered. The tip holder is a magnetic metal, which is held by magnetic force to the metallic disc. Fixing is done by an insulating glue, if not mentioned otherwise.

3.3.3 XYZ-scanning Stage Based STM

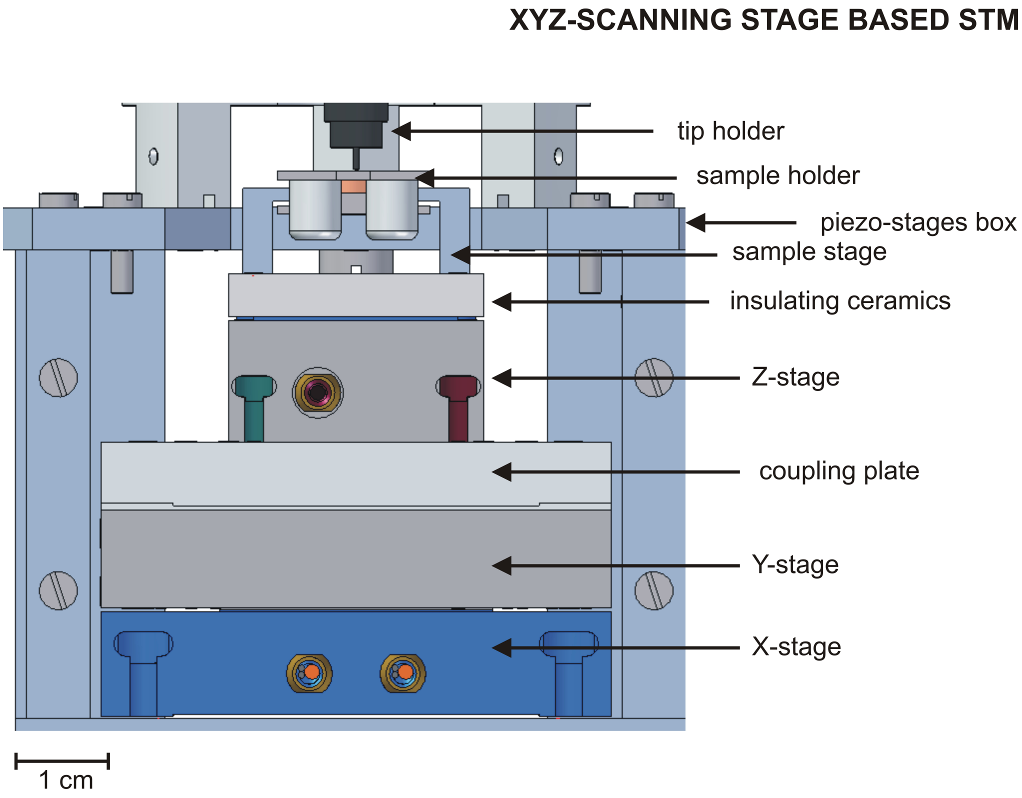

Figure 3.17: Front view of the XYZ-scanning stage-based STM.

The XYZ-scanning stage is based on a commercial nanopositioning and scanning system with frictionless flexure guidance (from *Physical Instruments*). The piezo-driven flexure nanopositioners provide resolutions on the nanometer scale despite their increased travel ranges. The flexure motion depends on an elastic deformation of a solid material, while the elimination of friction and the stiffness of the flexures provide resistance against vibration. The nanopositioning systems are driven via the commercial electronic that is driven by ±10 V from the computer.

Due to its large travel range, the XYZ-scanning stage-based STM is used for large scan ranges. It is situated in the piezo-stages box as shown in Fig. 3.17. The XYZ-scanning stage-based STM consists of three stages. The X- and Y-stages scan areas of up to 450 μm x 450 μm, whereas the Z-stage has a range of 50 μm. An aluminium plate couples the X- and Y-stages to the Z-stage. The sample platform for the sample holder are screwed on top of the Z-stage and are insulated electrically from it via a ceramic plate. During the STM measurements, the sample holder is fixed onto the two sample stages by two tungsten springs. The bias voltage wire is soldered to the sample platform.

3.3.4 Operating Principle of Multi-scale STM

The multi-scale STM provides the motion of the tip with respect to the sample or the motion of the sample with respect to the tip in x-,y-, and z-directions by its two scan units, respectively. The beetle-type STM can translate the tip up to 8 mm in the x- and y-directions and up to 1.2 mm in the z-direction by the combination of the outer piezos and the ramp. The XYZ-scanning stage-based STM can translate the sample up to 450 μm in the x- and y- directions using the XY-stage and up to 50 μm in the z-direction using the Z-stage. Finally, the beetle-type STM can translate the tip by 5 μm in the x- and y-directions and by 500 nm in the z-direction without slipping of the ramp.

The coarse approach of the tip to the sample is achieved via the beetle-type STM. The XYZ-scanning stage is deactivated during this process. The ramp is rotated down using slip-stick motion. For this, a triangular voltage ramp is applied to the outer electrodes of the outer piezos. A voltage of 75 V leads to steps of 34 nm in z-direction. During the final automatic approach, the inner piezo is extended after each step by 500 nm in the z-direction while searching for a tunneling current signal. It is retracted back before the next step.

The multi-scale STM provides three scanning possibilities. The beetle-type STM may scan with its inner piezo or its outer piezos. The maximum scan area of the beetle-type STM is limited to 5 μm x 5 μm. The XYZ-scanning stage-based STM utilizes the XY-stage for this purpose. The Z-stage is necessary to avoid losing tunneling contact during the scanning of large-scale images. The strength of the beetle-type STM is that it has resolutions in sub-nanometers, whereas the XYZ-scanning stage-based STM provides the 0.45 millimeter-scale scans. The software (see section 3.4.2) of the multi-scale STM allows it to switch between those scan units for different magnifications. For example, after recording a 0.45 millimeter scale image by using the XY-scanning stages, it is possible to magnify further to any chosen point on the image down to 7 μm by the XY-scanning stages and then switch to the beetle-type STM for nanometer resolutions without losing the tip position. The reverse procedure, from nm scale scanning up to a 0.45 mm scale scanning, is likewise possible.

All images are recorded in constant current mode. The regulation of the tip-sample distance is achieved by the inner electrode of the inner piezo. After comparing the measured tunneling current value with a set value, the voltage to the inner electrode of the inner piezo is adapted to keep the current constant by use of a necessary tip-sample displacement. This z-signal is controlled by a feedback loop with three parameters: a proportional gain, an integral gain, and a derivative gain. At the same time, the XYZ-scanning stage-based STM utilizes the integrated z-signal as an input signal to adapt the voltage at the Z-stage. This is achieved by a second feedback loop. The Z-stage value is adapted so that the z-variations of the inner piezo are (nearly) symmetrical around its relaxed value (at 0V). The feedback loop of the beetle-type STM operates on a faster time scale than the feedback loop of the XYZ-scanning stage-based STM. In this way, the feedback loops do not work against each other during their simultaneous operation.

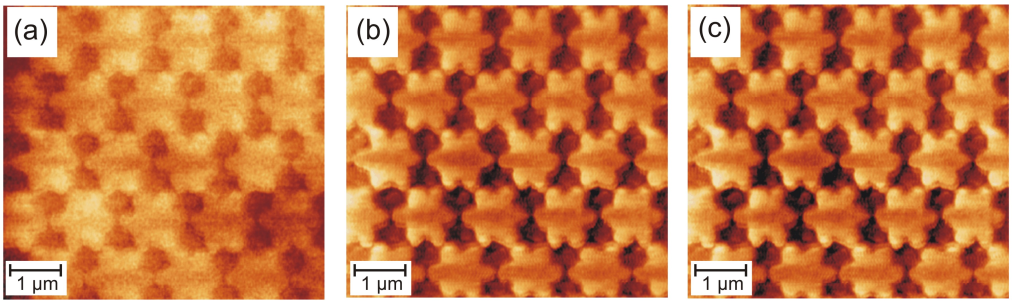

Figure 3.18: Images recorded during operation of the XYZ-scanning stage based STM. a) image produced by using the z-signal of the Z-stage of the XYZ-scanning Stage Based STM. b) image produced by using the z-signal of the beetle-type STM. c) Image produced by adding the z- signal of the beetle-type STM and the Z-signal of the Z-stage. The tunneling parameters are: I = 0.153 nA, V = -3.615 V.

The XYZ-scanning stage based STM produces images by using two different input signals. The first signal is the z-signal of the beetle-type STM. The second one is the z-signal of the Z-stage of the XYZ-scanning stage based STM. Fig. 3.18 shows three different images recorded during scanning with the XYZ-scanning stage based STM. In Fig. 3.18a the z-signal of the Z-stage is reproduced. In this image, the contours of the star-shaped micro-pillars are not very sharp. Fig. 3.18b shows an image based on the z-signal of the beetle-type STM. This image shows sharper contours and is less noisy compared to Fig. 3.18a. Fig. 3.18c shows an image, which results from summing Fig. 3.18a and Fig. 3.18b. For the lateral resolution of the structures it is better to use the z-signal of the beetle stage (Fig. 3.18b) because the faster feed-back loop leads to an increased resolution. However, to get reliable information about the height of the structures it is necessary to add the both signals (Fig. 3.18c).

Within this work, the images shown are based on the z-signal of the beetle stage. The height profiles are determined by adding the z-signal of the beetle-type STM and the z-signal of the Z-stage.

3.3.5 Damping Systems

The low noise level of the multi-scale STM results from a high mechanical stability, a very rigid design, a construction using compact components with short mechanical connections, and a large mass (8 kg). Finally, the wires utilized for the electrical contacts of the piezos are prevented from hanging loosely and external noise sources are reduced as much as possible. The multi-scale STM also achieves a low noise level from the combination of four damping systems, each described in more detail later in this section: sand boxes, pneumatic feet, suspending springs, and Eddy current damping.

3.3.5.1 Sand Boxes and Pneumatic Feet

As shown in Fig. 3.1, the UHV chamber rests on four pneumatic feet (*Newport*) with each foot placed in a box filled with sand. The pneumatic feet and sand boxes filter low-frequency oscillations (some Hz) originating from the floor as well as from the building. The sand insulates the pneumatic feet, and thus the chamber, from the vibrations transported via the floor. The pressure within the pneumatic feet determines the efficiency of the damping; a higher pressure leads to a quicker damping.

The pneumatic feet are also used for the horizontal alignment of the chamber with respect to the floor. This alignment is necessary for the STM to hang freely and for the approach mechanism to work properly.

3.3.5.2 Suspending Springs

While the pneumatic feet and sand boxes suppress low-frequency noise, the suspending springs (see Fig. 3.14) dampen the oscillations from some tens to some hundreds Hz in the perpendicular direction. These custom-made springs are constructed so that they extend up to three times their original length under the weight of the STM. They are attached to the top plate with Marcor screws for electrical insulation. The screws are also used to adjust the height and the alignment of the STM.

3.3.5.3 Eddy Current Damping

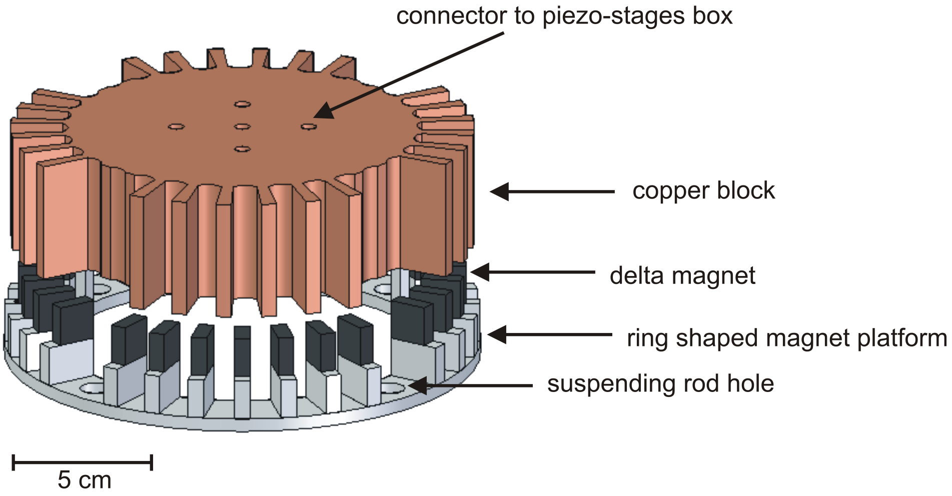

Figure 3.19: Sketch of the Eddy current damping.

Finally, the Eddy current damping serves to filter the high-frequency oscillations in the hundreds of Hz range but in the direction of horizontal and torsional motion. As shown in Fig. 3.19, it is composed of three parts: a rigid copper block, 28 delta magnets of 10 mm x 10 mm, and a ring-shaped magnet platform made out of stainless steel. The ring-shaped magnet platform is fixed to the four suspending rods (see Fig. 3.13). The Cu block is screwed to the piezo-stages box and levitates freely with the STM on the suspending springs (see Fig. 3.13). The delta magnets are fixed to the magnet platform by an insulating glue. Their

height and the alignment are adjusted by the nuts, which fix the ring-shaped magnet platform to the suspending rods.
The damping strength is defined by the amount, by which the magnets reach into the copper block. The best damping values are achieved by lowering 2/3 of the magnets into the block.

3.4 Controller and Software of the Multi-scale STM

The multi-scale STM, consisting two different scan units, requires a combination of various controllers and a software with two interfaces.
The controller of the multi-scale STM is a network-attached controller. The advantage of the current STM controller over more traditional designs is that the time-critical control tasks are distributed to an arbitrary number of subunits addressed over a TCP/IP communication protocol. Each subunit is configured with a master control software. A direct communication link between a specific subunit and the host software is only necessary for continuous data acquisition. Each subunit is based on a compact-RIO control system developed by *National Instruments* and features a real-time controller combined with a field-programmable gate array (FPGA).

3.4.1 Controller of the Multi-scale STM

The multi-scale STM utilizes a controller and a relay-box combination for the beetle-type STM and an extra controller for the XYZ-scanning stage-based STM. The basic element of each controller unit is the Compact-RIO control unit. This embedded system consists of a real-time controller, a FPGA, and interchangeable I/O-modules. A power supply and HV-amplifiers are connected to the Compact-RIO to complete the controller.
Four independent input signals are recorded by the system's analog-to-digital converters (ADC). Additionally, six output signals are produced by digital-to-analog converters (DAC). The output signals are used to drive the piezoelectric actuators for translating the tip over the sample as well as for scanning and approaching. Each controller contains a PID-type feedback loop implemented to the FPGA for standard operations.
The main controller is responsible for memorizing the position of the tip with

high precision and reliability. When scanning with the XYZ-scanning stage-based STM, the main controller must continue to read the tunneling current signal and to regulate the z-signal. It must also communicate with the XYZ-scanning stage-based STM controller and save the tip's positioning data.

The relay box is directly connected to the main controller via a sub-D socket and is responsible for the translation and the rotation of the ramp by sending signals to the responsible piezo electrodes of beetle-type STM. It is also used to give the user the opportunity to choose either the inner piezo or the outer piezo as a scanning unit.

3.4.2 Software of the Multi-scale STM

The multi-scale STM's software needs to perform two types of tasks. The first type is the command tasks, which autonomously control the STM's parts. The second type is the data acquisition tasks, which read and store data acquired from the multi-scale STM. The source code is developed in the visual programming language G.

A complete set of control parameters is stored, enabling the real-time system to operate independently from the software. The communication between the software and the real-time system is achieved by a transmission control protocol and an internet protocol (TCP/IP) over a local area network (LAN).

The software provides a user interface to access the controllers of the beetle-type STM and the XYZ-scanning stage-based STM, the control parameters of which are managed simultaneously. However, the data acquisition is restricted only to one controller at a time. The software is designed as two interfaces, with each interface providing a control environment for one of the scan heads.

The host PC is responsible for the application of user commands such as host variables, image memory, HV data, and ramp data. The actual STM parameters–set point, coarse approach, scan ramps etc.–are saved here. These parameters can be loaded either by a real-time system or by the host PC after starting the software. The host PC communicates with the real-time system via an ethernet.

3.4.3 Implementation of the controllers and the Software

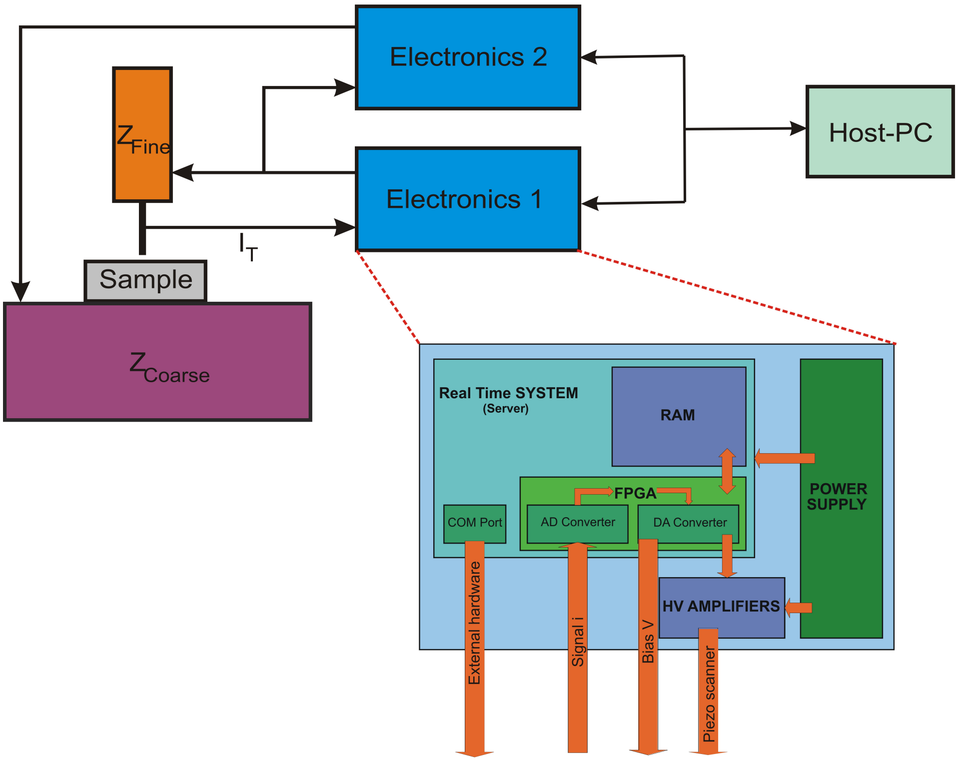

Figure 3.20: Skecth of the working principle of the multi-scale STM and the electronic box. (Sketch by C. Zaum)

The implementation of the controllers and the software is shown in Fig. 3.20. Different than regular STMs, the multi-scale STM is regulated by two cooperating feedback loops. The feedback loop signal is distributed between the z-actuators of the two scan units. These two independent feedback loops, on different controllers, regulate the distance between the tip and the sample.

The input signal for the controller of the beetle-type STM is the tunneling current (I_t). The feedback loop of the beetle-type STM controller is responsible for adjusting the distance between the tip and the sample by driving the z-actuator, labeled as Z_{Fine}. Simultaneously, the feedback loop of the XYZ-scanning stage-based STM controller utilizes the integrated z-signal as an input signal and drives the Z-stage, labeled as Z_{Coarse}. The Z-stage value is adapted so that the z-variations of the inner piezo are (nearly) symmetrical around its relaxed value (at 0V).

In order to avoid the feedback loops working against each other during their simultaneous operation, the feedback loop of the beetle-type STM controller operates on a faster time scale than the feedback loop of the XYZ-scanning stage-based STM controller.

Chapter 4

Proof of Principle

4.1 Experimental Details

In this chapter, the operating principle of the multi-scale STM is illustrated by two different systems. The first system consists of two types of gallium nitride (GaN)-based microstructures with two different shapes: rods and stars. The rod-shaped micro-pillars have diameters of about 2.2 μm, a center-of-mass distance of 2.5 μm, and heights of around 400 nm. The star-shaped micro-pillars have a circumcircle diameter of around 1.3 μm, a center-of-mass distance of 1.4 μm, and heights of around 400 nm. On these systems, the different scanning ranges are demonstrated. The second system–the herringbone reconstructed Au(111) [35]–is used to demonstrate the nm scale resolution capability of the multi-scale STM.

The GaN-based micro-pillars are fabricated by deep dry etching [36] at the Technical University of Braunschweig in the group of Prof. Waag. After being transferred into the UHV chamber, the sample is annealed by electron bombardment at $I_{filament} = 2.5$ A, $I_{emmision} = 12.5$ mA, and $V_{high} = 1$ kV for 5 h to a temperature of 828 K. This degassing of the sample is checked *in-situ* by a quadruple mass spectrometer. The commercial Au(111) crystal from *Matek* is prepared by two cycles of 1.3 keV Ar^+ sputtering at $P_{Ar} = 5 \cdot 10^{-5}$ mbar for 65 and 30 min, respectively, followed by annealing at 918 K for 30 min.

4.2 Gallium Nitrid-based Micro-pillars

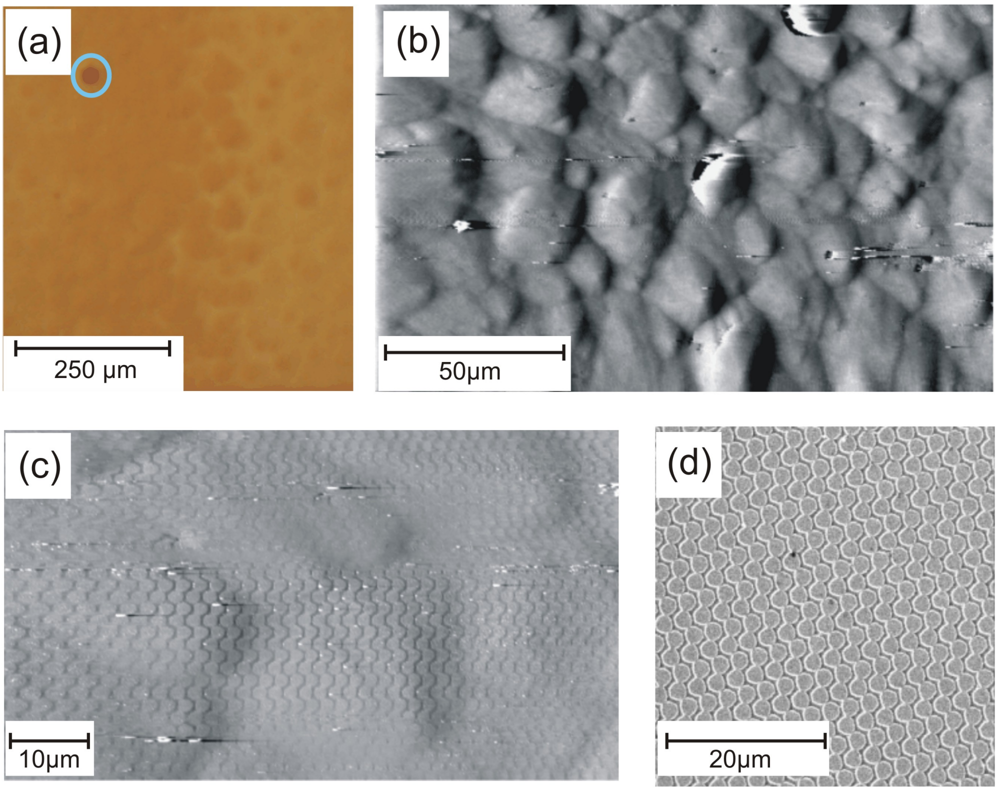

Figure 4.1: Overview images of GaN-based sample: (a) light microscope image. Circle marks a defect on the sample (b) multi-scale STM image recorded by XYZ-scanning stage-based STM showing large roughness on the surface. Variation of the structures are result of creep that depend on the scanning speed. The tunneling parameters are: I = 0.15 nA, V = -3.8 V (c) XYZ-scanning stage-based magnification of (b). The tunneling parameters are: I = 0.15 nA, V = -3.8 V d) SEM image by L. Kühnemund.

Fig. 4.1 shows images of rod-shaped pillars as recorded by different instruments. A light microscope image (see Fig. 4.1a) of the sample shows some imperfections on the sample. However, it is not possible to resolve the micro-pillars on this scale. A spot can be chosen on any part of the sample as identified by a light microscope image. A large-scale image with a side length of 173 μm is recorded by the XYZ-scanning stages of multi-scale STM is shown in Fig. 4.1b. The image also demonstrates the large dynamic range of the multi-scale STM with a distance between the highest and the lowest point of the image of 116 nm.

Such a large scale image facilitates to choose a region of the surface that is suitable for further investigations. At larger magnification, the micro-pillars are resolved (Fig. 4.1c). In this example, etching caused a closely-spaced row of pillars separated by grooves. In Fig. 4.1d I compare the STM image to a SEM image. This reveals the same etching characteristic as the STM image. The STM image, however, gives additional information about the average roughness of the surface, in Fig. 4.1b 15 nm.

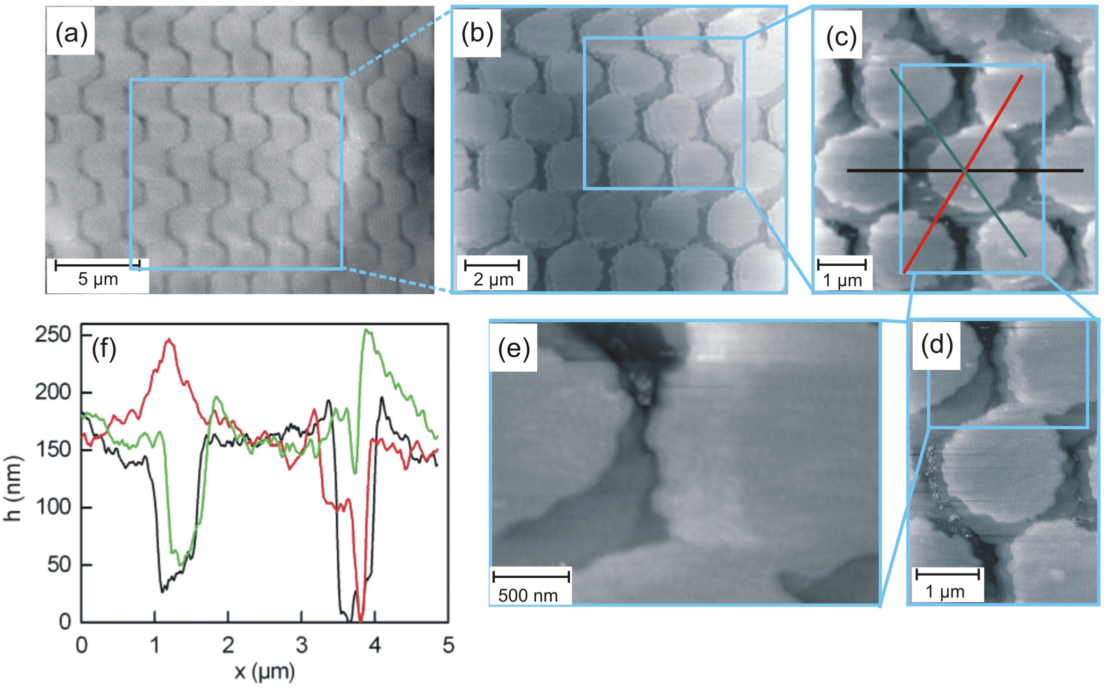

Figure 4.2: Magnification series of rod-shaped GaN-based micro-pillars: (a-c) images produced by the XYZ-scanning stage-based STM. (d-e) images produced by the beetle-type STM. The tunneling parameters are: I = 0.153 nA, V = - 3.8 V (f) line scan along the three directions shown in (c). Variation of the structures are result of creep that depend on the scanning speed.

As shown in Fig. 4.2, the possibility to alternate between the two scanning units at the same sample spot is demonstrated by a series of images. First, three images of increasing magnification are scanned by the XYZ-scanning stage (Fig. 4.2a-c), then two images are scanned by the beetle-type STM (Fig. 4.2d, e). On the largest image (Fig. 4.2a), the rod-shaped micro-pillars are clearly visible. Also observed (see Fig. 4.1) fact is that the pillars are not etched homogeneously in both directions. The gap between the pillars on the image is considerably larger in horizontal direction than in the vertical direction. The inhomogeneous distribution of the spacing between the pillars is further demonstrated by three line scans along three different directions, as shown in Fig. 4.2f. Further magnifications, first by the XYZ-scanning stage and later by the beetle-type STM (e.g. Fig. 4.2c and d) reveal differently etched layers. The top structure is ≈ 150 nm deep. An additional layer is edged a smaller amount. The remaining gap is so narrow that the tip reaches only few nm into this gap (see green line scan in Fig. 4.2f).

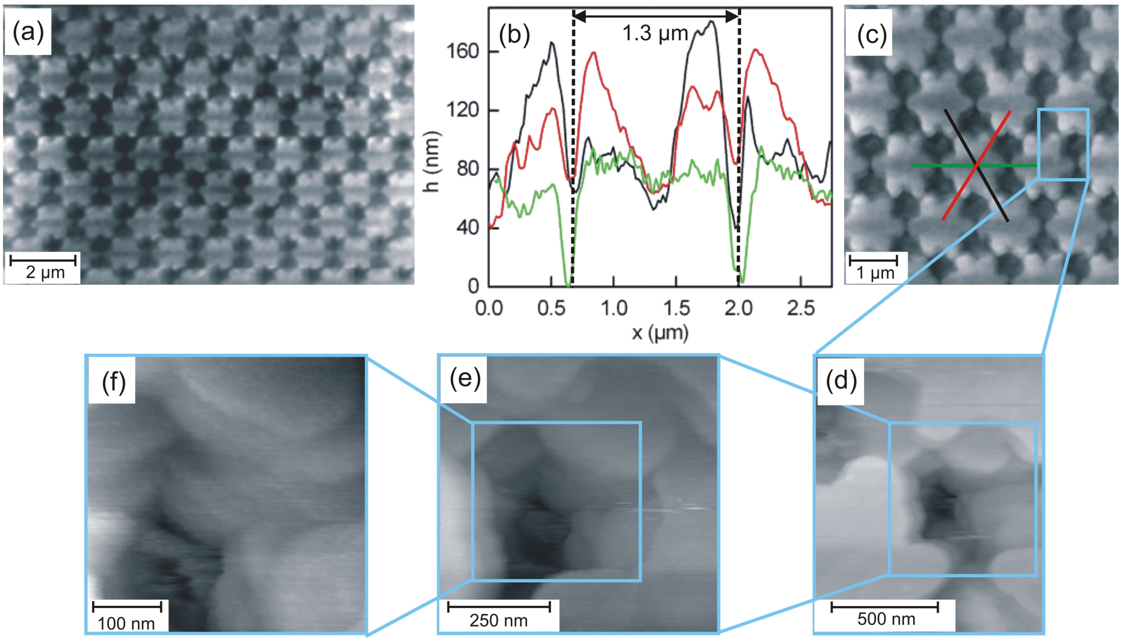

Figure 4.3: Magnification series of star-shaped GaN-based micro-pillars: (a-c) images produced by the XYZ-scanning stage-based STM. The tunneling parameters are: I = 0.153 nA, V = -3.615 V. (d-f) imaged by the beetle-type STM. The tunneling parameters are: I = 0.2 nA, V = -3.8 V.

On a different part of the same micro-structured sample, an underetching of the hexagonal mesh results in star-shaped pillars. A magnification series of these structures, as shown in Fig. 4.3, range from a 13 μm side length image to a 410 nm side length image. The first two images are recorded by the XYZ-scanning stage (Fig. 4.3a-c) and the last three images by the beetle-type STM (Fig. 4.3d-f). Fig. 4.3a illustrates an overview image recorded. A six-fold symmetry of the pillars as well as a homogeneous distribution of the spacing between the pillars is observed. These show no marked asymmetry in etching. At the largest magnification (Fig. 4.3f), the edges of the pillars show layers indicating different etchings of the edges in different layers. Fig. 4.3b shows three line scans taken along three different directions on the pillars in Fig. 4.3c. According to line scans, the star-shaped pillars have a circumcircle diameter of 1.3 μm.

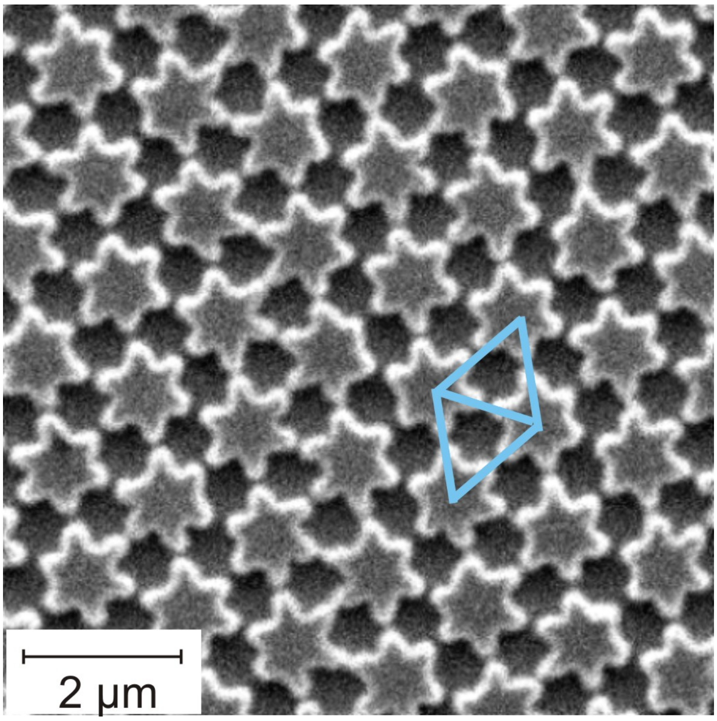

Figure 4.4: SEM image of star-shaped pillar used for the purpose of calibrating the multi-scale STM. A unit cell is indicated; image by L. Kühnemund.

Both stages of the multi-scale STM are calibrated by comparing a calibrated SEM image with STM images of the star-shaped pillars. Fig. 4.4 shows a SEM image. According to the SEM image, the three different directions of a hexagonal lattice of the pillars have a distance of: (1.40±0.15)μm, (1.42±0.26) μm, and (1.41±0.17) μm. Those values measured at a SEM image are then compared to the respective pillar distances in a STM image. The calibration factors for the x- and y-directions are calculated by using the respective ratios of these lattice distances. With these correction factors the piezo calibration constants for the beetle-type STM are determined to be: (33.8±0.55) nm/V in x-direction and (34.4±0.11) nm/V in y-direction. The XYZ-scanning stage-based STM controller uses the voltages of V_{comp} =±10V from the computer. For these voltages magnifications are: (19.3±1.60) μm/V_{comp} in the x-direction and (27.5±0.62) μm/V_{comp} in the y-direction.

One of the reasons of the uncertainity at the calibration constants is the creep at piezos arising from high scan speeds. The second one is the variations at the sizes of the pillars.

4.3 Au(111) Crystal

On the reconstructed Au(111) crystal, I demonstrate the smallest structures resolved so far by the multi-scale STM. Gold belongs to the face-centered-cubic noble metals with a fully occupied d band. Different from the other noble metals, the Au(111) surface does not terminate by an ideal (111) face but rather reconstructs into the characteristic "herringbone" pattern. In brief, the reconstruction is characterized by a $(22 \text{ x } \sqrt{3})$ unit cell. In this unit cell, the gold atoms on the top most surface layer are compressed gradually up to ≈4.2% along the $[1\bar{1}0]$ direction. This contraction leads 23 surface gold atoms to be distributed among 22 bulk sites in the unit cell, which results in alternating fcc and hcp stacking regions that run parallel to the $[11\bar{2}]$ direction [37, 38]. The Au atoms located near bridge positions form dislocation lines that separate the fcc from the hcp areas. The domain boundaries are presented approximately every 14 nm by long-range elastic relaxations [39]. At these boundaries, the domains bend by $\pm 120^o$. It is because of this that the zigzag pattern–pointed as the "herringbone"– reconstruction forms. The herringbone structure is sensitive to defects such as step edges [38].

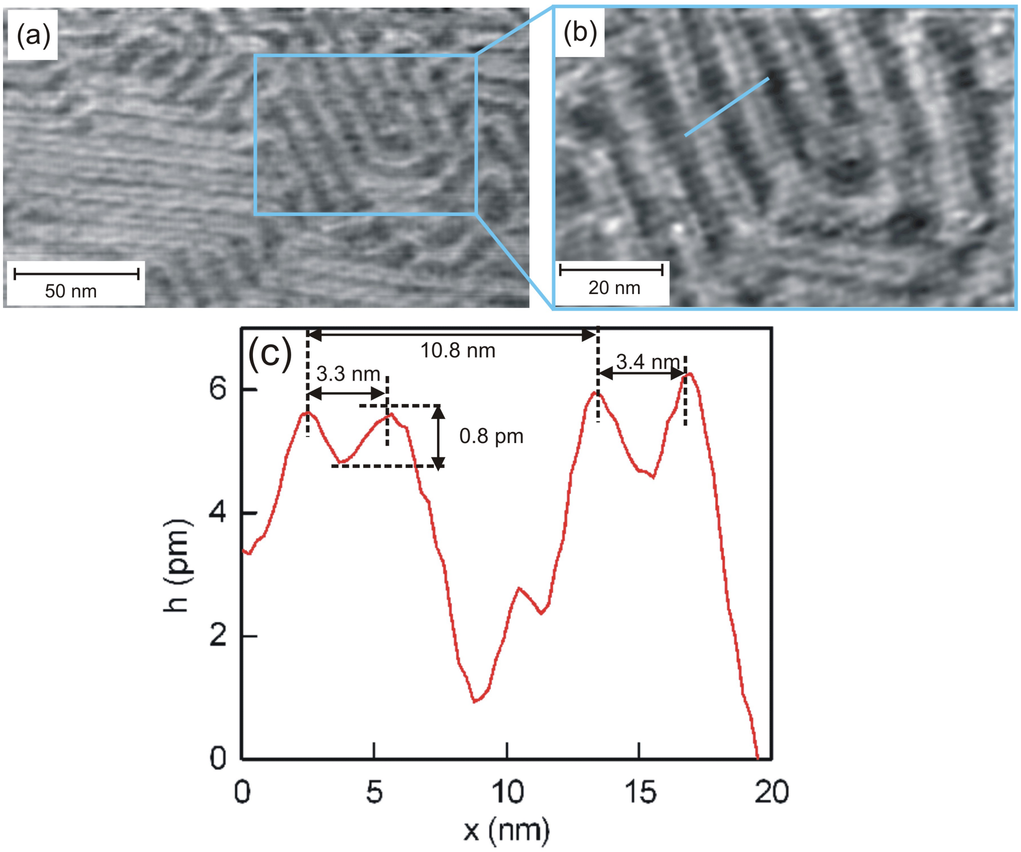

Figure 4.5: Magnification series of reconstruction lines on Au(111): (a-b) images produced by the beetle-type STM. The tunneling parameters are: I = 0.36 nA, V = 83 mV (c) line scan along the line in (b). The images are filtered by a 3 pixel Gaussian smooth.

An imperfect arrangement of reconstruction lines are shown in Fig. 4.5a. The paired ridges are clearly distinguishable at all magnifications. As a result of the imperfect arrangement of the reconstruction lines, the distance between the two ridges is 10.8 nm instead of 6.2 nm. The closest distance between the two ridges is (3.37±0.1) nm. Thus, the current lateral resolution of our STM is at least this value.

4.4 Further Specifications and Future Improvements

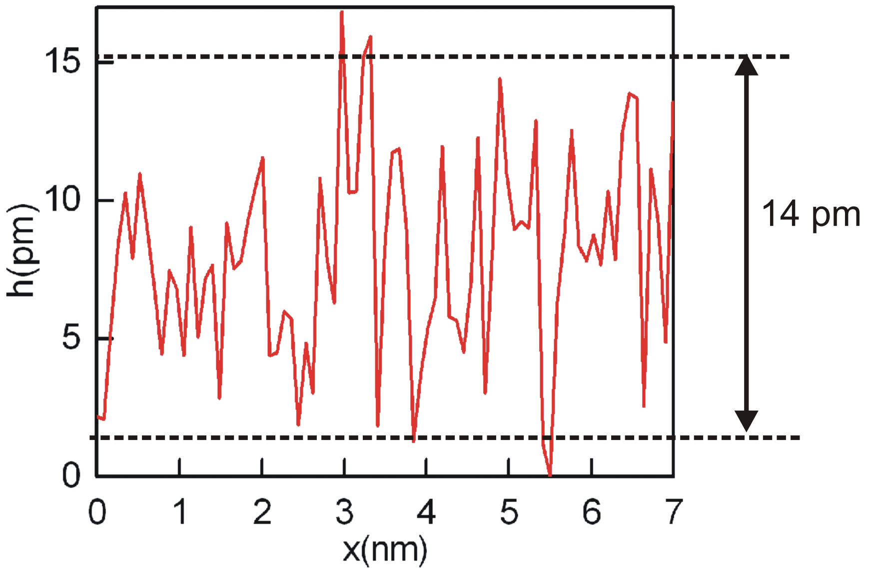

Figure 4.6: Line scan in parallel to reconstruction lines.

The line scan between the ridges in Fig. 4.6 demonstrates the current noise level of the multi-scale STM to be below 14 pm. Currently, the major noise source is a 50 Hz noise, which will be worked on in future by modifying the grounding of the system.

The z-direction of both stages of the multi-scale STM is calibrated at an Au (111) step edge. The calibration constants for the beetle-type and the XYZ-scanning stage-based STM are 6.6 nm/V and 1.2 μm/V, respectively.

A general drawback of STMs operating at ambient temperature is a relatively large thermal drift already caused by the temperature variation in the lab. The thermal drift of the multi-scale STM is currently 12 nm/h in the x-direction, 22 nm/h in the y-direction, and 2 nm/h in the z-direction. This will be improved upon in future after a careful analysis of the temperature variations on different parts of the STM.

A resonance frequency test (made by a frequency generator and a speaker) revealed the resonance frequencies of 1540 Hz, 1670 Hz, and 1890 Hz. The noise level during the measurements was 20 mV and the amplitude of the resonance peaks were around 600 mV. These comparably large frequencies are achieved by optimizing the weight of the ramp: the lighter the ramp, the higher the resonance frequencies. A minimum weight, however, is required for a reproducible slip-stick motion. The optimal weight is 13 g.

Chapter 5

A Combined Geometrical and Electronic Structure Study on GaN Micro-pillars

The III-V compound GaN, with its broad optical emission bands in the visible spectrum, is a base material for the fabrication of optoelectronic devices. GaN has therefore been extensively studied in recent years.

GaN is intrinsically n-doped as a result of intrinsic defects, most likely the nitrogen vacancies or gallium interstitials [40]. Until 1989, GaN could only be doped n-type. Following the first p-doping–achieved by Amano et al. using low-energy electron beam irradiation (LEEBI) [17] and utilizing low-temperature deposited buffer layer technology to enhance the crystalline quality [41]–high performance blue light emitting diodes (LEDs) [17] and long-lifetime blue laser-diodes [42] were built. In 1992, Nakamura et al. developed the p-doping of GaN by using the hole compensation mechanism [43, 44]. In 1993, Nakamura et al. [18] produced the first violet light GaN-LED, with wavelengths between 411 and 420 nm and an efficiency of 0.18 %. Now GaN-based LEDs cover the entire color spectrum, ranging from IR to UV regions, and can be readily manufactured by mixing GaN with Indium (In) as well as with aluminium (Al), forming InGaN and AlGaN, respectively. The mixture varies the band gap of GaN [45], resulting in a wide-range spectrum. InGaN produces longer wavelengths, while AlGaN produces shorter wavelengths than pure GaN. This observation led to the invention of semiconductor heterostructures. The InGaN/GaN-based quantum well heterostructures are used to produce blue/green light-emitting diodes (LEDS) with high-brightness properties [19, 20] as well as laser-diodes [18]. Higher efficiency (6.3 %) green and yellow light InGaN-LEDs were fabricated in 1995 [21, 22]. The first electrically pulsed GaN laser with one second long lifetime was produced in 1996 [23, 24]. In 1997, this lifetime was increasingly extended from 300 hours to 1150 hours and eventually up to 10,000 hours [46, 47, 48]. An example of a commercial application of this technology is Blu-ray Discs, which are read by GaN-based violet laser diodes.

Beyond the GaN-based thin film planar heterostructures, GaN-based micro-pillars with their unique physical properties are attracting attention in the field of optoelectronic devices. Some major advantages of micro-pillars over planar structures are that they have low defect concentrations independent of the substrate material, that they are free standing and that there is no thermal expansion mismatch between the substrate leading to a strain in the LEDs [25]. With these advantages emerges the possibility to push the efficiency of micro-scale devices to higher limits. The controlled fabrication of the micro-pillars, however, is highly challenging. The aspect ratio, the etch profile, the underetching effects, the terminating layer and the band gap character are all important factors for the fabrication of micro-pillars. With increasing information on these issues it becomes possible to control and improve the fabrication of the micro-pillars. There have been different techniques used for this purpose, i.e. SEM, AFM. In this study, the micro-pillars are investigated using the multi-scale STM, allowing for the resolution of the issues mentioned above.

In this chapter, I give a brief explanation about the crystal structure and the growth mechanism of GaN (see section 5.1). In the second section, the fabrication of the micro-pillars by means of deep dry etching is explained (see section 5.2).

Because GaN oxidizes very quickly, it is crucial to anneal the sample under UHV conditions in order to remove the oxide layer and the impurities. The oxidation character and the comparison with respect to GaAs is made in section 5.3. In the fourth section, the morphology of the micro-pillars is studied in detail. The roughness analysis of the sample–which plays an important role for electronic devices–the aspect ratio, and the etching profile of the pillars are determined. The underetching effect as a reasons of formation of four different types of micro-pillars is explained.

The preferential etching plane of the pillars is obtained after defining the orientation of the a- and m-planes of GaN by means of X-ray diffraction measurements (see section 5.4).

In the last section, local scanning tunneling spectroscopy (STS) is used to determine the doping type, the oxidation and metallization levels, the terminating layer, and the band gap character of the surface of individual micro-pillars. The possible reasons for the inhomogeneous distribution of the band gap widths on the surfaces of individual pillars are also explained.

5.1 Crystal Structure and Growth of GaN

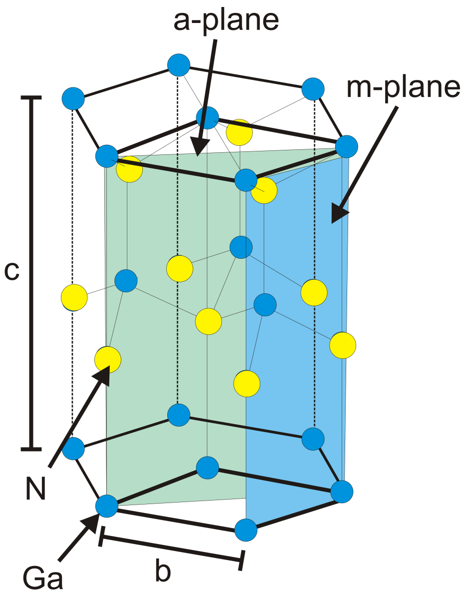

Figure 5.1: Ball-and-stick model of GaN. a-plane: ($\bar{2}110$), m-plane: ($1\bar{1}00$). The c-plane is (0001)

Gallium nitride (GaN) is a III/V direct band-gap semiconductor with a hexagonal wurtzite crystal structure. It belongs to the space group C_{6v}^{4} [49, 50]. The lattice constants at 294 K are b=0.3186 nm and c=0.5186 nm [51]. The indices of refraction at 300 K of GaN are 2.67 (λ = 367 nm) and 2.33 (λ = 1240 nm) [52]. The compound is a very hard material with a thermal conductivity of 1.3 W/cmK [53]. With the band-gap of 3.4 eV, GaN is one of the best candidates for optoelectronic devices in the green, blue, and near-UV regions [54, 55].

At the beginning of the last century, the growth of GaN was made possible using the cooling melt procedure due to its high vapor pressure. This process requires very high temperatures of around 2200^{o} and pressures of around 6 GPa [56, 57]. The growth of GaN is at present achieved by utilizing different epitaxial methods such as hybrid vapor phase epitaxy (HVPE)[58, 59, 60, 61], molecular beam epitaxy (MBE) [62, 63, 64, 65], and metalorganic vapor phase epitaxy (MOVPE) [66, 67, 68].

The n- or p-type doping of GaN is mostly done by using silicon (Si) [69] and magnesium (Mg) [17], respectively. The dopants change the growth behaviour of GaN, causing tensile stress and making the compound brittle. The compound has a very high spatial defect density in the range of 10^8 to $10^{10}/cm^2$ [70]. On the other hand, it has a mean diffusion length of only 250 nm for charge carriers before recombination to produce a photon [71]. GaN can also emit light at defect densities near $10^{10}/cm^2$ [72]. In contrast, materials with higher diffusion lengths of 1-7 μm–such as GaP-LEDs [73, 74, 75, 76, 77] or GaAs LEDs [78, 79]–require a much lower defect density, usually less than 2-5$\cdot$ $10^4/cm^2$ to avoid excessive non-radiative recombination at the defects [80, 81] e.g. for GaP [73].

5.2 Fabrication of the GaN-based Micro-pillars

To date, the fabrication of nano-structures has been done using various strategies, such as top-down or bottom-up approaches. The growth of nano-structures in the bottom-up approach is mostly done by molecular-beam-epitaxy (MBE) [62, 63, 64, 65], hybrid vapour phase epitaxy (HVPE) or by metalorganic vapour phase epitaxy (MOVPE) [58, 59, 60, 66, 67, 61, 68]. On pre-structured templates, deep dry-etching is used to fabricate nano-structures using the top-down approach [36]. It is also possible to combine top-down and bottom-up approaches to grow heterostructures of InGaN/GaN layers with MOVPE on free standing dry-etched silicon pillars [82].

3D nano-structures are attracting attention due to their large effective areas and small defect levels. In a 3D nanoLED the thermal expansion mismatch between the substrate and the LED layers do not cause excessive strain [25], whereas the mismatch between a planar GaN layer and a sapphire substrate is around 17 %. Another interesting approach concerning 3D nano-structures is to increase the active LED area by core-shell strategies approach [25]. In the core-shell approach, a nano-pillar is formed of an inner core and an outer shell. The inner core and the outer shell are differently doped with respect to one another. This combination builds a solid state light source with an increased volume of the active area.

In this section, the GaN-based heterostructure sample investigated by the multi-scale STM is defined and the etching process used to create micro-pillars on the GaN-based sample will also be explained.

The micro-pillars are fabricated by Prof. Waag's group at the Technical University of Braunschweig. The two-inch wafer substrate was purchased from the *OSRAM* company.

The GaN micro-structures are cryogenically deep dry-etched pillars in GaN/InGaN heterostructures using an inductively coupled plasma (ICP).

5.2.1 GaN-based Substrate

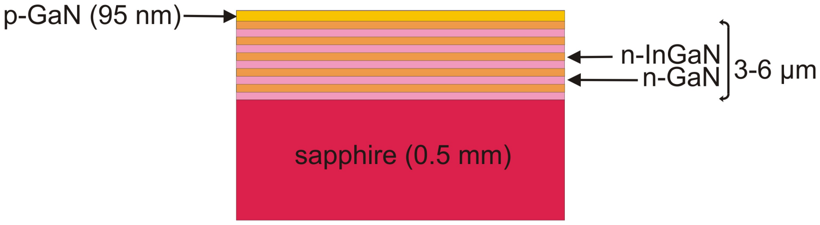

Figure 5.2: Sketch of a side view of the GaN-based sample. The InGaN/GaN quantum well and barrier sequence are grown on a sapphire substrate. The capping layer is formed from p-doped GaN.

Fig. 5.2 schematically demonstrates the sample that is to be processed by deep dry-etching. The layer sequence starts with an n-doped GaN-buffer layer grown on a 0.5 mm thick sapphire substrate in the (0001) direction. This is followed by a five-fold sequence of n-doped InGaN quantum wells (QW) separated by n-doped GaN quantum barriers (QB). This so-called LED active region is 3-6 μm thick. The heterostructure is covered with a 95 nm thick p-doped capping layer made of GaN, which is characterized in section 5.5. The MOVPE-precursors for the QW and the QB growth are triethylgallium (TEGa) and trimethylindium (TMIn). The thickness of the QW and the QB are 6 nm and 14 nm, respectively. Those LED active regions–InGaN quantum wells–were probed by the STS using multi-scale STM (see section 5.5.1).

5.2.2 Forming of Micro-pillars by Deep Dry-etching

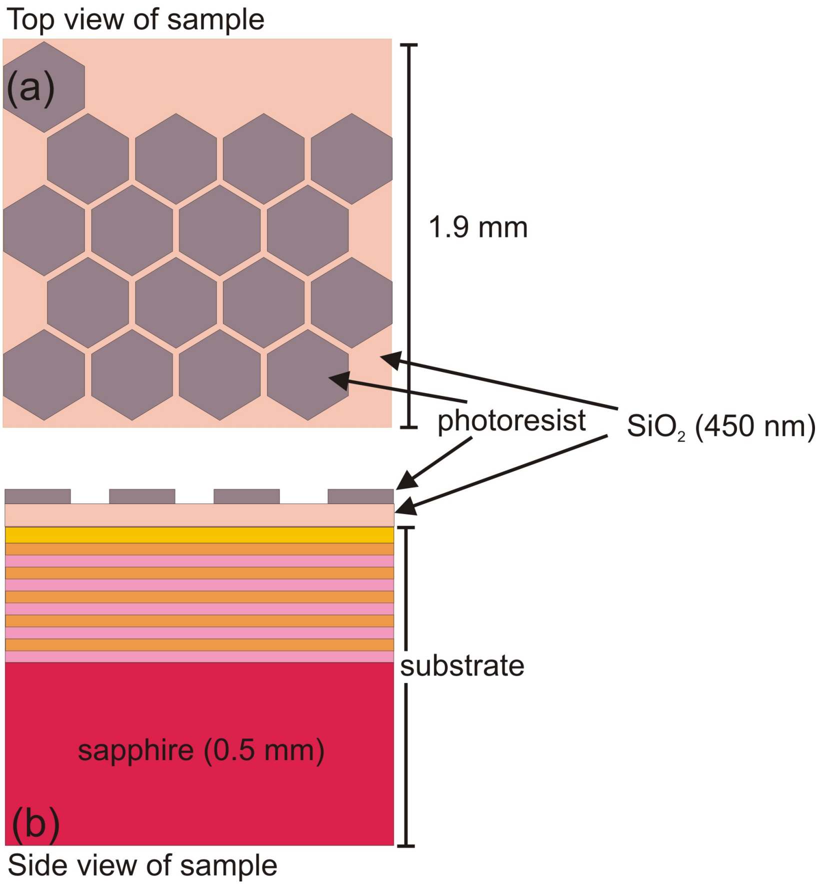

Figure 5.3: Sketch of the etching setup: (a) top view of GaN-based sample showing the mask and the SiO_2 layer just before etching (b) side view of GaN-based sample demonstrating the layers of the sample, also just before etching.

The etching set-up of the pillars is shown schematically in Fig. 5.3. The honeycomb form of the mask with a SiO_2 capping layer is sketched in Fig. 5.3a. The layer sequences of the GaN-based sample just before etching are shown in Fig. 5.3b.

The etching process begins by covering the GaN-based sample with a 450 nm thick $\mathrm{SiO_2}$ layer to increase the selectivity between the GaN and the photoresist mask during etching. A honeycomb mask is fixed above the sample. Photolithography is then used to imprint the mask pattern on the sample. In this case, the regions defined by the hexagons are hardened by light. The regions between the hexagons are softer and exposed to etching. A Sentech SI500C

(*Sentech Instruments*) dry-etching system performs the dry etching at a power of 500 W with a bias voltage of -12 V, a temperature of -95^0, and with an etch rate of 2.8-4.0 μm/min. The plasma gases utilized for the etching of GaN are CH_4, H_2, and Ar. This process results in μm diameter pillars in submicron lengths. The CH_4 gas leads to preferential desorption of Ga as Ga_4C_3 after the reaction, while H_2 gas leads to preferential desorption of N as NH_2. After completing the dry etching process, the sample is dipped into an HF solution to remove the remaining oxide layer and the photoresist mask.

The success of the etching process is dependent on the aspect ratios of the pillars fabricated and on the smoothness of the surface. The flow rate of the etch gases, the ion energy, and the ion density used are important parameters that determine a successful etching process. High etch rates achieved by increasing the ion energies and ion densities result in pillars with high aspect ratios. However, high etch rates also cause underetching effects, leading to unstable pillars. Ideally, the etched pillars should have their shape defined by the mask; unfortunately, however, high etching rates cause further etching of the pillars towards their centers, which in turn causes a geometric deformation. This drawback is defined as underetching. It is important to choose the etch parameters so suitable to get biggest aspect ratios with lowest underetching effects. This would lead to fabricate the best micro-structures available for optoelectronic devices.

Following the micro-pillars' fabrication, the aspect ratio, the etch profile, the underetching effects, and the terminating layer are studied in order to gain a better understanding of the fabrication process. The multi-scale STM is used to examine these issues, which could then be in turn used to improve the fabrication process.

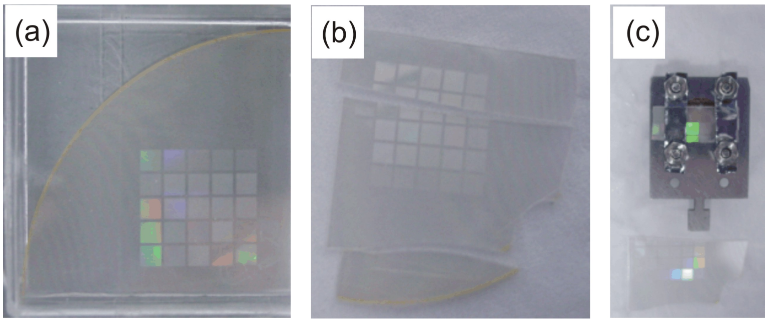

Figure 5.4: The sample containing micro-pillars: (a) entire wafer (b) after cutting (c) mounting setup.

In Fig. 5.4a, the wafer already containing the micro-pillars is shown. As each square contains pillars of different sizes and with different spacing, they have different optical colors. In order to fix the wafer to the sample holder, it is cut into suitable sized pieces using a diamond cutter (see Fig. 5.4b). It is then attached to the sample holder with the help of two tantalum foils in order to provide the electrical contacts necessary for STM measurements, as shown in Fig. 5.4c. Within this work, four different squares consisting of different types of micro-pillars are presented.

5.3 Major Contaminates and Cleaning of GaN-based Sample under UHV-conditions

The fabrication of GaN-based samples is done in different environments. Surface contamination is unavoidable during sample transfer. These contaminants require proper cleaning processes.

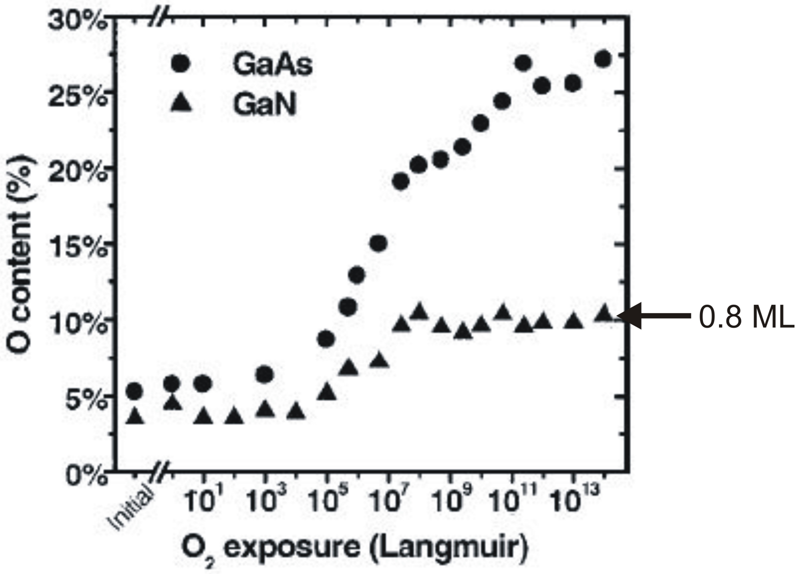

Figure 5.5: Oxygen content at GaN and GaAs surfaces after exposure to oxygen gas taken from [83].

The oxidation of GaN in air occurs in milliseconds. However, oxidation stops on GaN after the formation of only a single monolayer of oxide on GaN [83]. Fig. 5.5 shows the oxidation behaviour of GaN compared to GaAs after exposure to oxygen gas under UHV conditions. No increase in the oxygen content below 10^5 Langmuir (L=10^{-6} Torrs) for either GaN or GaAs is observed. Above 10^5L, however, the oxygen content begins to increase. For GaN, the oxygen content continues to increase until it stabilizes at 10% after an exposure of 10^8L. For GaAs, however, the oxidation continues indefinitely. The possible bonding sites for oxygen on GaN are either nitrogen vacancies or gallium atoms. The oxidation stops after the saturation of all available bonding sites on the surface. Adsorption of oxygen onto GaN surfaces is an exothermic process for up to 0.8 monolayers [84]. Above this, coverage the adsorption reaction is endothermic. Several surface cleaning procedures to remove oxygen from the GaN surface were studied. Some of those procedures are: ex-situ chemical etching [85][86], nitrogen sputtering [87], annealing in ammonia [88, 89], Ga deposition, redesorption, and N-plasma assisted cleaning [90].

The most effective cleaning technique to remove oxygen is reported to be Ga deposition/redesorption. For this technique, the Ga atoms deposited onto the surface of a GaN sample bind to oxygen atoms on the surface. By redesorption of Ga atoms from the surface, the oxygen atoms bound to desorbing Ga atoms are removed. However, XPS studies on a GaN surface cleaned by Ga deposition/redesoprtion show that the GaN surface terminates with Ga-rich (metallic) regions [90].

STM and STS studies require a high level of cleanliness due to the sensitivity of the surface structure, the electronic properties, and the possible reactivity of semiconductors to contaminants [91]. In the present setup, it is only possible to use the thermal annealing method as a cleaning procedure.

The GaN-based sample was annealed after its transfer into the UHV chamber by keeping it in thermal contact with a Cu plate exposed to electron bombardment. The annealing is achieved at $I_{filament} = 2.5A$, $I_{emmision} = 12.5mA$, $V_{high} = 1kV$ for 5 h by keeping it at 828 K with a base pressure of 4x10^{-10} mbar.

5.4 Morphology of the GaN-based Micro-pillar

In this section, a roughness analysis of the sample is obtained on an overview image of 173 μm x 173 μm of the GaN-based sample. The etch profile of the pillars and the effects of underetching due to high etch rates are discussed.

5.4.1 Overview and Roughness Analysis of Micro-pillars

As a first step, I present an overview image of the pre-structured sample in order to gain information about the roughness and etching quality of the sample. The ability to magnify to a specific region in the overview image is also important when studying the fabricated structures. Otherwise, blind approach of the STM tip to any region on the surface might end with a region where the etching process was not successful, causing damaged micro-pillars or even no pillars.

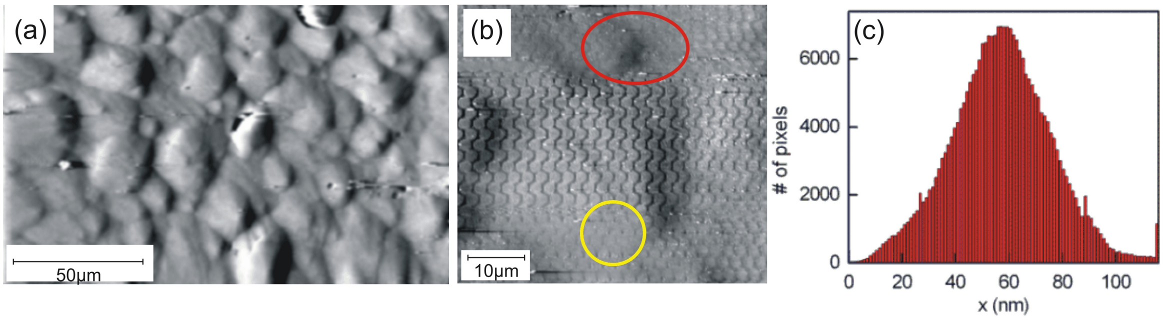

Figure 5.6: Overview image of GaN-based sample. (a) overview image with a length of 173 μm taken by multi-scale STM (XYZ-scanning stage), I = 0.15 nA, V = -3.8 V (b) magnification at a random region on the sample measured by the multi-scale STM (XYZ-scanning stage), I = 0.153 nA, V = -3.6 V. Red ellipse and yellow circle shows regions on the surface with an unsuccessful etching. (c) Height histogram of the overview image.

Fig. 5.6 shows two different STM images at different magnifications produced by multi-scale STM (XYZ-scanning stage). Fig. 5.6a is a 173 μm x 173 μm large image recorded by the XYZ-scanning stage of the multi-scale STM. The STM image illustrates a rough surface, which contains differently sized humps distributed randomly. Fig. 5.6b shows a STM image with a bigger magnification than the image in Fig. 5.6a. At this magnification, it is already possible to distinguish regions with different etching properties. The quality of the etching process differs at the center of the image from the marked regions. It is obvious that the etching grooves are oriented in one direction. This means that the etching was not homogeneous in all directions. However, the etching grooves on the red-ellipsed and yellow-circled regions are hardly visible in the STM image, showing an unsuccessful etching process. Fig. 5.6c is a height histogram of the overview image Fig. 5.6a. According to the height histogram, the sample has a height variation of 116 nm.

As demonstrated by the two different magnification series in chapter 4, two different squares of the sample are studied by the multi-scale STM. This study revealed two kinds of pillars: rod-shaped and star-shaped pillars, each with a different size. The rod-shaped micro-pillars have diameters of around 2.2 μm, a center-of-mass distance of 2.5 μm, and a height of around 400 nm. The star-shaped micro-pillars have a corner-to-corner distance of around 1.3 μm, a center-of-mass distance of 1.4 μm, and a height of around 400 nm.

The etching characteristic varies substantially for each kind of shape. The gap between the rod-shaped pillars is considerably larger in the horizontal direction than in the vertical direction. The inhomogeneous distribution of the spacing between the rod-shaped pillars is demonstrated by three line scans over three different directions (see Fig. 4.2). The star-shaped pillars show a six-fold symmetry as well as a homogeneous distribution of spacing between the pillars. These show no marked asymmetry in the etching (see Fig. 4.3).

Therefore, the etching character–and consequently the aspect ratio–of the rod-shaped pillars is different from that of the star-shaped pillars.

5.4.1.1 Discussion

The dissimilar lateral distribution between the rod-shaped and star-shaped pillars may be due to the different etch rates and different concentrations of etchants applied during the etching process. The STM images Fig. 4.2 and Fig. 4.3 give the information about the lateral distribution of the micro-pillars, which might allow for better control of the etch rates and the etchant concentrations. Though, the etch rates and the etchant concentrations are fundamental in the fabrication of pillars with high-aspect ratios. To avoid that the depletion regions dominate the electrical behaviour of the devices, the aspect ratio must be at least 2 [25].

In order to have differently-profiled sidewalls, it is possible to control the etch profile of the pillars. The diameter, the height, and the spacing between the pillars define their aspect ratio. The etch profile will be positive if the spacing between the pillars is smaller than the diameter of the pillars. The aspect ratio will then decrease if the etch rate is reduced [36]. The STM images (see Fig. 4.2 and Fig. 4.3) indicate that the pillars have a positive etch profile.

Until now, the predefined structures in μm regions have mostly been investigated by using a SEM, which gives topographical information but not a detailed roughness analysis. By using the multi-scale STM, It became possible to get a detailed roughness analysis of the overview images. This roughness analysis makes it possible to try to reduce the surface roughness caused by etching process. Overview images are also useful at choosing regions at the sample, which might be interesting to investigate.

5.4.2 Etching Characterization of GaN-based Sample

As a single type of mask is used during etching, the process must be uniform in the ICP chamber. However, differently shaped pillars are observed at different squares of the sample. This raises an issue in the etching process of the pillars. The source of the problem–the distinct shapes–may have been formed by various reasons. One of the reasons might be underetching due to high etching rates. Second reason might be the crystallographic dependent etching. The third one might be because of a failure in the formation of photoresist during the photolithography process or from a combination of all.

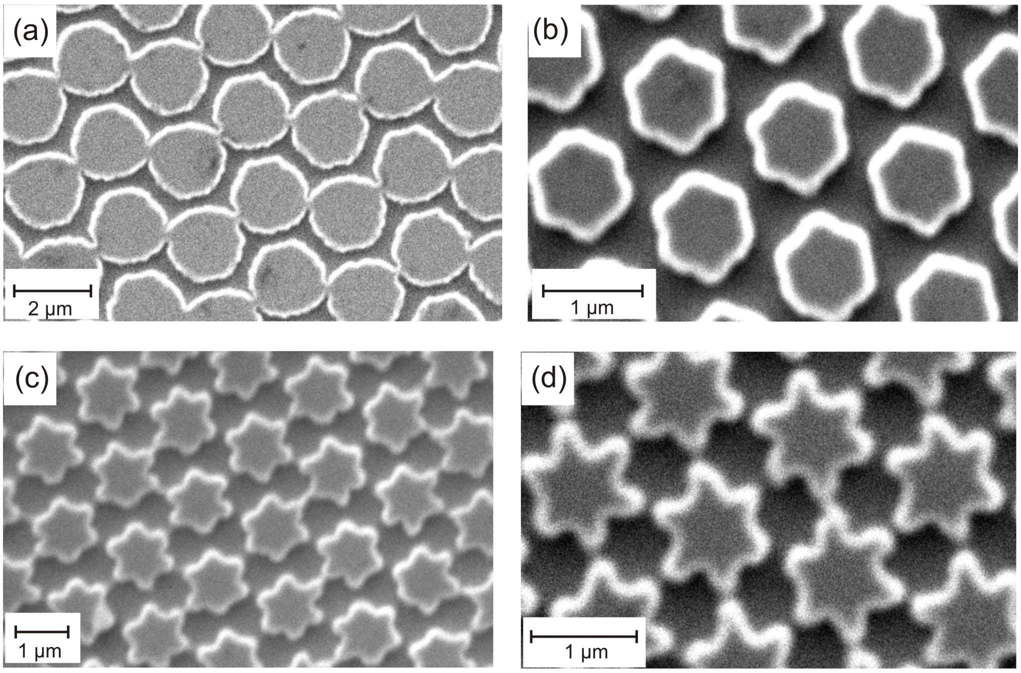

Figure 5.7: SEM images recorded at four different squares showing different degrees of underetching, (a) rod-shaped pillars with non-homogeneous spacing (b) hexagonally-shaped pillars (c) star-like pillars (d) star-shaped pillars with homogeneous spacing between them; images by L. Kühnemund.

In Fig. 5.7, SEM images of four distinct-shaped pillars at four different squares are shown. In Fig. 5.7a, rod-shaped pillars are shown with an inhomogeneous lateral distribution of the pillars. The etching took place mainly in the x-direction. In the y-direction, the pillars are not even completely separated from one other. Images of these types of pillars taken from a multi-scale STM are already presented in section 5.4.1. In Fig. 5.7b, hexagonally-shaped pillars with a homogeneous lateral distribution different from the rod-shaped pillars are demonstrated. The star-like pillars shown in Fig. 5.7c are formed by the continuous etching of the hexagonally-shaped pillars in Fig. 5.7b starting from their sides and going towards their centers. This etching continues further, forming the perfect star-shaped pillars illustrated in Fig. 5.7d. The lateral distribution for star-like and star-shaped pillars is as homogeneous as the hexagonally-shaped pillars' distribution.

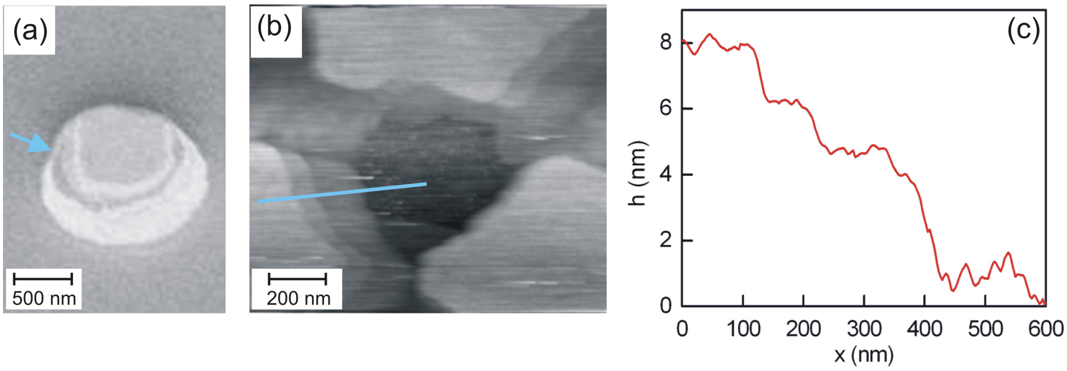

Figure 5.8: Etched edges as a result of underetching (a) SEM image showing a rod-shaped pillar with an etched edge surrounding the pillar (image taken in the group of Prof. Waag, TU Braunschweig) (b) STM image of star-shaped pillars presenting multiple etched edges surrounding the pillars in different directions, I = 0.153 nA, V = -3.8 V. It is recorded by beetle-type STM (c) line scan measured along the red line in Fig. 5.8(b).

An example of the etching characteristic is demonstrated in Fig. 5.8. Fig. 5.8a is a SEM image of a rod-shaped pillar. The pillar is not etched as a homogeneously perfect rod. Instead, an etched edge is observed at the top of the pillar marked by an arrow. The pillar has an almost conical shape with a flat top rather than a rod-shape. Fig. 5.8b illustrates a STM image produced by the beetle-type STM demonstrating sections of three star-shaped pillars. There, several etched edges surrounding the pillars in different directions with different terrace sizes are observed. This could be a tip effect. However, another possible explanation is based on a line scan (see Fig. 5.8c) measured along the line in Fig. 5.8b. According to the line scan, the terraces are several hundred nm large. The edges have a height of 2 to 4 nm, which is comparable to 2 to 4 bi-layers of GaN. These etched edges may have arisen from an underetching process, which supports the preferential etching character.

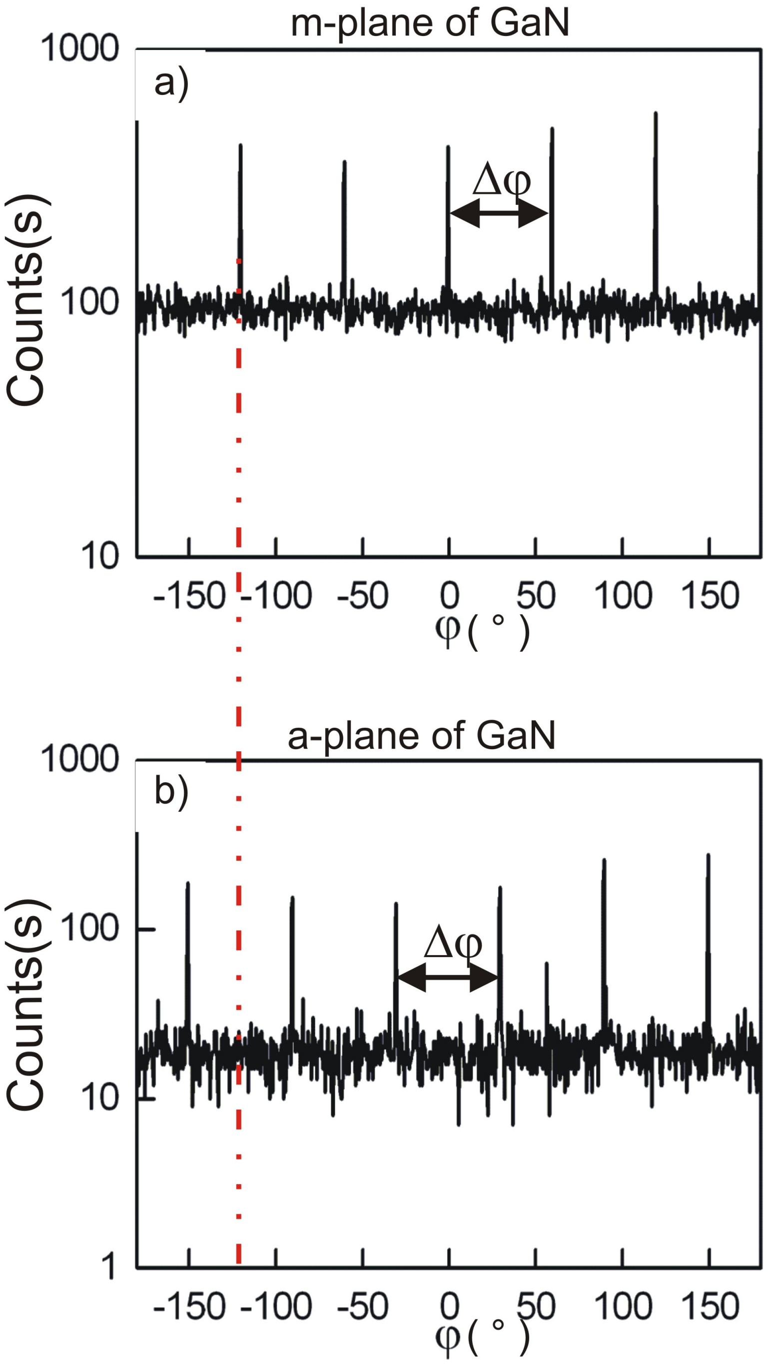

Figure 5.9: XRD measurements to define the m- and a-planes of GaN. (a) φ-scan for the $(1\bar{1}00)$-plane (b) φ-scan for $(\bar{2}110)$-plane, incidence angle 1^o. The dashed line shows an offset of 30^o between the two planes.

X-ray diffraction experiments were made in order to understand the etching characteristics of the pillars, and carried out by determining the orientation of the m- and a-planes as well as the unit cell of the GaN-based pillars. The XRD data in Fig. 5.9 shows the orientation of the GaN's m- and a-planes, respectively. The m- and a-planes exhibit hexagonal symmetry and an offset of 30^o with respect to one another. The dashed line in Fig. 5.9 shows this offset between the two planes. The orientation of the m- and a-planes and of the GaN unit cell can thus be defined.

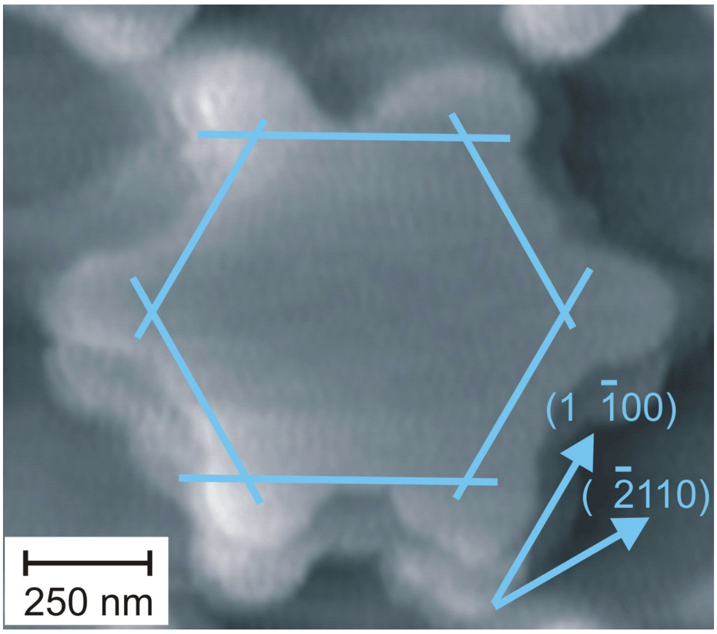

Figure 5.10: STM image of a star-shaped pillar (measured using the beetle-type STM), I = 0.153 nA, V = -3.8 V. The two arrows show the directions of the m- and a-planes. The lines are drawn in the direction of the a-planes.

The information obtained from the XRD measurements, combined with the images recorded by the multi-scale STM based in the known scan direction, reveal the orientation of the hexagonal unit cell of GaN at a pillar. In Fig. 5.10, the direction of the m- and a-planes at a star-shaped pillar is demonstrated. The lines drawn demonstrate the direction of the GaN's a-planes. The continued etching of the pillars towards their centers is observed to be in the direction of the a-planes (preferential etching).

5.4.2.1 Discussion

The formation of several types of pillars shows that the ICP etching was not homogeneous for this GaN-based sample. The reason for the differently-shaped pillars may be the underetching caused by high etching rates. The new shapes are formed by preferential etching of the GaN's a-planes. As shown in Fig. 5.10, the star-shaped pillar is formed by the continued etching of the pillar towards its center along the a-planes. The closely packed m-plane, with high atom densities, is more inert than the a-plane with a lower atom density. This causes a preferential etching along the a-plane. This crystallographic dependent etching (the $(\bar{2}110)$-direction is etching faster than the $(1\bar{1}00)$-direction) is already known for Si [92] but has not been reported for GaN so far. On the other hand, the variation in the lateral distribution characteristic of different pillars may have arisen from the formation of the photoresist during the photolithography. As a result, low-aspect ratio rod-shaped pillars with positive etch profiles are formed (see Fig. 4.2). This is due to inhomogeneous ICP conditions.

The underetching, crystallographic dependent etching, and the formation of the photoresist are processes that determine the shapes and aspect ratios of the pillars. Fabrication of high-aspect ratio, stable, functional micro-structures is possible by reducing the underetching, determining the crystallographic dependent etching, and controlling the formation of the photoresist during the photolithography.

5.5 Determination of the Electronic Properties of the GaN-based Micro-pillars by STS

Understanding the electronic properties of the GaN-based micro-pillars' and nanostructures' surfaces are crucial in order to determine the band gap energy width of those structures. The GaN heterostructures–formed by different atoms, such as In or Al–as well as impurities in GaN or in the oxide layers on the surface of those structures, cause changes at the band gap energy. The STS is a powerful tool that can characterize the electronic properties of surface of semiconductor materials such as GaN. With the STS, it is possible to get information about the band gap energy widths, the terminating layer, the doping type, the oxidation, and the metallization levels of the micro- and nanostructures.

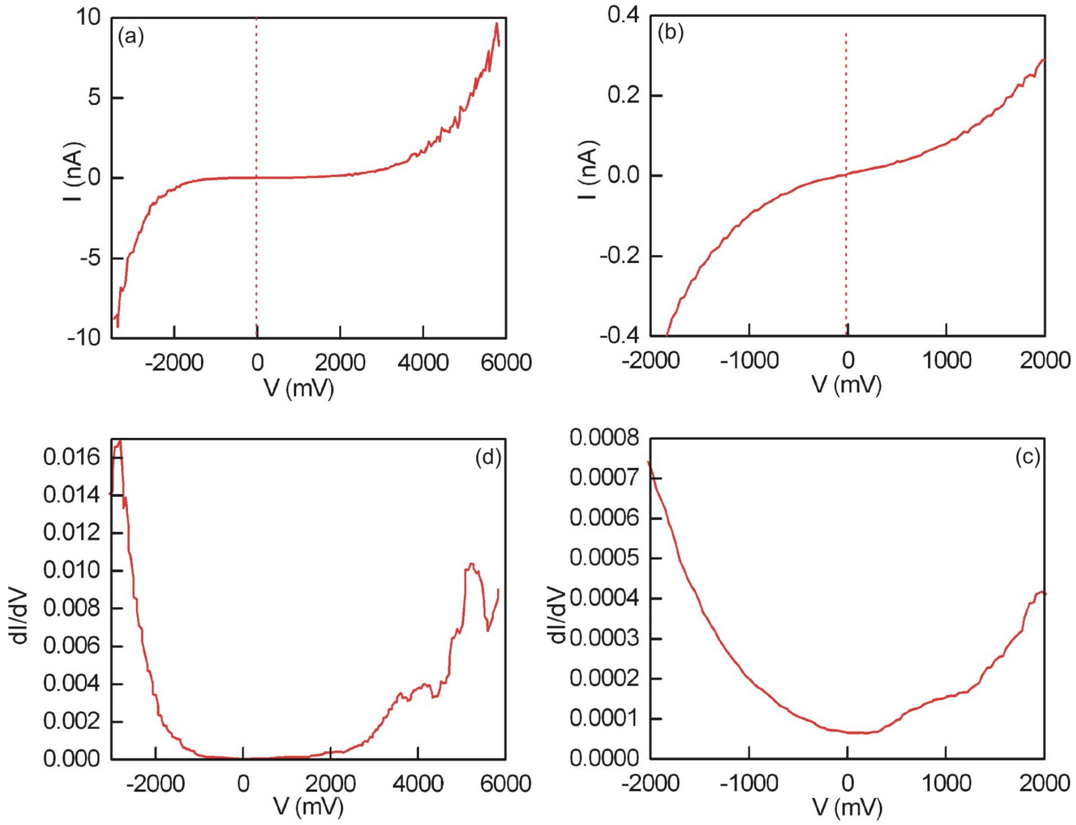

Figure 5.11: Examples of STS data: (a) semi-conducting I(V) characteristics, (b) metallic I(V) characteristics, (c) numerically derived and smoothed dI/dV(V) characteristics of (b), (d) numerically derived and smoothed dI/dV(V) characteristics of (a).

The multi-scale STM is used to locally measure I(V)-curves on individual pillars' surfaces. Fig. 5.11 shows typical I(V)-curves (see Fig. 5.11a-b) measured on a star-shaped pillar and their numerically-derived dI/dV(V)-curves (see Fig. 5.11c-d). Fig. 5.11a exhibits typical semi-conducting behaviour. The Fermi level is closer to the conduction band (CB) than to the valence band (VB). Thus, the surfaces of the pillars are p-doped. In Fig. 5.11b, the I(V)-curve shows typical metallic behaviour, where the slope is not zero at 0 V. The difference between semi-conducting and metallic I(V) characteristics is more obvious in Fig. 5.11c-d. The dI/dV(V)-curve in Fig. 5.11c has a parabolic shape and exhibits zero band gap width, which is typical for a metal surface. On the other hand, the dI/dV(V)-curve in Fig. 5.11d shows a band gap, where the conductance value is zero at distinct voltage values.

In this section, the distribution of the GaN-based pillars' band gap energy is studied. The band gap energy of each area locally probed by STS can be obtained from the differential conductance vs. bias voltage. Within this work after having recorded a suitable STM image, it was only possible to record I(V)-curves by placing the tip on a chosen point on the surface and ramping the voltage with the feedback loop switched off. Additional STM images were taken in between to determine tip changes and to calculate the drift properly. The drift was found to be 20 nm/h in x- and 12 nm/h in y-direction in all images. During the data processing the drift was assumed to be linear and eliminated from the data points. The dI/dV(V)-curves are determined by numerically taking the first derivative of the I(V)-curves. The analysis of the STS data yields the criterion of the surface region of interest's homogeneity in terms of the electronic properties. The band gap energies of the micro-pillars are mapped out laterally, and the data are then summarized in a histogram to obtain the interval of the band-gap energies over the surface.

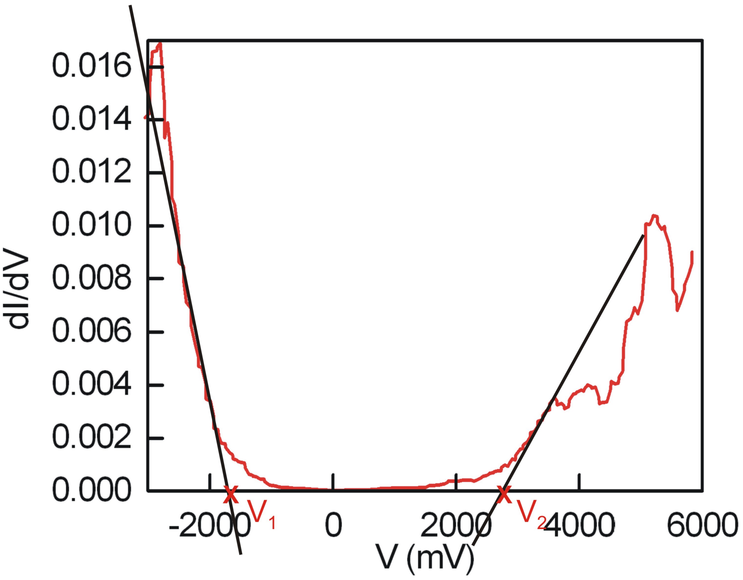

Figure 5.12: The band gap ist measured from the dI/dV(V) curves by taking the difference of the intersection points of the tangent lines on the V axis.

As shown in Fig. 5.12 The band gap energies are determined from the numerically calculated normalized first derivative (dI(V)/dV)/(I(V)/V)-curves. Two tangent lines are drawn to the ascending and descending part of the dI/dV(V)-curve. The difference between the two intersection points of the tangent lines on the bias voltage axis is taken as the band gap energy.

5.5.1 Surface Structure of the Micro-pillars

The STS technique is used to determine the electronic characteristic of the surfaces of individual micro-pillars. Four different regions of the GaN-based sample with several pillars have been studied.

Individual pillars are characterized according to their band gap energy maps. Examples of some features on the surface of several individual pillars are given on four different maps. The first map shows that the surfaces of three individual micro-pillars are made of Ga, GaN, and oxide sections. The second map presents an inhomogeneous distribution of Ga, GaN, InGaN, and oxide regions on a single micro-pillar. The third map is also an example of a single micro-pillar, illustrating mostly GaN characteristics, partly Ga, and InGaN characteristics arising from the inhomogeneous etching process. The final example is a map of a micro-pillar measured after sputtering the sample to remove the residual oxide seen on the entire maps. As a result of the sputtering, the surface of the pillar shows Ga characteristics. For each map, a histogram showing the interval of the band-gap energies over the surface is presented.

The color codes used for the band-gap energy maps are as follows:

Color code	**Energy**	**Character**
Dark blue	0 meV	metallic, Ga-rich region
Red	0 meV - 1500 meV	gap region, not found on the surface
Yellow	1500 meV - 2300 meV	GaN with deep-level impurities
Light Green	2300 meV - 2900 meV	InGaN QW
Dark Green	2900 meV - 3400 meV	doped GaN
Light blue	> 3400 meV	oxidized GaN

Table 5.1: Color codes of the band gap energy maps

In the following maps, the band gap energies of different pillars are presented and discussed.

5.5.1.1 Band Gap Energy Map of Ga, GaN and Oxide

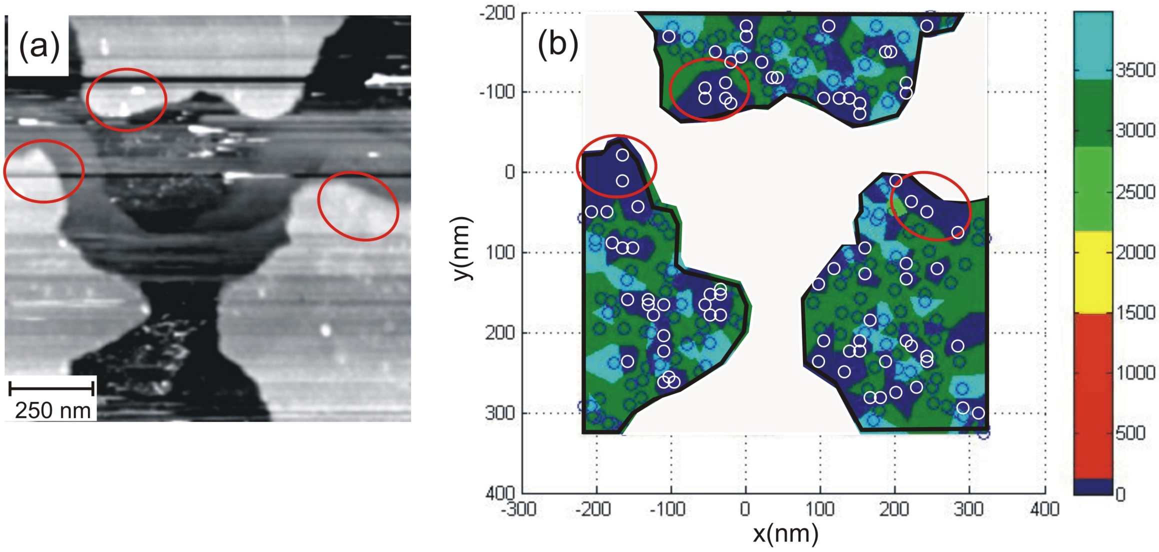

Figure 5.13: Band gap energy map: (a) STM image (using beetle-type STM) of sections of three differently star-shaped pillars, I = 0.153 nA, V = -2.2 V. (b) Band gap map of Ga, GaN, and oxide created by STS data measured on the sections of three star-shaped pillars. The red ellipses correspond to one another at the STM image and at the map.

The STM image in Fig. 5.13a shows partial areas from three star-shaped nanopillars with some bright spots slightly distributed over the surface. Some of those bright spots are marked by red ellipses and might refer to either Ga droplets or oxide layers which cannot be clearly defined from the STM image. The region neighboring the micro-pillars exhibits areas with some non-uniform etching, which may be attributed to the underetching problem as discussed in section 5.4.2. Fig. 5.13b shows the band-gap energy map of the micro-pillars in Fig. 5.13a. Each point refers to a local spectroscopy recorded on the surface of the pillars. The regions with different band-gap energies are shown by six different colors (see table 5.1). The contours of the star-shaped pillars were drawn to aid with visualisation. The band gap energies are calculated from the first derivative of the I-V curves. These values are then mapped spatially as a Voronoi diagram. Since the STM tip cannot reach the bottom of the region

between the micro-pillars, there are no STS data shown for this region.
The band-gap energy map shows similar band gap energies grouped together in distinct regions. In the areas with bright spots labeled by red ellipses in Fig. 5.13b the surface is metallic. The metallic property of the protrusions monitored from the energy map suggests that these areas are composed of Ga rich components rather than of leftover oxides of the surface. On many of the surfaces of the micro-pillars, semiconducting characteristics with a finite (certain) band gap energy is exhibited. The band-gap energy map also illustrates some oxide regions on the surfaces of the pillars.

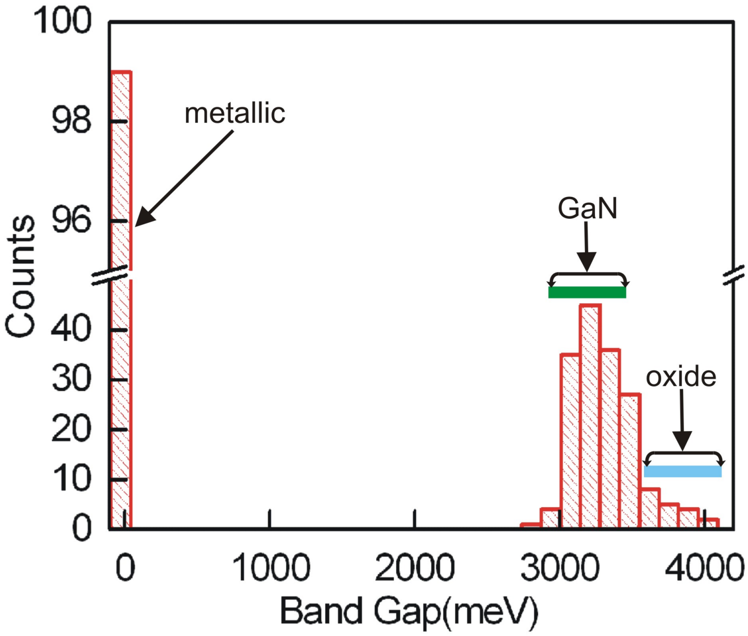

Figure 5.14: Histogram of band gap energies of pillars in Fig. 5.13.

Fig. 5.14 shows the histogram of the measured band gap energies of the pillars in Fig. 5.13. There are three characteristic intervals: the first one at 0 eV corresponds to Ga (metallic) regions of the pillars; the second one, around 3.4 eV, lies at the band gap of GaN; and the third one, above 3.4 eV, shows some oxide layer also seen at the histogram.

5.5.1.2 Discussion

The Ga-rich regions on the surface of the pillars might be caused by different processes. One of them is the cleaning process of the GaN surfaces by the manufacturer, which might involve the Ga deposition/redesorption method [90]. By this method, the removal of the oxide layers from the GaN surface (See section 5.3) may result in Ga-rich regions on the surface arising from the Ga deposition. Another reason may be the Ga accumulation and N depletion during etching in $CH_4/H_2/Ar$-plasma. In the literature, examples of the effects of etchant concentration on the surface of the pillars have been reported, such as the increase of Zn on the surface region after etching ZnO substrates with $CH_4/H_2/Ar$ [93]. This results in the roughening of the surface due to the formation of bright spot features. The same phenomena has also been observed by etching different multi-component materials such as InP and (Ba,Sr)TiO_3 in $CH_4/H_2/Ar$ and Ar/Cl_2 plasmas, respectively [94, 95, 96]. These features can be attributed to the preferential desorption of one of the reaction products. The Ga accumulation and N depletion during etching in $CH_4/H_2/Ar$ plasmas can be investigated by the STS, which is referred to as the metallization of the sample. The preferential desorption of N results in NH_3 while the preferential desorption of Ga yields Ga_4C_3. It is also shown in section 5.5.1.7 that Ar remove N atoms easier from the surface than the Ga atoms. The excess Ga on the surface perfectly wets a Ga-polar GaN surface resulting in a dynamic, fluidlike bilayer [97, 98]. XPS measurements also have revealed the metallicity of a GaN surface, when 1.5 ML of Ga have been evaporated on it, while with only 0.5 ML Ga, the surface remains semiconducting [99]. The etchants did then remove enough nitrogen atoms to have an excess of Ga of well above 0.5 ML. If some parts on the surface are Ga-polar, the Ga can flow and wet the surface. This can explain the Ga rich regions not only at the corners but also at the interior parts of the pillars. This has been demonstrated here by the STS and also by the bright spot features shown on images made by the multi-scale STM.

The oxide layer measured by the STS might also originate from two different processes. The residual SiO_2 capping layer used for dry etching as explained in section 5.2.2 may be one of the reasons for the oxide on the surface. The second reason is that the transfer of the sample in air must have caused an oxidation due to the speedy oxidization of GaN [90]. From this, one can conclude that the annealing process (5.3) used for the sample cleaning was not sufficient to remove all the oxide from the surface.

5.5.1.3 Band Gap Energy Map of Ga, InGaN, GaN, Impurities, and Oxide

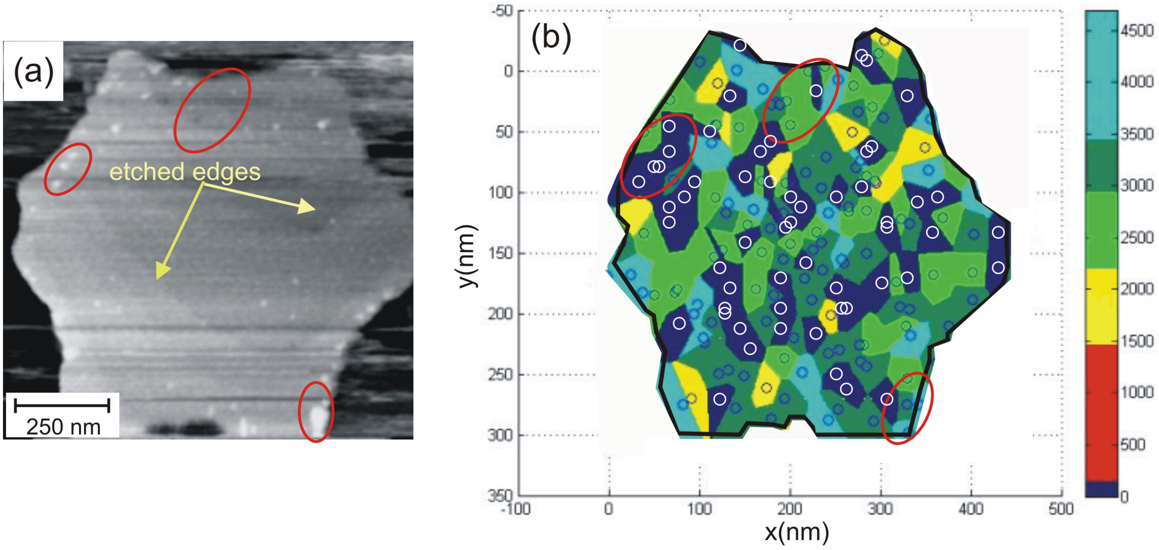

Figure 5.15: Band gap energy map: (a) STM image (usnig beetle-type STM) of a star-shaped pillar, I = 0.164 nA, V = -5 V. (b) Band gap map of Ga, GaN, InGaN, impurities, and Oxide created by STS data measured on the star-shaped pillar. The red ellipses at the top, at the bottom and at the left corner correspond to one another at the STM image and at the map. The arrows mark the etched edges arising from preferential etching.

Fig. 5.15a shows a STM image of a star-shaped pillar with some bright spots similar to the ones in Fig. 5.13, with varying sizes and shapes distributed over the surface of the micro-pillar. Some of these spots are marked by red ellipses. The non-uniform etching is also obvious on the surface of the pillar, shown by differently oriented edges pointed with arrows. The corresponding band-gap energy map (see Fig. 5.15b) characterizes regions with five distinct energy values. The ellipses on the band-gap map refer to the related regions in the STM image. According to the map, the spots on the upper-left corner show a Ga-rich (metallic) region, whereas the brighter and bigger spot on the lower right corner is an oxide layer. The semiconducting regions are distributed randomly. The band gap energies between 1.5 eV and 2.3 eV shown with yellow are attributed to the impurities on the surface of the pillars. The light green regions refer to the InGaN QWs embedded in the sample.

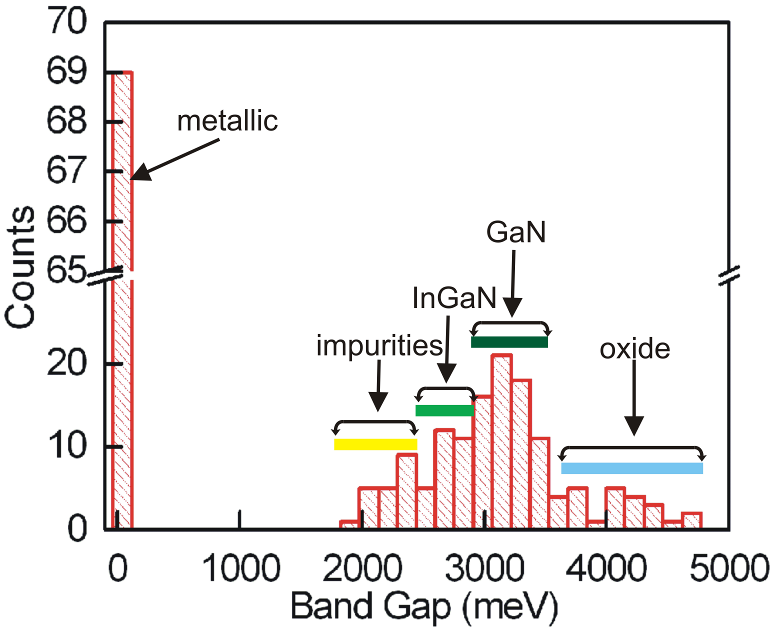

Figure 5.16: Histogram of band gap energies of pillar in Fig. 5.15.

The corresponding histogram in Fig. 5.16 shows five characteristic intervals: the first one at 0 eV, which refers to Ga-rich regions of the pillars; the second one around 2.2 eV, which shows impurities; the third one around 2.8 eV, which refers to InGaN QWs [82]; the fourth one around 3.4 eV, which is the characteristic band gap of GaN; and the last one around 4.2 eV, which shows oxide layers.

5.5.1.4 Discussion

The probable metallization and oxidation process of the GaN surface is already discussed in section 5.5.1.2. Typical impurities–such as Mg–and compounds of molecules–i.e. trimethyl or triethyl precursors–which are used in the growing process of GaN layers are also obvious on the surface of the pillar, as shown by STS data. Unfortunately, these impurities are not resolved by STM images due to the large scale of the STM image.

The traces of InGaN on the surface can be attributed to the 15 nm average roughness of the surface explained in section 5.4.1. This can be explained by the non-uniform character of the etching and underetching effect, which in some regions reached down to the QWs, and thus destroyed the LED structure in these regions. Another reason is that during the etching of the side walls of the pillars, the desorbed InGaN from the side-walls adsorbed on the surface of the pillars.

The etched edges marked with arrows shows once again that the preferential etching take place along the ($\bar{2}110$)-direction.

5.5.1.5 Band Gap Energy Map of Ga, GaN, InGaN, Impurities, and Oxide

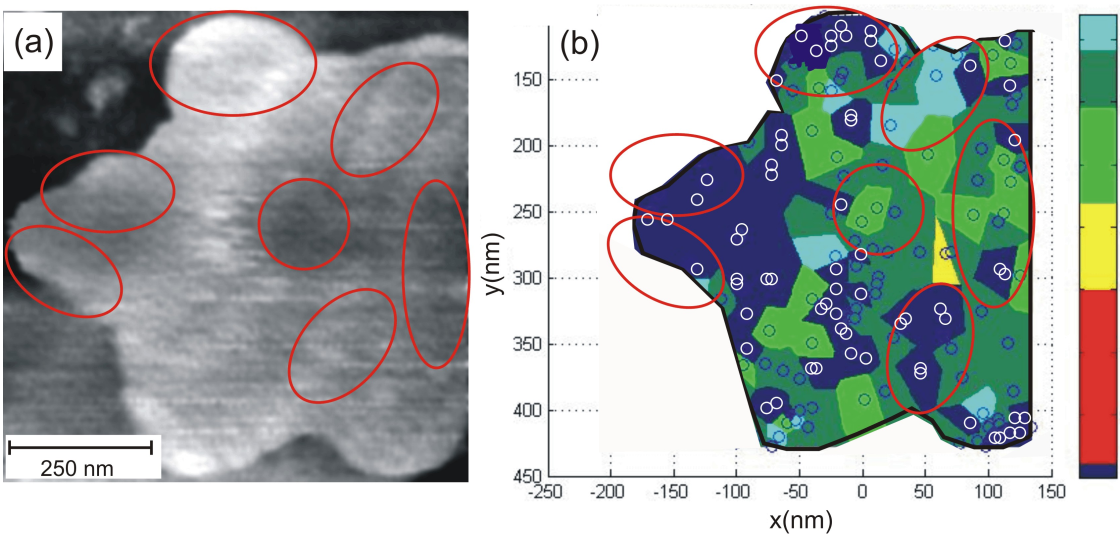

Figure 5.17: Band gap energy map: (a) STM image (usnig beetle-type STM) of a star-shaped pillar, I = 0.153 nA, V = -2.2 V. (b) Band gap map of Ga, GaN, InGaN, impurities, and Oxide created by STS data measured on the star-shaped pillar. The red ellipses correspond to one another at the STM image and at the map.

The STM image in Fig. 5.17a shows part of one star-shaped pillar with several bright spots on the surface. Those spots vary according to their intensities. Besides bright spots, there are also some depletion regions in the center and on the right side of the pillar. The corresponding band-gap energy map (see Fig. 5.17b) defines the bright spot regions with two distinct energy values: Ga-rich (metallic) and oxide. The depletion regions at the center and on the right hand side of the pillar is defined to be GaN and InGaN QWs. According to the STS, there are also impurities defined on the surface of the pillar.

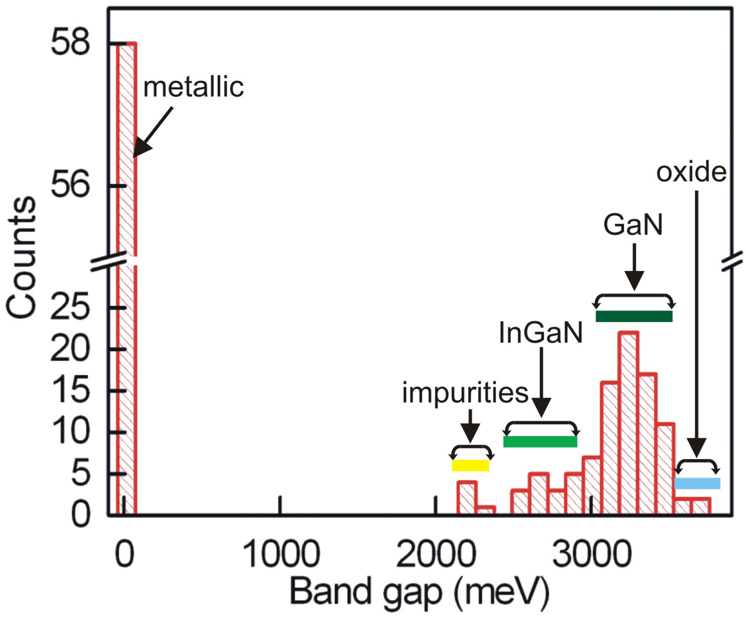

Figure 5.18: Histogram of band gap energies of pillar in Fig. 5.17.

The histogram 5.17c shows five different band gap energies: the first one at 0 eV for Ga-rich regions; the second one, around 2.2 eV, showing the impurities; the third one, around 2.8 eV, attributed to InGaN QW; the fourth one, at 3.4 eV, which is characteristic for the band gap of GaN; and finally at 3.5 eV, showing the oxide layer.

5.5.1.6 Discussion

GaN and Ga-rich regions are also the dominating features here. The InGaN QW regions, positioned at the corner and at the center of the pillars, are seen as depletions in the STM image. The InGaN at the center of the pillar can be explained by either non-uniform etching or absorption of InGaN, which is desorbed from the side walls of the pillars during the etching process.

5.5.1.7 Band Gap Energy Map of Ga and Oxide after Sputtering

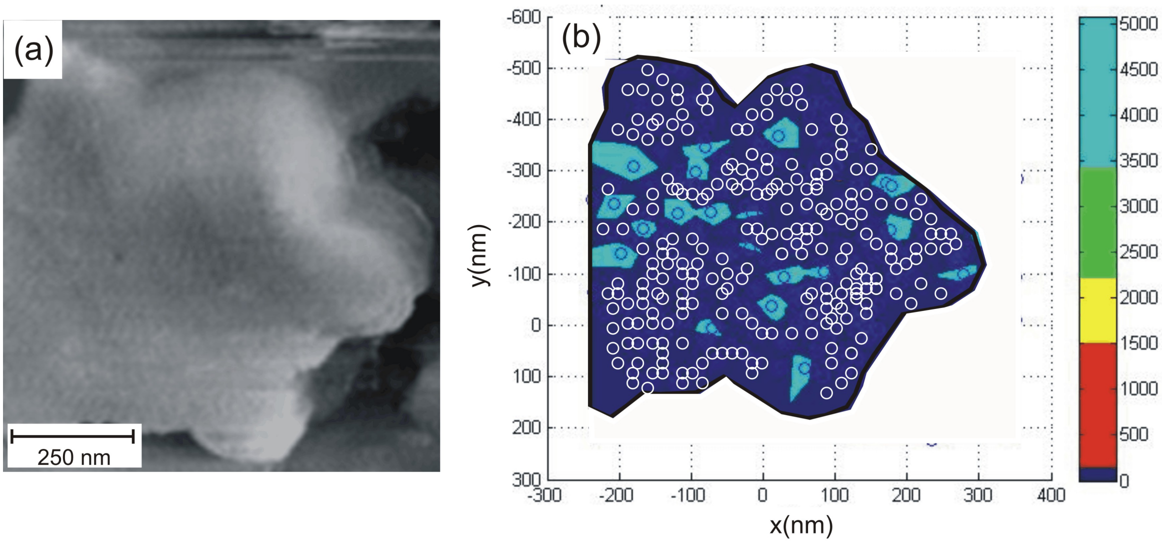

Figure 5.19: Band gap energy map: (a) STM image (usnig beetle-type STM) of a star-shaped pillar, I = 0.153 nA, V = -3.8 V. (b) Band gap map of Ga created by STS data measured on the star-shaped pillar.

In order to remove the remaining oxide layers coming either from the SiO_2 capping layer or from the quick oxidization process of GaN, I sputtered the sample using Ar ion bombardment. The parameters for sputtering were 10 sec at 0.6 keV with an emission current of 6 μA at an Ar pressure of P_{Ar} = $5{\cdot}10^{-5}$. Fig. 5.19a shows part of one star-shaped pillar after this procedure. The varying contrast between the lower and the upper corner of the pillar indicates a roughness induced by inhomogeneous sputtering. The band-gap energy map in Fig. 5.19b illustrates that the pillar is almost metallic.

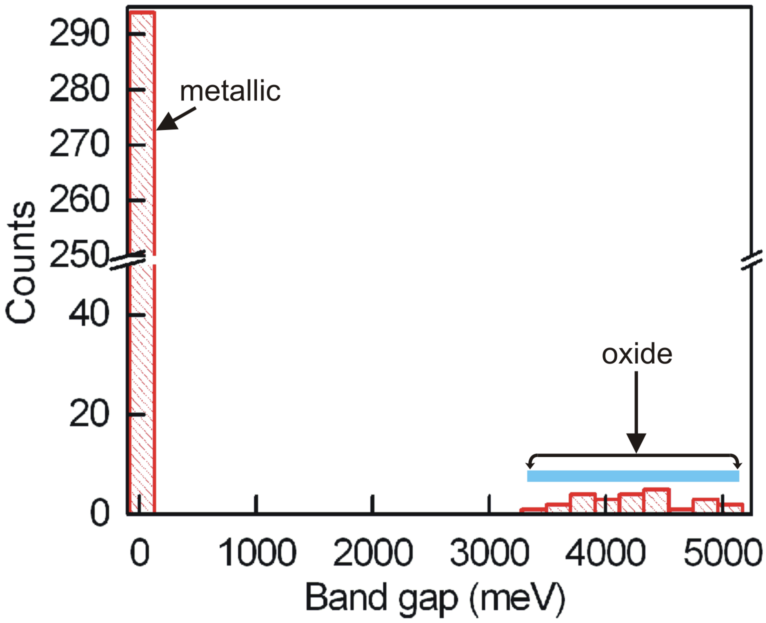

Figure 5.20: Histogram of band gap energies of pillar in Fig. 5.19.

As confirmed in Histogram 5.20, the oxide layer is mostly removed. However, 2% of the surface is still covered by the residual oxide. Another sputtering is expected to remove the remainder.

5.5.1.8 Discussion

As the N atoms have a higher sputtering yield than the Ga atoms, they were easily removed from the surface as Ga atoms. The sputtering removed preferentially the N atoms, leaving a Ga-rich surface.

5.5.2 Overall Discussion

In this chapter, it was shown that the multi-scale STM is a powerful instrument used to study the morphological and the electronic structure of GaN-based micro-pillars' surface locally. By using the STM and the STS, I have identified the etching process that took place during the fabrication of GaN-based microstructures. These techniques can be utilized to improve the fabrication process of pre-structured samples and gain better control of them.

Use of the multi-scale STM in morphology studies has shown that different kinds of pillars show different etching characteristics. The rod-shaped pillars with inhomogeneous etching characteristics have different distributions in horizontal and vertical directions, while the star-shaped pillars are etched homogeneously and have a six-fold symmetry with equal spacing distribution. Both pillars are positively etched.

Despite a single mask used during the etching process, the formation of different kinds of pillars raises new issues. Various shaped pillars results from preferential etching, which arise from underetching. Underetching is an effect that occurs as a result of high etching rates. Due to the high etching rates, the etching process does not stop at the borders defined by the mask pattern but rather continues to etch the pillars towards their centers. This causes a deformation in the geometry of the pillars. The lower etching rates, as seen by rod-shaped pillars, cause an asymmetric etching characteristic, whereas the higher etching rates have a symmetric etching characteristic but result in underetching effects. In the future, it will be important to avoid underetching effects in the manufacture of pillars and ensure a homogeneous distribution of spacing. This will made possible by choosing a suitable etching rate that is low enough to get high-aspect ratio pillars but not too high so as to avoid underetching effects.

The STS analysis achieved by the multi-scale STM is used to identify the doping type and the band-gap width distribution of the individual pillars' surfaces. This study revealed that the capping GaN layer is p-doped, which is important to distinguish it from differently doped neighbouring regions. According to the STS, the surface of the pillars are not semiconducting as expected, but rather show an inhomogeneous characteristic. In addition to the semiconducting regions, the surface contains metallic, insulating, and impurity regions.

The metallization of the sample is caused by Ga atoms, which might have occurred because of the etching rates and the cleaning process of the GaN-based sample by Ga absorption/desorption.

The semiconducting regions on the surface are GaN and InGaN. GaN is the conspicuous terminating layer, whereas InGaN is the QW layers embedded into the sample, which is not clear to find it on the surface. There are two reasons for InGaN's formation on the surface. The first one is the inhomogeneous and uncontrolled etching process. The etching did not stop at the terminating GaN layer but instead continued at some regions down to InGaN layers, forming a rough surface. The second reason is that during the etching of the side walls of the pillars, the desorbed InGaN from the side-walls adsorbed on the surface of the pillars.

The impurities identified are typically Mg and compounds of molecules–i.e. trimethyl or triethyl precursors–used at the growing process of GaN layers. Moreover, the oxide layer on the surfaces of the pillars might be caused by the capping SO_2 layer or the quick oxidation rates of GaN.

Total removal of the oxide layer was not made possible by the thermal annealing procedure. Furthermore, the sputtering process used to remove the residual oxide resulted in the polarization of the surface. The N atoms with higher sputtering yields are removed from the surface, leaving a Ga-rich surface behind.

Chapter 6

Summary and Outlook

This work focuses on the construction of a room temperature, multi-scale STM in a UHV system and the investigations on GaN-based micro-pillars by means of this multi-scale STM.

The experimental setup contains a UHV chamber that provides a clean environment for surface investigations. Furthermore, the system enables one to transfer and reproducibly prepare the samples by using custom-built sample handling tools. The measuring instrument of the setup is the multi-scale STM. The creation of the multi-scale STM resulted from the desire to investigate surfaces pre-structured on the micro- or nanometer scales and enables the study of surfaces not only morphologically but also electronically. The advantage of the multi-scale STM over other measuring instruments with large scanning ranges, such as the SEM, is that it enables the investigation of electronic properties of structures not only on the nanometer scale but also on the millimeter scale. This ability was made possible by combining two different stages: A commercial piezo stage for a scan range from 450 μm x 450 μm to 7 μm x 7 μm and a custom-built, beetle-type STM for scan areas from 5 μm x 5 μm down to nanometer resolutions. As the multi-scale STM is constructed from two scan units, the controller consists of several units and a control software composed of two user interfaces for each scan unit. The tip-surface distance is regulated by two feedback loops, which belong to the beetle-type STM and the XYZ-scanning stage-based STM. Switching between the two scan units for scanning is possible without losing the position of the tip.

On the other hand, the ability of scanning on millimeter scales requires mechanical stability. This is achieved by choosing a proper damping system that filters different frequency ranges and directions.

GaN-based III-V compound semiconductor heterostructures, due their broad optical emission bands in all regions of the visible spectrum, are attracting interest in the field of nano-technologies. However, the controlled fabrication of these micro-pillars is highly challenging. The control and improvement of such structures will only be made possible through better understanding of not only of the morphology but also of their electronic structure. Until now, these micro-pillars have been studied only morphologically by means of the SEM, while the electrical properties of the micro-pillars have been unknown. This lack of information has been resolved through the use of the multi-scale STM.

In this work, the morphological characteristic of the GaN-based micro-pillars on the micrometer and nanometer scales is presented by means of the multi-scale STM. According to the morphology studies, the GaN-based sample contains various types of micro-pillars, and each kind of micro-pillars has individual etching characteristics and individual distributions of spacing. Furthermore, the formation of various types of micro-pillars is shown to be resulted from the underetching effect. Moreover, the investigations revealed that the underetching takes place in the direction of a-planes with lower atom density.

The local scanning tunneling spectroscopy (STS) is used to answer, for the first time, the question of the electronic structures of the surface of the micro-pillars. The STS allows the doping type, the oxidation and metallization levels, the terminating layer, and the band-gap energy width of the individual micro-pillars to be determined. According to the STS, the surfaces of the micro-pillars are not conserved homogeneously, consisting only of GaN as expected, but is distributed inhomogeneously and contains metallic (Ga-rich), semiconducting (GaN, InGaN), impurity, and oxide regions. Some possible reasons for this are explained in detail.

The thermal annealing process was not enough to remove the oxide layer completely. Additionally, sputtering the sample with Ar ions to remove the residual oxide resulted in the polarization of the surface. The N atoms, with higher sputtering yields, are removed from the surface, leaving a Ga-rich surface behind.

In the future, the multi-scale STM may be used for any conducting structures on the micrometer scale. Furthermore, bulky molecules with dimensions of several nm on conducting surfaces can also be investigated. Those molecules can be used as columns of vertically-grown nanowires. For this purpose, not only bulky but also a smaller type of molecules (e.g. benzene molecules) deposited on the surface can be used. With the aid of the STM tip, the benzene molecules can be picked up and placed on top of the bulky molecule. Due to the multi-scale STM's flexibility in the z-direction, it is possible to investigate these nanowires based on molecules by using the tip as one electrode and the surface as the second electrode. In particular, the latter example could not be investigated by a SEM-STM combination due to the SEM's damaging electron beam.

Another example are anodized aluminium oxide (AAO) nano-pores filled by metal atoms. While the STM requires conducting samples for investigations, AAO samples, with their insulating regions, require a special approach system to avoid tip crashes. Therefore, the two scan units of the multi-scale STM can be used at the same time for the coarse approach mechanism. Additionally, the deposition of molecules onto this complex system–i.e. porphyrine molecules–will open up new realms in nanotechnologies. The porphyrine molecules, with their light absorption wavelength in visible spectrum, are very good candidates for molecular solar cells and light emitting diodes (LEDs). Because of this, the study of the molecular and electronic properties of these molecules lying at the metal-insulator interfaces can be used for the development and fabrication of new generation solar cells and LEDs.

Another interesting approach to new generation LEDs is a core-shell strategy. In the core-shell approach, a nano-pillar is formed of an inner core and an outer shell. The inner core and the outer shell are differently doped with respect to one another. This combination builds a solid state light source. With the multi-scale STM's ability to investigate the electronic structures of micro-pillars, it becomes possible to distinguish two differently doped regions and further define the band-gap widths of the individual micro- and nano-pillars.

This is the first STM study reported on pre-structured samples, giving morphological and electrical information on some hundred micrometer scale. I hope that these will open a new vista for studies of predefined micro and nanostructures.

Appendix A: Anodic Aluminium Oxide

Anodic aluminium oxide (AAO) templates and membranes are used to fabricate structures on the nanometer scale [100, 101]. The insulating properties of AAO allow for the deposition of various materials [102, 103], i.e. metal atoms.
The AAO templates are prepared by using a standard two-step anodization procedure. High-purity aluminium foils (99.99%) are used. After annealing the Al foils in air at 400^{o}C for 3h, they are electro-polished in a polishing solution. After the first anodic oxidation process, the alumina layer is removed by a mixed solution of H_3PO_4 and H_2CrO_4. This process is repeated at the second anodic oxidation. The remaining metallic aluminum of the porous alumina template is removed in a $CuCl_2$ solution. Finally, a transparent porous alumina membrane is obtained. The AAO sample is fabricated at the Technical University of Braunschweig by Prof. Lemmens's group.
The anodized aluminium oxide (AAO) nano-pores filled by metal atoms are planned to be used as a template for deposition of molecules, i.e. porphyrine molecules. The study of the molecular and electronic properties of these molecules lying at the metal-insulator interfaces can be used for the development and fabrication of new generation solar cells and LEDs.
While the STM requires conducting samples for investigations, AAO samples, with their insulating regions, require a special approach system to avoid tip crashes. Therefore, the two scan units of the multi-scale STM can be used at the same time for the coarse approach mechanism.

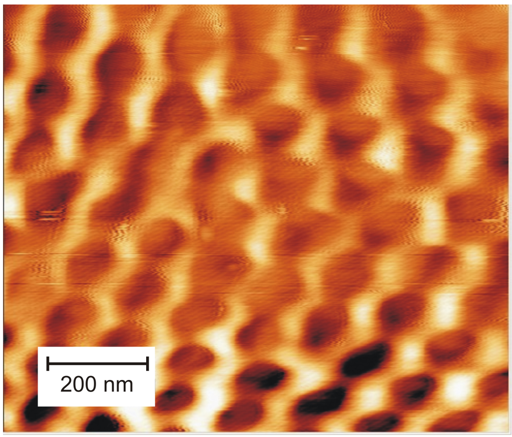

Figure 1: A.1: AFM image of AAO sample.

However, deposition of metal atoms into the AAO nanopores resulted in an extreme rough surface, which was then not possible to be investigated by a STM. The preliminary measurements are done by a AFM. In Fig. 1, an AFM image of an empty AAO template is shown. The pores are approximately 100 nm large and form a hexagonal array.

In the future, sputtering and annealing processes should be applied to the AAO sample to get flatter surfaces that will enable further investigations by the multi-scale STM.

Bibliography

[1] G. Binnig and H. Rohrer. Scanning tunnelling microscopy. *Helv. Phys. Acta*, 55:726, 1982.

[2] G. Binnig, H. Rohrer, C. Gerber, and E. Weibel. 7x7 reconstruction on Si(111) resolved in real space. *Phys. Rev. Lett.*, 50:120, 1983.

[3] G. Binnig and H. Rohrer. Scannig tunelling microscopy. *Surf. Sci.*, 126:236, 1983.

[4] G. Binnig and H. Rohrer. Scanning tunneling microscopy. *Surf. Sci.*, 152-153:17, 1985.

[5] G. Binnig, H. Rohrer, C. Gerber, and E. Weibel. Surface studies by scanning tunneling microscopy. *Phys. Rev. Lett.*, 49:57, 1982.

[6] F. Besenbacher, E. Laegsgaard, and I. Stensgaard. Fast-scanning stm studies. *Materials today*, 8:26, 2005.

[7] R. M. Feenstra and A. P. Fein. Surface morphology of GaAs(110) by scanning tunneling microscopy. *Phys. Rev. B*, 32(2):1394, 1985.

[8] W. Ho. Single-molecule chemistry. *J. Chem. Phys.*, 117:11033, 2002.

[9] J. Henzl and K. Morgenstern. An electron induced two-dimensional switch made of azobenzene derivatives anchored in supramolecular assemblies. *Phys. Chem. Chem. Phys.*, 12:6035, 2010.

[10] G. Binnig, H. Rohrer, C. Gerber, and E. Weibel. Tunneling through a controllable vacuum gap. *Appl. Phys. Lett.*, 40:178, 1982.

[11] K. Besocke. An easily operable scanning tunneling microscope. *Surf. Sci.*, 181:145, 1987.

[12] J. Frohn, J. F. Wolf, K. Besocke, and M. Teske. Coarse tip distance adjustment and positioner for a scanning tunneling microscope. *Rev. Sci. Instrum.*, 60:1200, 1989.

[13] N. Pertaya, K.-F. Braun, and K.-H. Rieder. On the stability of besocke-type scanners. *Rev. Sci. Instrum.*, 75:2608, 2004.

[14] L. Petersen, M. Schunack, B. Schaefer, T. R. Linderoth, P. B. Rasmussen, P. T. Sprunger, E. Laegsgaard, I. Stensgaard, and F. Besenbacher. A fast-scanning, low- and variable-temperature scanning tunneling microscope. *Rev. Sci. Instrum.*, 72:1438, 2001.

[15] Ch. Gerber, G. Binnig, H. Fuchs, O. Marti, and H. Rohrer. Scanning tunneling microscope combined with a scanning electron microscope. *Rev. Sci. Instrum.*, 57:221, 1986.

[16] E. Ejder and H. G. Grimmeiss. Optical investigations of Zn, Hg and Li doped GaN. *Applied Physics A: Materials Science & Processing*, 5(3):275–279, 1974.

[17] H. Amano, M. Kito, K. Hiramatsu, and I. Akasaki. P-type conduction in Mg-doped GaN treated with low-energy electron beam irradiation (LEEBI). *Jpn. J. Appl. Phys.*, 28(12):L2112, 1989.

[18] S. Nakamura, M. Senoh, and T. Mukai. High-power InGaN/GaN double-heterostructure violet light emitting diodes. *Appl. Phys. Lett.*, 62(19):2390, 1993.

[19] S. Nakamura, M. Senoh, and T. Mukai. p-GaN/n-InGaN/n-GaN double-heterostructure blue-light-emitting diodes. *J. Appl. Phys.*, 32(1A/B):L8, 1993.

[20] S. Nakamura, T. Mukai, and M. Senoh. Candela-class high-brightness InGaN/AlGaN double heterostructure blue-light-emitting diodes. *Appl. Phys. Lett.*, 64(13):1687, 1994.

[21] S. Nakamura, M. Senoh, N. Iwasa, S. Nagahama, T. Yamada, and T. Mukai. Superbright green InGaN single-quantum-well-structure light-emitting diodes. *Jpn. J. Appl. Phys.*, 34(10B):L1332, 1995.

[22] S. Nakamura, M. Senoh, N. Iwasa, and S. Nagahama. High-brightness InGaN blue, green and yellow light emitting diodes with quantum well structures. *Jpn. J. Appl. Phys.*, 34(7A):L797, 1995.

[23] S. Nakamura, M. Senoh, S. Nagahama, N. Iwasa, T. Yamada, T. Matsushita, H. Kiyoku, and Y. Sugimoto. InGaN-based multi-quantum-well-structure laser diodes. *Jpn. J. Appl. Phys.*, 35(1B):L74, 1996.

[24] S. Nakamura, M. Senoh, S. Nagahama, N. Iwasa, T. Yamada, T. Matsushita, H. Kiyoku, and Y. Sugimoto. InGaN multi-quantum-well structure laser diodes with cleaved mirror facets. *Jpn. J. Appl. Phys.*, 35(2B):L217, 1996.

[25] A. Waag, X. Wang, S. Fündling, J. Ledig, M. Erenburg, R. Neumann, M. Al Suleiman, S. Merzsch, J. Wei, S. Li, H. H. Wehmann, W. Bergbauer, M. Straßburg, A.Trampert, U. Jahn, and H. Riechert. The nanorod approach: GaN nanoleds for solid state lighting. *Physica Status Solidi c*, 8:2296, 2011.

[26] R. Wiesendanger. *Scanning Probe Microscopy and Spectroscopy*. Cambridge University Press, 1994.

[27] J. Bardeen. Tunneling from a many-particle point of view. *Phys. Rev. Lett.*, 6:57, 1961.

[28] J. Tersoff and D. R. Hamann. Theory and application for the scanning tunneling microscope. *Phys. Rev. Lett.*, 50:1998, 1983.

[29] J. Tersoff and D. R. Hamann. Theory of the scanning tunneling microscope. *Phys. Rev. B*, 31:805, 1985.

[30] J. A. Stroscio, R. M. Feenstra, and A. P. Fein. Electronic structure of the si(111)2x1 surface by scanning tunneling microscopy. *Phys. Rev. Lett.*, 57:2579, 1986.

[31] R. J. Hamers. Atomic-resolution surface spectroscopy with the scanning tunneling microscope. *Annu. Rev. Phys. Chem.*, 40:531, 1989.

[32] R. M. Feenstra. Scanning tunneling spectroscopy. *Surf. Sci.*, 299/300:965, 1994.

[33] M. von Ardenne. Das Elektronen-Rastermikroskop. Praktische Ausführung. *Zeitschrift für technische Physik*, 19:407, 1938.

[34] G. Meyer. A simple low-temperature ultrahigh-vacuum scanning tunneling microscope capable of atomic manipulation. *Rev. Sci. Instrum.*, 67:2960, 1996.

[35] J. Perdereau, J.P. Biberian, and G. E. Rhead. Adsorption and surface alloying of lead monolayers on (111) and (110) faces of gold. *J. Phys. F: Metal Phys.*, 4:798, 1974.

[36] Ü. Sökmen, A. Stranz, S. Fündling, S. Merzsch, R. Neumann, H.-H. Wehmann, E. Peiner, and A. Waag. Shallow and deep dry etching of silicon using icp cryogenic reactive ion etching process. *Mycrosyst. Technol.*, 16:863, 2010.

[37] K. Morgenstern, J. Kibsgaard, J. P. Lauritsen, E. Laegsgaard, and F. Besenbacher. Cobalt growth on two related close-packed noble metal surfaces. *Surf. Sci.*, 601:1967, 2007.

[38] J. V. Barth, H. Brune, and G. Ertl. Scanning tunneling microscopy observations on the reconstructed au(111) surface: Atomic structure, long-range superstructure, rotational domains, and surface defects. *Phys. Rev. B*, 42:9307, 1990.

[39] S. Narasimhan and D. Vanderbilt. Elastic stress domains and the herringbone reconstruction on au(111). *Phys. Rev. Lett.*, 69:1564, 1992.

[40] H. P. Maruska, W. C. Rhines, and D. A. Stevenson. Preparation of mg-doped gan diodes exhibiting violet electroluminescence. *Materials Research Bulletin*, 7(8):777, 1972.

[41] H. Amano, N. Sawaki, I. Akasaki, and Y. Toyoda. Metalorganic vapor phase epitaxial growth of a high quality GaN film using an AlN buffer layer. *Appl. Phys. Lett.*, 48(5):353, 1986.

[42] H. Amano, T. Asahi, and I. Akasaki. Stimulated emmision near ultraviolet at room temperature from a GaN film grow on sapphire by MOVPE using an AlN buffer layer. *Jpn. J. appl. Phys.*, 29:L205, 1990.

[43] S. Nakamura, N. Iwasa, M. Senoh, and T. Mukai. Hole compensation mechanism of p-type GaN films. *Jpn. J. Appl. Phys.*, 31(5A):L1258, 1992.

[44] S. Nakamura, T. Mukai, M. Senoh, and N. Iwasa. Thermal annealing effects on p-type Mg-doped GaN films. *Jpn. J. Appl. Phys.*, 31(2B):L139, 1992.

[45] H. Morkoç, S. Strite, G. B. Gao, M. E. Lin, and B. Sverdlov nad M. Burns. Large band gap SiC, III-V nitride, and II-VI ZnSe-based semi-conductor device technologies. *J. Appl. Phys.*, 76:1363, 1994.

[46] S. Nakamura, M. Senoh, S. Nagahama, N. Iwasa, T. Yamada, T. Matsushita, Y. Sugimoto, and H. Kiyoku. High-power, long-lifetime ingan multi-quantum-well-structure laser diodes. *Jpn. J. Appl. Phys.*, 36(8B):L1059, 1997.

[47] S. Nakamura, M. Senoh, S. Nagahama, N. Iwasa, T. Yamada, T. Matsushita, H. Kiyoku, Y. Sugimoto, T. Kozaki, H. Umemoto, M. Sano, and K. Chocho. InGaN/GaN/AlGaN-based laser diodes with modulation-doped strained-layer superlattices grown on an epitaxially laterally overgrown GaN substrate. *Appl. Phys. Lett.*, 72(2):211, 1998.

[48] S. Nakamura, M. Senoh, S. Nagahama, N. Iwasa, T. Yamada, T. Matsushita, H. Kiyoku, Y. Sugimoto, T. Kozaki, H. Umemoto, M. Sano, and K. Chocho. InGaN/GaN/AlGaN-based laser diodes with modulation-doped strained-layer superlattices. *Jpn. J. Appl. Phys.*, 36:1568, 1997.

[49] M. E. Levinshtein, S. L. Rumyantsev, and M. S. Shur. *Properties of advanced semiconductor materials: GaN, AlN, InN, BN, SiC, SiGe*. John Wiley & Sons, New York, 2001.

[50] S. Bloom. Band structures of GaN and AlN. *J. Phys. Chem. Solids*, 32(9):2027, 1971.

[51] M. Leszczynski, T. Suski, H. Teisseyre, P. Perlin, I. Grzegory, J. Jun, S. Porowski, and T. D. Moustakas. Thermal expansion of gallium nitride. *J. Appl. Phys.*, 76(8):4909, 1994.

[52] E. Ejder. Refractive index of GaN. *Physica Status Solidi (a)*, 6(2):445, 1971.

[53] E. K. Sichel and J. I. Pankove. Thermal conductivity of GaN: 25-360K. *J. Phys. Chem. Sol.*, 38(3):330, 1977.

[54] F. A. Ponce and D. P. Bour. Nitride-based semiconductors for blue and green light-emitting devices. *Nature*, 386:351, 1997.

[55] S. Nakamura, S. Pearton, and G. Fasol. *The Blue Laser Diode - The Complete Story*. Springer, Berlin, 2. auflage edition, 2000.

[56] M. Bockowski. Review: Bulk growth of gallium nitride: challenges and difficulties. *Crystal Research and Technology*, 42(12):1162, 2007.

[57] W. Utsumi, H. Saitoh, H. Kaneko, T. Watanuki, K. Aoki, and O. Shimomura. Congruent melting of gallium nitride at 6 gpa and its application to single-crystal growth. *Nature Mater.*, 2(3):735, 2003.

[58] T. Detchprohm, K. Hiramatsu, H. Amano, and I. Akasaki. Hydride vapor phase epitaxial growth of a high quality GaN film using a ZnO buffer layer. *Appl. Phys. Lett.*, 61(22):2688, 1992.

[59] A. Sakai, H. Sunakawa, and A. Usui. Defect structure in selectively grown GaN films with low threading dislocation density. *Appl. Phy. Lett.*, 71(16):2259, 1997.

[60] A. Usui, H. Sunakawa, A. Sakai, and A. A. Yamaguchi. Thick GaN epitaxial growth with low dislocation density by hydride vapor phase epitaxy. *Jpn. J. Appl. Phys.*, 36(7B):L899, 1997.

[61] H. M. Kim, D. S. Kim, Y. S. Park, D. Y. Kim, T. W. Kang, and K. S. Chung. Growth of GaN nanorods by a hybride vapour phase epitaxy method. *Adv. Mater.*, 14:13, 2002.

[62] E. Calleja, M. A. Sánchez-García, F. J. Sánchez, F. Calle, F. B. Naranjo, E. Muñoz, U. Jahn, and K. Ploog. Luminescence properties and defects in GaN nanocolumns grown by molecular beam epitaxy. *Phys. Rev. B*, 62:24, 2000.

[63] J. Ristić, M.A. Sánchez-García, J.M. Ulloa, E. Calleja, J. Sanchez-Páramo, J.M. Calleja, U. Jahn, A. Trampert, and K.H. Ploog. AlGaN nanocolumns and AlGaN/GaN/AlGaN nanostructures grown by molecular beam epitaxy. *Phys. Status Solidi b*, 234:717, 2002.

[64] A. Kikuchi, K. Yamano, M. Tada, and K. Kishino. Stimulated emission from GaN nanocolumns. *Phys. Status Solidi b*, 241:2754, 2004.

[65] V. N. Jmerik, V. V. Mamutin, V. A. Vekshin, T. V. Shubina, S. V. Ivanov, and P. S. Kop'ev. Coaxial rf-magnetron nitrogen activator for GaN MBE growth. *Materials Science and Engineering B*, 59(1-3):60, 1999.

[66] O. Ambacher. Growth and application of group III-nitrides. *J. Phys. D: Appl. Phys.*, 31(20):2653, 1998.

[67] O. Briot, J. P. Alexis, M. Tchounkeu, and R. L. Aulombard. Optimization of the MOVPE growth of GaN on sapphire. *Mater. Sci. Eng. B*, 43(1-3):147, 1997.

[68] F. Qian, Y. Li, S. Gradecak, D. Wang, C. J. Barrelet, and C. M. Lieber. Gallium nitride-based nanowire radial heterostructures for nanophotonics. *Nano Lett.*, 4:1975, 2004.

[69] S. Nakamura, T. Mukai, and M. Senoh. Si- and Ge-Doped GaN films grown with GaN buffer layers. *Jpn. J. Appl. Phys.*, 31:2883, 1992.

[70] S. D. Lester, F. A. Ponce, M. G. Craford, and D. A. Steigerwald. High dislocation densities in high efficiency GaN-based light-emitting diodes. *Appl. Phys. Lett.*, 66(10):1249, 1995.

[71] S. J. Rosner, E. C. Carr, M. J. Ludowise, G. Girolami, and H. I. Erikson. Correlation of cathodoluminescence inhomogeneity with microstructural defects in epitaxial GaN grown by metalorganic chemical-vapor deposition. *Appl. Phy. Lett.*, 70(4):420, 1997.

[72] M. Godlewski, E. Łusakowska, E. M. Goldys, M. R. Phillips, T. Böttcher, S. Figge, D. Hommel, P. Prystawko, M. Leszczynski, I. Grzegory, and S. Porowski. Diffusion length of carriers and excitons in GaN-influence of epilayer microstructure. *Appl. Surf. Sci.*, 223(4):294, 2004.

[73] W. A. Brantley, O. G. Lorimor, P. D. Dapkus, S. E. Haszko, and R. H. Saul. Effect of dislocations on green electroluminescence efficiency in gap grown by liquid phase epitaxy. *J. Appl. Phys.*, 46(6):2629, 1975.

[74] I. Ladany. Gallium phosphide double-epitaxial diodes. *J. Electrochemical Society*, 116(7):993, 1969.

[75] W. H. Hackett, Jr., R. H. Saul, R. W. Dixon, and G. W. Kammlott. Scanning electron microscope characterization of GaP red-emitting diodes. *J. Appl. Phys.*, 43(6):2857, 1972.

[76] O. G. Lorimor, P. D. Dapkus, and W. H. Hackett, Jr. Very high efficiency GaP green light emitting diodes. *J. Electrochemical Society*, 122(3):407, 1975.

[77] T. Suzuki and Y. Matsumoto. Effects of dislocations on photoluminescent properties in liquid phase epitaxial GaP. *Appl. Phys. Lett.*, 26(8):431, 1975.

[78] M. Ettenberg. Effects of dislocation density on the properties of liquid phase epitaxial GaAs. *J. Appl. Phys.*, 45(2):901, 1974.

[79] M. Ettenberg, H. Kressel, and S. L. Gilbert. Minority carrier diffusion length and recombination lifetime in GaAs:Ge prepared by liquid-phase epitaxy. *J. Appl. Phys.*, 44(2):827, 1973.

[80] A. H. Herzog, D. L. Keune, and M. G. Craford. High-efficiency Zn-diffused GaAs electroluminescent diodes. *J. Appl. Phys.*, 43(2):600, 1972.

[81] R. J. Roedel, A. R. von Neida, R. Caruso, and L. R. Dawson. The effect of dislocations in $Ga_{1-x}Al_xAs : Si$ light-emitting diodes. *J. Electrochemical Society*, 126(4):637, 1979.

[82] S. Fündling, Ü. Sökmen, E. Peiner, T. Weimann, P. Hinze, U. Jahn, A. Trampert, H. Riechert, A. Bakin, H-H. Wehmann, and A. Waag. Gallium nitride heterostructures on 3D structured silicon. *Nanotechnology*, 19:405301, 2008.

[83] N. J. Watkins, G. W. Wicks, and Y. Gao. Oxidation study of GaN using x-ray photoemission spectroscopy. *Appl. Phy. Lett.*, 75(17):2602, 1999.

[84] T. K. Zywietz, J. Neugebauer, and M. Scheffler. The adsorption of oxygen at GaN surfaces. *Appl. Phys. Lett.*, 74:1695, 1999.

[85] M. Dialea, , F.D. Aureta, N.G. van der Berga, R.Q. Odendaala, and W.D. Roosb. Analysis of GaN cleaning procedures. *Appl. Surf. Sci.*, 246:279, 2005.

[86] S. W. King, J. P. Barnak, M. D. Bremser, K. M. Tracy, C. Ronning, R. F. Davis, and R. J. Nemanich. Cleaning of AlN and GaN surfaces. *j. Appl. Phys.*, 84:5248, 1998.

[87] R. W. Hunt, L. Vanzetti, T. Castro, K. M. Chen, L. Sorba, P. I. Cohen, W. Gladfelter, J. M. Vanhove, J. N. Kuznia, M. A. Khan, and A. Franciosi. Electronic structure, surface composition and long-range order in GaN. *Physica B: Condensed Matter*, 185:415, 1993.

[88] V. M. Bermudez, D. D. Koleske, and A. E. Wickenden. The dependence of the structure and electronic properties of wurtzite GaN surfaces on the method of preparation. *Appl. Surf. Sci.*, 126:69, 1998.

[89] A. J. MacGinnis, D. Thomson, R. F. Davis, E. Chen, A. Michel, and H. H. Lamb. In situ cleaning of GaN/6H-SiC substrates in NH_3. *J. Christ. Growth*, 222:452, 2001.

[90] C. Schulz, T. Schmidt, J. I. Flege, N. Berner, C. Tessarek, D. Hommel, and J. Falta. Oxide removal from GaN(0001) surfaces. *Phys. Status Solidi C6*, 6:305, 2009.

[91] S. Ingrey. III–V surface processing. *J. Vac. Sci. Technol.*, A10:829, 1992.

[92] G. Craciun, M. A. Blauw, E. van der Drift, P. M. Sarro, and P. J. French. Temperature influence on etching deep holes with sf_6/o_2 cryogenic plasma. *J. Micromechanics and Microengineering*, 12:390, 2002.

[93] L. Stafford, W. T. Lim, S. J. Peatron, Ju-Il Song, J-S. Park, Y-W. Heo, J-H. Lee, J-J. Kim, M. Chicoine, and F. Schiettekatte. Deep etch-induced damage during ion-assisted chemical etching of sputtered indium-zinc-oxide films in $Ar/CH_4/H_2$ plasmas. *Thin solid films*, 516:2869, 2008.

[94] H. M. Lee, D. C. Kim, W. Jo, and K. Y. Kim. Inductively coupled plasma etching of $(Ba,Sr)TiO_3$ thin films. *J. vac. Sci. Technol.*, B 16:1891, 1998.

[95] T. Shibano, T. Takenaga, K. Nakamura, and T. Oomori. Etching of $(Ba,Sr)TiO_3$ film by chlorine plasma. *J. Vac. Sci. Technol.*, A 18:2080, 2000.

[96] J. A. Diniz, J. W. Swart, K. B. Jung, J. Hong, and S. J. Pearton. Inductively coupled plasma etchingof in-based compound semiconductors in $CH_4/H_2/Ar$. *Solid State Electron*, 42:1947, 1998.

[97] A. R. Smith, R. M. Feenstra, D. W. Greve, J. Neugebauer, and J. E. Northrup. Reconstructions of the GaN(000-1) surface. *Phys. Rev. Lett.*, 79(20):3934, 1997.

[98] A. R. Smith, R. M. Feenstra, D. W. Greve, M.-S. Shin, M. Skowronski, J. Neugebauer, and J. E. Northrup. Reconstructions of GaN(0001) and (000-1) surfaces: Ga-rich metallic structures. *J. Vac. Sci. and Technol. B*, 16(4):2242, 1998.

[99] R. Klauser, P. S. A. Kumar, and T. J. Chuang. A synchrotron radiation photoemission study of gallium and nitrogen adsorption on 6H-SiC, $LiGaO_2$ and gan substrates: initial stages of gan formation. *Surf. Sci.*, 411:329, 1998.

[100] C. R. Martin. Nanomaterials: A membrane-based synthetic approach. *Science*, 266:1961, 1994.

[101] H. Masuda and K. Fukuda. Ordered metal nanohole arrays made by a two-step replication of honeycomb structures of anodic alumina. *Science*, 268:1466, 1995.

[102] L.-P. Carignan, C. Lacroix, A. Ouimet, M. Ciureanu, A. Yelon, and D. Ménard. Magnetic anisotropy in arrays of Ni, CoFeB, and Ni/Cu nanowires. *J. Appl. Phys.*, 102:023905, 2007.

[103] L. Liu, W. Lee, Z. Huang, R. Scholz, and U. Gösele. Fabrication and characterization of a flow-through nanoporous gold nanowire/AAO composite membrane. *Nanotechnology*, 19:335604, 2008.

Curriculum Vitae

Fatih Kalkan

Born on June 17th 1975 in Istanbul

Chronology

April 2005-March 2011	Ph.D. student at the Leibniz Universität Hannover, in the group of Prof. K. Morgenstern
October 2001-February 2005	Master′s (Diplom) student at the Leibniz Universität Hannover. Diploma thesis: The Bianchi Identities of 3D-Dimensional Supergravity. In the group of Prof. N. Dragon
October 1993-July 1999	Bachelor of Science in Physics at the Bogazici University, Istanbul
September 1986-September 1993	A-Levels at Yildiz College, Istanbul

Publications

Articles

- F. Kalkan, M. Mehlhorn, and K. Morgenstern, Molecular Switches at surfaces, submitted for publication to J. Phys. : Condensed Matter
- F. Kalkan, C. Zaum, and K. Morgenstern, A scanning tunneling microscope with a scanning range from 450 μm x 450 μm down to nanometer resolution, in preparation

Talks

- F. Kalkan and K. Morgenstern, Scanning probe microscopy of porphyrines at metal-insulator interfaces, Workshop of the NTH school for contacts in Nanosystems, Wernigerode, Germany (2010), Talk
- F. Kalkan and K. Morgenstern, Multi-scale STM and other activities within the NTH Project: Contacts in Nanosystems, TU Braunschweig, Braunschweig, Germany (2010), Talk

Posters

- F. Kalkan, D. Krüger, M. Al-Suleiman, J. Wei, A. Waag, and K. Morgenstern, Spatially-resolved STS studies on deep dry etched

GaN nano-pillars, Workshop of the NTH school for contacts in Nanosystems, Hannover, Germany (2011), Poster

- F. Kalkan, C. Zaum and K. Morgenstern, A STM with a scan width from 500 μm down to sub nanometers, Workshop of the NTH school for contacts in Nanosystems, Wernigerode, Germany (2010), Poster
- F. Kalkan, C. Zaum and K. Morgenstern, A STM with a scan width from 500 μm down to sub nanometers, Spring meeting of the Deutschen Physikalischen Gesellschaft, Dresden (2009), Poster.

Acknowledgements

First of all, I would like to thank Professor Karina Morgenstern for giving me the chance to work in her group. I would especially like to thank her for never losing her faith in me and for supporting me even when I was having the most difficulty. Her knowledge and experience in the field of STM was instrumental to the success of this project.

I would also like to thank Professor Peter Lemmens for being the second referee and ardent supporter. I am thankful to him and his research group for providing AAO samples as well as to Professor Andreas Waag and his research group for providing the GaN-based sample. This GaN-based sample opened an interesting research field and helped me to demonstrate the large scanning areas of the multi-scale STM.

I would especially like to thank Dr. David Krüger for his participation in this work. His experience with GaN and our discussions about it were invaluable in allowing me to write this thesis. I am also thankful to him for the excellent analysis software that he created.

I would like to thank to my lab and office colleague, Carsten Sprodowski, for his friendship and unrelenting willingness to help me in my times of need. I thank also especially to Christopher Zaum for creating the software and the electronics of the multi-scale STM. Naturally, I would also like to thank the other members of our research group: Friederike Matthaei, Björn Siebrants, and Sarah Heidorn. They have been wonderful friends and collaborators throughout.

Thank you to Dr. Michael Mehlhorn, ex-member of our research group, for his friendship and for his sharing his STM experience with me. I would also like to thank another ex-member, Dr. Jörg Henzl, for his friendship and for his willingness to help whenever I

needed it.
I would like to thank to those in our mechanical and electronic workshops, especially Andreas Wittig, Jens Wiegmann, and Gerhard Neuhaus for their tremendous work. Without them, the construction of the multi-scale STM would not have been possible.
Thank you to Professor Pfnür's group for providing an excellent working environment at the institute. In particular, I would like to thank Thomas Langer for writing a matlab program that saved me a lot of time and Lisa Kühnemund for measuring the SEM images.
Thank you to Heike Kahrs and Elke Trolp for helping me to navigate the bureaucracy and cut through the red tape. Without them, it wouldn't have been easy for me to obtain a visa.
Thank you to Dr. Helmut Rodemann, Dr. Gundog Yucesan, Dr. Cemil Kayis, Kristina Coskun, and Mehmetali Ilhan for their valuable corrections.
I would like to thank my mom, my mother-in-law, and my sister for their support.
I would most especially like to thank my wife, Susanne, for supporting me mentally, no matter what, and my daughter, Kalila, for bringing me laughter even at the most stressful times.

List of Figures